DGK Ausschuss Geodäsie (DGK)
der Bayerischen Akademie der Wissenschaften

Reihe C | Dissertationen | Heft Nr. 958

Zelong Guo

Co- and Post-seismic Slip Models Inferred from InSAR Geodesy

München 2025

Verlag der Bayerischen Akademie der Wissenschaften, München

ISSN 0065-5325
ISBN 978-3-7696-5370-0

DGK Ausschuss Geodäsie (DGK)
der Bayerischen Akademie der Wissenschaften

Reihe C Dissertationen Heft Nr. 958

Co- and Post-seismic Slip Models
Inferred from InSAR Geodesy

Von der Fakultät für Bauingenieurwesen und Geodäsie
der Gottfried Wilhelm Leibniz Universität Hannover
zur Erlangung des akademischen Grades
Doktor-Ingenieur (Dr.-Ing.)
genehmigte
Dissertation

von

Zelong Guo, M.Sc.

München 2025

Verlag der Bayerischen Akademie der Wissenschaften, München

ISSN 0065-5325 ISBN 978-3-7696-5370-0

Adresse des Ausschusses Geodäsie (DGK)
der Bayerischen Akademie der Wissenschaften:

Ausschuss Geodäsie (DGK) der Bayerischen Akademie der Wissenschaften

Alfons-Goppel-Straße 11 ● D – 80 539 München

Telefon +49 – 89 – 23 031 1113 ● Telefax +49 – 89 – 23 031 - 1283 / - 1100
e-mail post@dgk.badw.de ● http://www.dgk.badw.de

Prüfungskommission:

Vorsitzender:	Prof. Dr.-Ing. habil. Christian Heipke
Referent:	Prof. Dr. Mahdi Motagh
Korreferenten:	Prof. Dr.-Ing. Steffen Schön
	Prof. Dr. Klaus Reicherter (RWTH Aachen University)

Tag der mündlichen Prüfung: 17.04.2025

Diese Dissertation ist auf dem Server des Ausschusses Geodäsie (DGK)
der Bayerischen Akademie der Wissenschaften, München unter <http://dgk.badw.de/>
sowie unter Wissenschaftliche Arbeiten der Fachrichtung Geodäsie und Geoinformatik
der Leibniz Universität Hannover (ISSN 0174-1454), Nr. 408,
unter <https://doi.org/10.15488/19073>, Hannover 2025 elektronisch publiziert

ISSN 0065-5325 ISBN 978-3-7696-5370-0

Abstract

Earthquake cycle deformation includes interseismic, coseismic, and postseismic deformation. The strain accumulated during the interseismic phase is rapidly released in the form of fault rupture during an earthquake, generating positive stress loading on adjacent regions. This is gradually adjusted through various postseismic mechanisms, leading to ongoing deformation after the earthquake. There is a close relationship between coseismic and postseismic deformation, and studying this relationship can deepen our understanding of seismic dynamics. By modeling coseismic deformation, we can obtain the fault's geometry and establish a slip distribution model, which is critical for subsequent seismic hazard assessment. Additionally, based on the coseismic slip distribution, we can determine changes in the stress state of the fault and surrounding areas. The fault and surrounding media continue to slip postseismically, driven by coseismic stress changes, contributing to postseismic deformation. While postseismic deformation mechanisms are complex, the advancement of space geodetic techniques allows for increasingly accurate data collection, offering new insights into the mechanical properties of fault zones and the regional lithospheric rheology.

As the largest earthquake on record in the Zagros Fold-and-Thrust Belt (ZFTB), the 2017 Mw 7.3 Sarpol-e Zahab earthquake in Iran-Iraq border highlighted the region's potential for magnitude 7+ earthquakes. A detailed study of the faulting process during this event is essential for understanding the seismogenic structures and evaluating seismic hazards in the region. Additionally, in this seismogenic region (Northern Zagros), the Phanerozoic sedimentary cover rock reaches a thickness of about 8–13 km, overlying the Phanerozoic crystalline basement. A Hormuz salt layer is suspected to act as a decoupling layer at the cover-basement interface due to the strong mechanical contrast between the sedimentary cover and basement (e.g., Alavi, 2007; McQuarrie, 2004). However, the interaction between the faulting process and the sedimentary cover and basement remains unclear. In this thesis, using Interferometric Synthetic Aperture Radar (InSAR) deformation data, we investigate and model both the coseismic and postseismic deformation of this event. The study begins with an introduction to the basic InSAR data processing and the modeling theories for coseismic and postseismic deformation. Then, we apply both analytical and Finite Element Method (FEM) models to examine the coseismic and postseismic deformation of the 2017 Mw 7.3 Sarpol-e Zahab earthquake. The major findings and contributions of this dissertation are summarized as follows:

- The coseismic slip model reveals a planar fault dipping at 15°, which explains the observed coseismic deformation well. The rupture propagated unilaterally southward, involving the sequential rupture of two asperities along a dextral-thrust fault. The main slip area is concentrated at depths of approximately 13–19 km, with a maximum slip exceeding 7 m. The geodetic moment is estimated to be 1.0×10^{20} N m, corresponding to a moment magnitude of Mw 7.3.
- Based on 3-year postseismic InSAR observations, we invert the data for both kinematic and stress-driven (rate-strengthening) afterslip models based on ramp-flat

fault. The kinematic model effectively captures the spatiotemporal variations of the postseismic deformation. A multi-segment, stress-driven afterslip model with depth-varying friction provides a better explanation for the postseismic deformation's evolution compared to a two-segment model. The transition depth inferred from the kinematic and rate-strengthening afterslip models is approximately 12 km, likely corresponding to the cover-basement interface. The best-fitting viscosity from the combined viscoelastic relaxation and stress-driven afterslip models exceeds 10^{19} Pa s, indicating that viscoelastic relaxation contributes negligibly to the postseismic deformation. Both kinematic and stress-driven afterslip models suggest minor afterslip ($\sim$0.3 m) downdip of the coseismic rupture, though resolving this depends heavily on data accuracy and model resolution.

- Because the stress-driven afterslip models with depth-varying friction on the ramp-flat fault cannot explain the postseismic deformation to the west, we integrate 4.5-year postseismic InSAR observations with 2-dimensional (2D) FEM frictional afterslip models using planar faults, ramp-flat faults, and combined ramp-flat and splay faults to determine if fault complexity improves the model fit. Our findings suggest that a planar fault model cannot fully explain the long-wavelength postseismic deformation field. In contrast, the ramp-flat fault model fits better, with a maximum afterslip of approximately 1.0 m up dip of the coseismic rupture. Fault friction variations are estimated at $\sim$0.001 for the up-dip and $\sim$0.0002 for the down-dip sections of the ramp-flat fault. The combined ramp-flat and splay fault model further improves the fit, although the afterslip on the splay fault is minor ($\sim$0.2 m) compared to the ramp-flat fault ($\sim$0.9 m). The friction variation for both faults in the optimal model is approximately 0.0008. This combined model, suggesting a complex interaction between the sedimentary cover and crystalline basement, aligns well with geologic studies and fault slip on the Main Frontal Fault (MFF) in the Zagros.

Keywords: InSAR Observations, Co- and Post-seismic Deformation Modeling, 2017 Mw 7.3 Sarpol-e Zahab Earthquake

Zusammenfassung

Die Verformung im Erdbebenzyklus umfasst interseismische, co-seismische und postseismische Verformungen. Die während der interseismischen Phase akkumulierten Spannungen werden während eines Erdbebens in Form eines schnellen Bruchs an der Störungszone freigesetzt, wodurch in angrenzenden Regionen eine positive Spannungsaufladung erzeugt wird. Diese wird durch verschiedene postseismische Mechanismen allmählich angepasst, was zu einer anhaltenden Verformung nach dem Erdbeben führt. Es besteht eine enge Beziehung zwischen co-seismischer und postseismischer Verformung, und die Untersuchung dieser Beziehung kann unser Verständnis der seismischen Dynamik vertiefen. Durch die Modellierung der co-seismischen Verformung können wir die Geometrie der Störungszone bestimmen und ein Verschiebungsverteilungsmodell erstellen, das für die anschließende Bewertung der seismischen Gefährdung von entscheidender Bedeutung ist. Darüber hinaus können wir auf Grundlage der co-seismischen Verschiebungsverteilung Veränderungen im Spannungszustand der Störungszone und der Umgebung bestimmen. Die Störungszone und das umgebende Gestein gleiten weiterhin postseismisch, angetrieben durch die co-seismischen Spannungsänderungen, was zur postseismischen Verformung beiträgt. Obwohl die Mechanismen der postseismischen Verformung komplex sind, ermöglicht der Fortschritt der weltraumgestützten geodätischen Messtechniken eine immer genauere Datenerfassung und bietet neue Einblicke in die mechanischen Eigenschaften von Störungszonen und die regionale Rheologie der Lithosphäre.

Als das größte jemals aufgezeichnete Erdbeben im Zagros-Falten- und Überschiebungsgürtel (ZFTB) verdeutlichte das Mw 7,3 Sarpol-e Zahab-Erdbeben im Jahr 2017 an der iranisch-irakischen Grenze das Potenzial der Region für Erdbeben der Magnitude 7 und höher. Eine detaillierte Untersuchung des Störungsprozesses dieses Ereignisses ist unerlässlich, um die seismogenen Strukturen besser zu verstehen und die seismischen Gefahren in der Region zu bewerten. Zudem erreicht in dieser seismogenen Region (nördliches Zagros) die Phanerozoische Sedimentbedeckung eine Mächtigkeit von etwa 8–13 km und überlagert das phanerozoische kristalline Basement. Aufgrund des starken mechanischen Kontrasts zwischen Sedimentbedeckung und Basement wird vermutet, dass eine Hormuz-Salzschicht als Entkoppelungsschicht an der Schnittstelle zwischen Sedimentbedeckung und Basement fungiert (e.g., Alavi, 2007; McQuarrie, 2004). Wie jedoch der Störungsprozess mit der Sedimentbedeckung und dem Basement interagiert, ist weiterhin unklar. In dieser Arbeit untersuchen und modellieren wir sowohl die co-seismische als auch die postseismische Verformung dieses Ereignisses mithilfe von Interferometric Synthetic Aperture Radar (InSAR)-Verformungsdaten. Die Studie beginnt mit einer Einführung in die grundlegenden InSAR-Datenverarbeitungs- und Modellierungstheorien für co-seismische und postseismische Verformungen. Dann wenden wir sowohl analytische Modelle als auch Modelle der Finite-Elemente-Methode (FEM) an, um die co-seismische und post-seismische Deformation des Mw 7,3 Sarpol-e Zahab Erdbebens von 2017 zu untersuchen. Die Hauptbefunde und Beiträge dieser Dissertation werden wie folgt zusammengefasst:

- Das co-seismische Verschiebungsmodell zeigt eine planare Störung mit einem Einfallen von 15°, das die beobachtete co-seismische Verformung gut erklärt. Der Bruch propagierte einseitig nach Süden und umfasste den sequentiellen Bruch von zwei Asperitäten entlang einer dextral-Überschiebungsstörung. Der Hauptverlagerungsbereich konzentriert sich auf Tiefen von etwa 13–19 km, wobei die maximale Verschiebung mehr als 7 m beträgt. Das geodätische Moment wird auf $1,0 \times 10^{20}$ N m geschätzt, was einer Momentenmagnitude von Mw 7,3 entspricht.

- Basierend auf 3-jährigen postseismischen InSAR-Beobachtungen invertieren wir die Daten für sowohl kinematische als auch spannungsgetriebene (rate-strengthening) Nachgleitungsmodelle basierend auf einer Rampen-Flach-Störung. Das kinematische Modell erfasst effektiv die raumzeitlichen Variationen der postseismischen Verformung. Ein mehrsegmentiges, spannungsgetriebenes Nachgleitungsmodell mit tiefenabhängiger Reibung bietet eine bessere Erklärung für die Entwicklung der postseismischen Verformung im Vergleich zu einem zweisegmentigen Modell. Die Übergangstiefe, die aus den kinematischen und rate-strengthening Nachgleitungsmodellen abgeleitet wird, liegt bei etwa 12 km und entspricht wahrscheinlich der Schnittstelle zwischen Sedimentbedeckung und Basement. Die am besten passende Viskosität aus den kombinierten Modellen für viskoelastische Entspannung und spannungsgetriebene Nachgleitungsmodelle beträgt mehr als 10^{19} Pa s, was darauf hinweist, dass die viskoelastische Entspannung nur einen vernachlässigbaren Beitrag zur postseismischen Verformung leistet. Sowohl das kinematische als auch das spannungsgetriebene Nachgleitungsmodell deuten auf ein geringes Nachgleiten ($\sim$0,3 m) unterhalb des co-seismischen Bruchs hin, obwohl die Auflösung stark von der Genauigkeit der Daten und der Modellauflösung abhängt.

- Da die spannungsgetriebenen Nachgleitungsmodelle mit tiefenabhängiger Reibung an der Rampen-Flach-Störung die postseismische Verformung im Westen nicht erklären können, integrieren wir 4,5-jährige postseismische InSAR-Beobachtungen mit 2D-FEM-Modellen für Reibungsnachgleitungsmodelle unter Verwendung planarer Störungen, Rampen-Flach-Störungen und kombinierter Rampen-Flach- und Splay-Störungen, um zu bestimmen, ob die Komplexität der Störung das Modell verbessern kann. Unsere Ergebnisse zeigen, dass ein planares Störungsmodell das langwellige postseismische Verformungsfeld nicht vollständig erklären kann. Im Gegensatz dazu passt das Rampen-Flach-Störungsmodell besser zu den Daten, mit einem maximalen Nachgleiten von etwa 1,0 m oberhalb des co-seismischen Bruchs. Die Reibungsvariationen an der Störung werden auf $\sim$0,001 für den oberen und $\sim$0,0002 für den unteren Bereich der Rampen-Flach-Störung geschätzt. Das kombinierte Rampen-Flach- und Splay-Störungsmodell verbessert die Anpassung weiter, obwohl das Nachgleiten an der Splay-Störung ($\sim$0,2 m) im Vergleich zur Rampen-Flach-Störung ($\sim$0,9 m) gering ist. Die Reibungsvariation für beide Störungen im optimalen Modell beträgt etwa 0,0008. Dieses kombinierte Modell, das auf eine komplexe Interaktion zwischen der Sedimentbedeckung und dem kristallinen Basement hinweist, stimmt gut mit geologischen Studien und dem Störungsschlupf an der Main Frontal Fault (MFF) im Zagros überein.

Schlüsselwörter: InSAR-Beobachtungen, Modellierung co- und postseismischer Deformationen, Erdbeben von Sarpol-e Zahab 2017 (Mw 7,3)

Acknowledgements

As I pen down this chapter, I am filled with a deep sense of gratitude. In October 2020, with a mix of excitement and anxiety, I embarked on my doctoral journey in Germany. Now, four years have swiftly passed, marking an unforgettable chapter in my life. There are so many people to thank.

First and foremost, I would like to express my deepest gratitude to my supervisor, Professor Mahdi Motagh. In the realm of research, you have been a remarkable mentor, offering invaluable guidance and providing many opportunities for international collaboration. Whenever I faced scientific challenges, you are always there with constructive suggestions. You meticulously reviewed my papers before submission, always striving for excellence. Beyond academia, you have been a great friend, someone with whom I could have pleasant conversations, and you consistently extended your help whenever needed.

I would also like to thank Professor Christian Heipke for organizing the retreats at the Institute of Photogrammetry and GeoInformation at Leibniz University Hannover, and for always being available to provide timely support during my PhD studies.

I am deeply thankful to my colleagues in our research group: Dr. Sigrid Roessner, Dr. Chao Zhou, Dr. Mimi Peng, Dr. Zhuge Xia, Dr. Magdalena Stefanova Vassileva, Dr. Alina Shevchenko, Wandi Wang, Xiaohang Wang, Yufang He, Dibakar Kamalini Ritushree, Dr. Jun Ma, Juanjuan Yu, Pengcheng Sha, Shagun Garg, Dr. Haonan Jiang, Dr. Jianan Li, Yuyan Zhu, Dr. Yao Sun, Sen Lyv, Maoqi Liu, Weiwei Bian, and Dr. Yuankun Xu. I have learned so much from each of you during our group meetings, and your feedback and suggestions have been invaluable to my work. I also want to extend my gratitude to the people at Hannover University: Dr. Mahmud Haghshenas Haghighi, Andreas Piter, Sulaiman Fayez Hotaki, Yan Yang, Erik Rivas, Mingyue Ma and Imeime Uyo. Meeting you during the retreats always brought joy.

I would also like to extend my gratitude to my collaborators, Dr. Shaoyang Li, Dr. Guangyu Xu, and Prof. Jyr-Ching Hu. Our discussions always sparked new ideas, which greatly contributed to the refinement of my research.

I want to thank other colleagues from GFZ, Shanyu Zhou, Xiong Zhao, and Guosheng Gao. Special thanks to Xiong Zhao, the "head chef", for the delightful weekends spent together at your and Xiaohang's place — those gatherings remain some of the fondest memories of my academic journey. A heartfelt thanks to Xiaohang, Xiongzhao, Wandi, and Zhuge for their help during my time in the hospital when I broke my arm. Your support and encouragement helped me through those difficult times. I am especially grateful to Xiong and Xiaohang for bringing me meals every day during that tough period. I also want to express my appreciation to my friend Kunpeng Shi in China, who has been there for me since my master's studies. Whether in life or research, you've always offered your help when I needed it. I wish you all the best in your future endeavors.

I am particularly grateful to Sylvia Magnussen for your technical assistance with hardware and software in our section. Your prompt help saved me a lot of time. I also want to thank Christin Skala for your support with administrative tasks in the section.

I would like to express my sincere gratitude to the members of my doctoral examination committee: Prof. Dr.-Ing. habil. Christian Heipke and Prof. Dr.-Ing. Steffen Schön from Leibniz University Hannover, and Prof. Dr. Klaus Reicherter from RWTH Aachen University. Thank you for taking the time out of your busy schedules to review my dissertation and participate in my defense.

Finally, I want to express my heartfelt gratitude to my family. To my parents and grandmother, without your unwavering support, understanding, and help, I would never have been able to complete my PhD. I wish you all good health and happiness every day. I also want to thank my wife, Jing Wang. The four years of living apart in different countries have felt exceptionally long, yet you have always stood by me quietly, without a word of complaint. Thank you for your understanding and patience. And finally, to our cats, Maodou and Maoqiu — your companionship has made our little home incredibly warm and filled with love.

Thank you to everyone who has accompanied, encouraged, and supported me along the way.

Contents

List of Abbreviations

Abbreviation	Description
1D	1-Dimensional.
2.5D	2.5-Dimensional.
2D	2-Dimensional.
3D	3-Dimensional.
ALOS	Advanced Land Observing Satellite.
CIG	Computational Infrastructure for Geodynamics.
DEM	Digital Elevation Model.
DInSAR	Differential InSAR.
ERAI	ERA-Interim.
FEM	Finite Element Method.
GACOS	Generic Atmospheric Correction Online Service.
GCMT	Global Centroid Moment Tensor.
GNSS	Global Navigation Satellite System.
GPS	Global Positioning System.
HZF	High Zagros Fault.
InSAR	Interferometric Synthetic Aperture Radar.
IRSC	Iranian Seismological Center.
LOS	Line-of-Sight.
MERIS	Medium Resolution Imaging Spectrometer.
MFF	Mountain Front Fault.
MODIS	Moderate-Resolution Imaging Spectroradiometer.
MPSO	Multipeak Particle Swarm Optimization.
MRF	Main Recent Fault.
MT-InSAR	Multi-Temporal InSAR.
PS	Persistent Scatterer.
PS-InSAR	Persistent Scatterer Interferometric Synthetic Aperture Radar.
RMS	Root-Mean-Square.
SAR	Synthetic Aperture Radar.

Abbreviation	Description
SBAS	Small Baseline Subset.
SLAR	Side-Looking Aperture Radar.
SLC	Single Look Complex.
SRTM	Shuttle Radar Topography Mission.
SVD	Singular Value Decomposition.
USGS	U.S. Geological Survey.
VCM	Variance-Covariance Matrix.
WLS	Weighted Least Squares.
WRF	Weather Research and Forecasting.
ZFF	Zagros Foredeep Fault.
ZFTB	Zagros Fold-and-Thrust Belt.

1 Introduction

As it is well known, earthquake is one of the most catastrophic disasters to human. As shown in Figure 1.1, large earthquakes tend to occur at the plate boundaries or where tectonic movements are active. According to statistics of the U.S. Geological Survey (USGS), the earthquake frequency with magnitude greater than 6.0 is around 12 times per month from 1970 to 2024. The large-magnitude earthquakes occurring close to cities can cause catastrophic devastation by disrupting all activity within them. Those occurring near coastlines or under oceans could lead to secondary disasters such as tsunami, landslide or debris flow, often causing major human and economic losses. Thus, these disasters remind us of nature's power and have called into question our resilience to future events.

In term of crustal deformation, a complete earthquake cycle could be divided into four phases: interseismic, preseismic, coseismic and postseismic (Figure 1.2; Scholz, 2019). During the interseismic phase, rocks on both sides of a fault undergo continuous deformation due to ongoing geological forces (such as tectonic stress and plate movements), causing stress and strain accumulation along interplate and intraplate fault planes. When this stress reaches a critical state, it triggers rapid fault slip, creep, or aseismic slip. This stage typically occurs slowly and can last for decades, centuries, or even longer. In the preseismic phase, strain accumulation accelerates, but the duration is usually short, making it difficult to observe any significant surface deformation. During the coseismic phase, the accumulated stress during interseismic period reaches its limit and is suddenly released, leading to the fault rapid rupture and sudden strain energy release. Fault displacement on both sides induces permanent crustal deformation, accompanied by rapid seismic wave oscillations, causing transient changes in the stress state of the crustal medium. In the postseismic relaxation phase, residual strain energy caused by coseismic slip is released through stress coupling between the upper crust and the viscoelastic relaxation properties of the lower crust and upper mantle, as well as afterslip along fault planes and poroelastic rebound of crustal pore media. The surface deformation gradually recovers to a new equilibrium state and then begins the next interseismic strain accumulation phase.

Nowadays, space geodetic observation data, including the Global Navigation Satellite Systems (GNSS) and Interferometric Synthetic Aperture Radar (InSAR), particularly InSAR, offers researchers an unprecedented opportunity to study various phases of the earthquake cycle. These technologies enable all-weather, low-cost, wide-range and high-spatial-resolution observations that cover each stage of the earthquake cycle (Elliott et al., 2016a). By observing these earthquake phases, unifying the geological and geodetic results before, during, after, and between earthquakes, researchers can better understand crust-mantle evolution processes and assess seismic hazards.

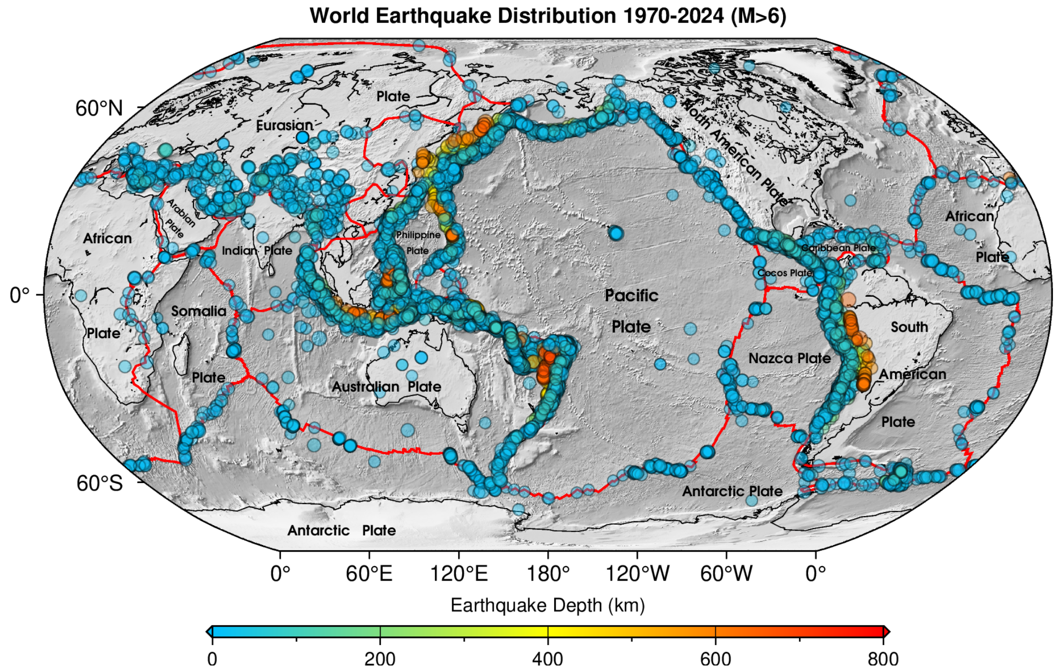

Figure 1.1: World earthquake distribution map from 1970 to 2024 for magnitudes greater than 6.0. The colored dots indicating the earthquakes which are sourced from the U.S. Geological Survey (USGS) earthquake catalog. The red lines represent plate boundaries from Bird (2003).

1.1 Study of Earthquake Cycle Deformation Using Satellite Geodesy

Usually we cannot find reliable pre-earthquake geodetic signals hours to days preceding a large earthquake (e.g., Roeloffs, 2006), and that is also one of the reasons why short-term warnings before the earthquake are very challenging. However, recent study of Bletery and Nocquet (2023) have observed a deformation which could be interpreted as accelerating slip near the hypocenters of 90 large earthquakes starting approximately 2 hour before the mainshocks by stacking high-rate GNSS time series around the world. But Hirose et al. (2024) found no acceleration-like deformation from 2 hour before the mainshock utilizing tiltmeter records and a similar stacking procedure. Thus, whether there is observable preseiemic signal remains an open question (Bürgmann, 2023).

Compared to the difficult-detectable preseismic signal, geodetic techniques have been widely and successfully used for capturing co-, post- and inter-seismic deformation. In the early 1990s, the Global Positioning System (GPS) was first used to measure the ground surface deformation associated with the 1989 Ms 7.1 Loma Prieta earthquake in California (Lisowski et al., 1990). A few years later, Massonnet et al. (1993) using InSAR observations showed exquisitely detailed coseismic deformation map of the 1992 Mw 7.3 Landers earthquake in the Mojave Desert in southern California. From then on, geodetic data have been widely used for 3-dimensional (3D) coseismic deformation capturing and coseismic slip modeling. Compared to GNSS data which can directly capture 3D displacement components, the conventional Differential InSAR (DInSAR) technique could only resolve 1-dimensional (1D) measurements in the Line-of-Sight (LOS) direction because of its side-looking geometry. Therefore, a large number of studies, including combination of multi-pass LOS and azimuth measurements, integration of InSAR and GNSS data, have been carried out to estimate the full 3D surface coseismic displacements in recent decades (e.g., Fialko et al., 2001; Wright et al., 2004; Hu et al., 2012), which is important to understand the role of earthquakes in topography building. After obtaining coseismic surface deformation data, optimization methods are often employed for finding the optimal parameters for the fault geometry. Then the fault plane can be divided into multiple sub-faults, and the Green's function is calculated using the dislocation theory and the coseismic slip distribution on the fault patches is ultimately determined (e.g., Jónsson et al., 2002; Ozawa et al., 2011; Guo et al., 2019). Because seismological data are global in coverage and has higher temporal resolution, it is also often jointly inverted with geodetic observations to solve the earthquake rupture process over second (e.g., Grandin et al., 2015; Lay, 2018). Coseismic fault slip and rupture process modeling is an important topic, as it establishes which portions of the fault ruptured and which did not, and we can identify regions of the fault system that have been brought closer to failure with stress changes calculation from slip distribution to update the estimate of regional seismic hazard.

Aseismic slip following large earthquakes, or postseismi deformation, proceed so slowly that slip is without radiating seismic waves, which make the mm-accuracy geodetic data an excellent observation to study the spatial variation of regionally lithospheric rheology and frictional properties on faults. There are several relaxation processes that follow earthquakes, which include continued aseismic afterslip on the fault plane, readjustment of groundwater following coseismic pressure changes (poroelastic deformation), and viscous flow in the lower crust and/or upper mantle (viscoelastic relaxation) (Bürgmann and Dresen, 2008). Afterslip along the fault planes primarily controls the rapid deformation in the near field over several years following an earthquake and provides crucial insights for understanding fault frictional behavior (e.g., Marone et al., 1991; Perfettini and Avouac, 2007; Barbot et al., 2009; Helmstetter and Shaw, 2009). Poroelastic rebound refers to the crustal deformation that occurs after a change in pore pressure gradient near the fault due to coseismic rupture (Jónsson et al., 2003; Peltzer et al., 1998). Viscoelastic relaxation primarily arises from the slow release of coseismic stress loading by the weaker lower crust or upper mantle, which mainly affects the intermediate to far-field regions of an earthquake and could lasts typically for several years, decades, or even centuries (Bürgmann and Dresen, 2008). The viscosity of the lower crust and upper mantle inferred by geodetic observations could provides key insights into the fault coupling and regionally rheological properties (e.g., Freed et al., 2006; Huang et al., 2014). However, clear separation of the appropriate model representations for these potential processes still remains a big challenge. For example, the well-studied postseismic mechanisms of the 1992 Mw 7.3 Landers earthquake, multiple different models or combination models have been proposed to explain the postseismic observations (e.g., Shen et al., 1994; Jónsson et al., 2003; Peltzer et al., 1998; Freed and Bürgmann, 2004).

Interseismic coupling is typically observed to be spatially heterogeneous, with locked patches where stress accumulates, which may be released in future earthquakes or aseismic transients, surrounded by regions of creeping events (Avouac, 2015). Now satellite geodesy has provided us an effective tool to monitor the crustal deformation caused by interseismic coupling. Interseismic response could result in centimeter or even millimeter motion of the earth's surface per year. Geodetic observations, especially Multi-Temporal InSAR (MT-InSAR) could provide large-scale small-magnitude deformation history on a successive

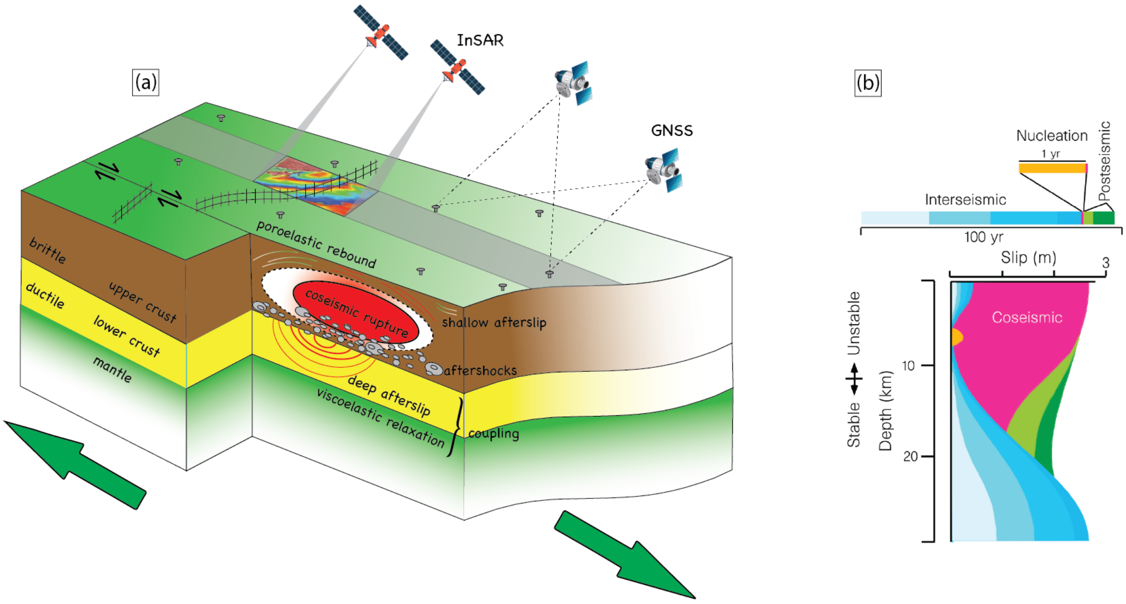

Figure 1.2: Earthquake cycle deformation and satellite geodesy application. (a) Conceptual cartoon modified from Elliott et al. (2016a) indicates satellite geodesy measuring the earthquake cycle. (b) The complete earthquake cycle and slip as a function of depth over the seismic cycle of a strike–slip fault. The figure is reproduced from Scholz (1998), with permission from Springer Nature.

time interval. The derived interseismic crustal deformation has been used to illuminate fault deformation rates and patterns and calculate the crustal strain-rate tensor, which is an important approach to estimating seismic hazard (e.g., Elliott et al., 2016a; Avouac, 2015). The long-term deformation rates of many major fault systems around the world have been studied using interseismic geodetic observations, for example, San Andreas Fault in eastern California (e.g., Fialko, 2006; Jolivet et al., 2009; Tong et al., 2013; Xu et al., 2021), North Anatolian Fault in eastern Turkey (e.g., Wright et al., 2001; Walters et al., 2011; Hussain et al., 2016; Bletery et al., 2020) as well as multiple faults (e.g., Haiyuan, Altyn Tagh, Xianshuihe and Kunlun faults) of Tibetan Plateau in China(e.g., Elliott et al., 2008; Jolivet et al., 2008; Cavalié et al., 2008; Wang et al., 2009; Zhao et al., 2022; Wu et al., 2024). They also have also been used to study the spatial variations in fault rheology and frictional properties (e.g., Kaneko et al., 2013; Jolivet et al., 2013; Qiao and Zhou, 2021), mapping variations in frictional coupling along subduction megathrusts (e.g., Jolivet et al., 2013; Wang et al., 2012; Moreno et al., 2018). Interseismic deformation information also provide an important tools to test whether the continental lithosphere deforms as a collection of many discrete blocks or as a continuous medium (the so-called block models and continuum models), for example, how Tibetan Plateau is formed and deformed under the collision of the Indian Plate with Eurasia has been a subject of extensive debate (e.g., Avouac and Tapponnier, 1993; Thatcher, 2007; Loveless and Meade, 2011; Flesch et al., 2001; Vergnolle et al., 2007; Fang et al., 2024).

In conclusion, with the advancement of satellite geodesy, we are able to obtain an increasing amount of observational data, which can be widely applied to the study of earthquake cycle deformation. Therefore, the development of satellite geodesy presents an excellent opportunity for us to gain a deeper understanding of the Earth's internal structure and the dynamics of seismic processes.

1.2 Research Objectives

As mentioned in previous sections, geodetic data has been widely applied in modeling deformation throughout the earthquake cycle. In this study, we use InSAR observations to investigate the coseismic and postseismic deformation characteristics associated with the 2017 Mw 7.3 Iran-Iraq border (Sarpol-e Zahab) earthquake, the largest recorded event in the Zagros Fold-and-Thrust Belt (ZFTB). We particularly focus on modeling the sources of coseismic and postseismic deformation, which is crucial for understanding deformation patterns and seismogenic structures in this region. The specific objectives of this study are as follows:

- Coseismic deformation modeling: This study uses InSAR data to obtain the coseismic deformation field and investigates the fault geometry and slip model of the event. Given the complexity of the fault system in the earthquake region, we aim to explore the relationship between the seismogenic fault and regional faults, which is crucial for assessing regional seismic hazard.

- Postseismic deformation modeling: This study delves into the primary mechanisms of postseismic deformation following this earthquake, focusing on afterslip modeling. We explore frictional afterslip, examining the complexities of fault friction and fault geometry during the postseismic deformation process.

- Crustal shortening and seismic-aseismic slip: Due to the collision between the Eurasian and Arabian plates, the deformation pattern of the Zagros Mountain belt is highly complex. By modeling both coseismic and postseismic deformation, we seek to better understand the relationship between crustal shortening and the seismic and aseismic slip associated with earthquakes in this region.

To address the above research objectives posed in this study, we conduct a detailed investigation of both coseismic and postseismic deformation for the 2017 Mw 7.3 Sarpol-e Zahab earthquake. The research is divided into two main parts (Figure 1.3):

- In the first part, beyond modeling coseismic deformation, we utilize InSAR observations to examine fault geometry and the evolution of postseismic deformation over the three years following the mainshock. In addition to kinematic afterslip, we focus on stress-driven afterslip evolution models. We develop a series of two-segment, stress-driven afterslip models and multisegment models with depth-varying frictional properties. Furthermore, we model postseismic viscoelastic deformation, investigating a combined model of afterslip and viscoelastic relaxation. Additionally, we explore downdip afterslip in detail, addressing existing debates about its presence in previous studies.

- Although the afterslip models developed in the first part largely explain the observed postseismic data, these mechanical afterslip models with friction variation tend to underestimate the early postseismic deformation to the west. This discrepancy may

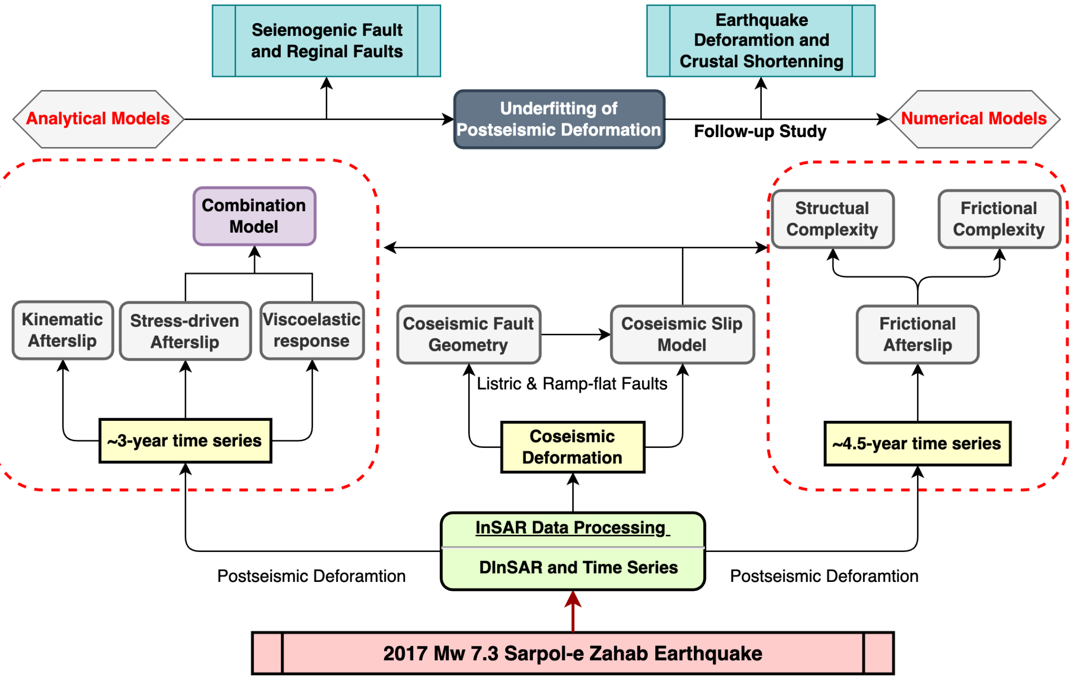

Figure 1.3: The research roadmap of this thesis.

suggest a more complex fault structure or more intricate fault friction than previously anticipated. Therefore, building on the foundation of the first part, we proceed to the second part of the study. In this part, we integrate 4.5 years of InSAR postseismic observations with 2D Finite Element Method (FEM) models incorporating various fault geometries, such as planar faults, ramp-flat faults, and combined ramp-flat and splay faults, to explore the frictional afterslip process driven by coseismic stress changes following the mainshock. We examine the complexity of fault friction and fault structure during the postseismic process. Using high-precision earthquake relocation data and geological cross-sections, we analyze the relationship between the seismogenic fault and known regional faults. Finally, we synthesize the results from both coseismic and postseismic modeling to further analyze the relationship between the coseismic and postseismic deformation of this earthquake and crustal shortening in the region.

1.3 Thesis Outline and Structure

The structure of this dissertation is organized as follows:

Chapter 1 is a Introduction. This chapter introduces the background and significance of the study, reviews the current state of research on earthquake cycle deformation modeling with satellite geodesy, and presents the research objectives and content of this study.

Chapter 2 is a overview of InSAR fundamentals. In this chapter, we briefly introduce the historical development of radar technology from Side-Looking Aperture Radar (SLAR) to Synthetic Aperture Radar (SAR), followed by the basic principles of InSAR and the main sources of errors. We then introduce several typical time-series InSAR techniques and conclude with a summary of the basic process for obtaining coseismic and postseismic deformation fields using InSAR observations.

Chapter 3 presents the theories of coseismic and postseismic deformation modeling. This chapter focuses on the theoretical background of modeling seismic deformation. It begins with an introduction to elastic dislocation theory and the basics of coseismic inversion, followed by a description of several typical mechanisms of postseismic deformation.

Chapter 4 introduces the earthquake case for this thesis — the 2017 Mw 7.3 Sarpol-e Zahab Earthquake. This chapter provides a brief overview of the tectonic background and current research on the 2017 Mw 7.3 Sarpol-e Zahab earthquake in the Zagros region.

Chapter 5 presents the coseismic and postseismic deformation modeling of the 2017 Mw 7.3 Sarpol-e Zahab earthquake using analytical solutions. InSAR data is used to obtain the coseismic deformation field and the postseismic deformation field over a three-year period. The coseismic slip model and postseismic deformation mechanisms are analyzed. For the postseismic sources, we simulate both kinematic and stress-driven afterslip, as well as combined models of afterslip and viscoelastic relaxation. Particular attention is paid to exploring the heterogeneity of fault friction during the postseismic process. Additionally, we conduct an in-depth analysis of downdip afterslip.

Chapter 6 is a further analysis based on the results from Chapter 5. Since the postseismic models obtained in Chapter 5 still struggle to fit the postseismic deformation field on the western side, this chapter explores the potential causes of this discrepancy. We reprocess the InSAR data to obtain 4.5 years of postseismic deformation data. Using 2-dimensional (2D) FEM models, we analyze models based on different fault geometries (including planar, ramp-flat, and combined models of ramp-flat and splay faults) and further explore the fault frictional properties associated with these geometries. Additionally, we discuss the relationship between the earthquake source fault and the existing faults in the region.

Chapter 7 is the conclusion and outlook. This chapter summarizes the research findings of this dissertation and discusses potential directions for future research.

2 InSAR Theory

2.1 Introduction

Geodesy is the science concerned with measuring and understanding the Earth's geometric shape, its orientation in space, and its gravity field, as well as monitoring changes in these properties over time. Within this broad discipline, InSAR geodesy refers specifically to the use of InSAR, a remote sensing technique, to measure 3D, time-dependent surface deformations of the solid Earth (Simons and Rosen, 2007). This method utilizes radar signals from satellites to monitor surface deformations with exceptional precision, achieving accuracies ranging from mm to cm over extensive areas. Its applications span critical geophysical phenomena such as earthquakes, landslides, volcanic activity, and land subsidence, providing high-resolution spatial and temporal data that enhance our understanding of the Earth's dynamic surface.

The operational mechanism of InSAR involves analyzing the phase difference between radar images to detect surface displacements. The accuracy of InSAR geodesy is typically reported in the range of mm to cm, depending on the application and error correction methods applied. For instance, for the C-band Sentinel-1 satellite, a displacement of about 2.8 cm generates one cycle of phase difference, and with advanced processing, accuracies of several millimeters can be achieved (Simons and Rosen, 2007). This precision is influenced by various factors, including atmospheric conditions (e.g., tropospheric and ionospheric delays), decorrelation effects (thermal, geometric, and noise-related), and systematic uncertainties in radar path delays and orbits.

To enhance accuracy, several methods are employed. For example, variance reduction by about half at 30 km wavelengths can be achieved using the high resolution weather model for wet delay correction (Foster et al., 2006). InSAR time-series analysis techniques, for example, stacking multiple interferograms could reduce tropospheric delay effects, which is useful for detecting small signals (Hanssen, 2001; Emardson et al., 2003). Ferretti et al. (2000) and Colesanti et al. (2003) utilized permanent scatter technique shows the measurement of subsidence rates of individual buildings at the level of less than 1 mm/yr, and seasonal effects due to groundwater withdrawal and recharge, respectively. Additionally, combining permanent scatter InSAR with GNSS data can also provide us high-accuracy displacement results. For example, Bürgmann et al. (2006) combined GPS-derived horizontal velocities and permanent scatter InSAR estimates of uplift in the San Francisco Bay Area to track tectonic uplift in areas not subject to seasonal effects, at an accuracy of better than 1 mm/yr. These techniques are crucial for applications such as monitoring interseismic deformation velocities and building subsidence rates with accuracies less than 1 mm/yr.

In the following sections, we provide a brief overview of the theoretical concepts related to InSAR. Due to space limitations, we have only covered the essential background and theories relevant to the processing of InSAR data in this thesis. For more comprehensive details on SAR and InSAR theories, readers are encouraged to consult specialized literature (e.g., Bürgmann et al., 2000; Hanssen, 2001; Ferretti et al., 2007; Lu and Dzurisin, 2014; Meyer, 2019).

- In Section 2.2, we first present the historical development from SLAR to SAR and briefly introduce current SAR development.
- Section 2.3 explains the basic principles of InSAR, discusses error sources and their mitigation.
- In Section 2.4, we review several widely used MT-InSAR techniques, including stacking, PS-InSAR and SBAS.
- Section 2.5 outlines the computational procedures used in this study for deriving coseismic and postseismic deformation fields from InSAR data.

2.2 Synthetic Aperture Radar (SAR) Basic

2.2.1 From Side-Looking Airborne Radar (SLAR) to SAR

A specific class of radar systems are the imaging radars, such as SLAR and later SAR. With the advancement of SLAR systems in the 1950s, the first airborne radar systems with reliable imaging capabilities were developed. The SLAR system consists of a radar sensor mounted on an airborne (or spaceborne) platform (Figure 2.1; Meyer, 2019). Radar antennas are usually placed on one side of a flight platform and the platform moves in a straight line at a certain altitude. The flight direction of the antenna is called the azimuth (or along-track direction), and the direction perpendicular to the flight direction of the antenna (which is consistent with the direction of radar wave emission) is called the range direction. As the aircraft moves along its flight path, it continuously illuminates a swath of the ground below, which is the antenna footprint.

The size of the instantaneous footprint (W_g and L_s in Figure 2.1) in both the range and azimuth directions is primarily determined by the relationship between the system's wavelength λ and the antenna's size L_a and L_e (which defines the antenna's beamwidth using $\beta = \lambda/L$ in that direction), as well as by the distance of the radar sensor from the ground R_0 and the incidence angle η:

$$L_s = \frac{\lambda R_0}{L_a} \tag{2.1}$$

$$W_g = \frac{\lambda R_0}{L_e \cdot \cos(\eta)} \tag{2.2}$$

Thus, we can see that the size of the antenna footprint is related to factors such as system wavelength, antenna size, incident angle, and slant range distance (Figure 2.1).

Objects at different ranges can be distinguished if the separation between them exceeds half the transmitted pulse length. Therefore, the slant range resolution of a SLAR system is defined as:

$$\rho_S = \frac{c \cdot \tau_p}{2} \tag{2.3}$$

where c represents the speed of light. The parameter ρ_S is commonly known as the slant range resolution of a SLAR system, as it reflects the system's ability to differentiate

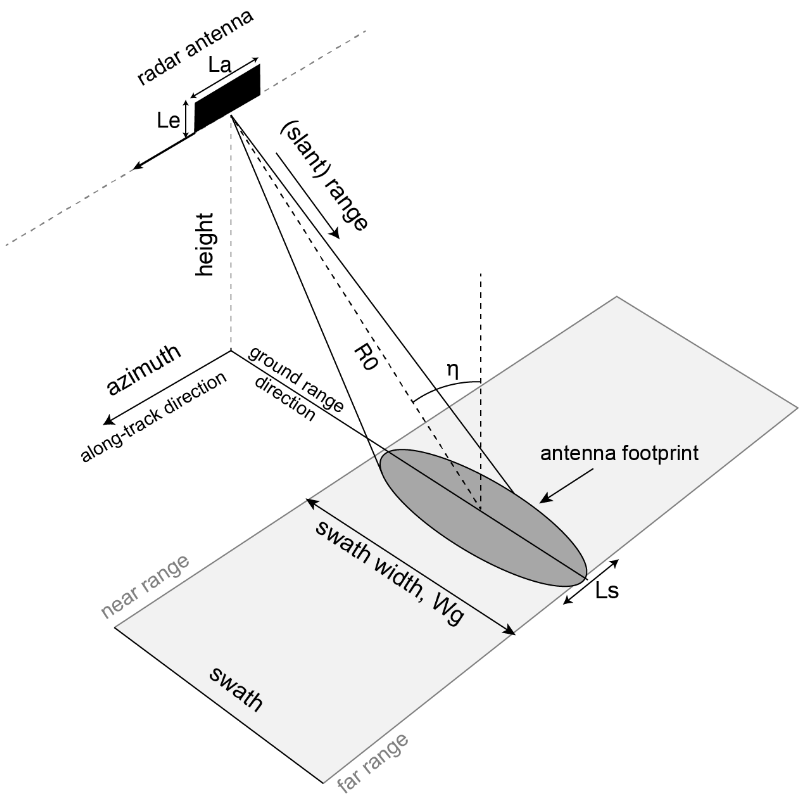

Figure 2.1: Simplified SLAR acquisition geometry.

between objects at varying slant distances from the radar (Figure 2.1). We can also derive the ground range resolution ρ_G from ρ_S using the local incidence angle η (Figure 2.1), which defines the system's ability to distinguish objects located on the ground:

$$\rho_G = \frac{\rho_S}{\sin\eta} = \frac{c \cdot \tau_p}{2\sin\eta} \tag{2.4}$$

From Equation 2.4 and Figure 2.1, we can see the value of ρ_G is not constant across the swath from near rang to far range direction.

In the along-track (or azimuth) direction, the radar scans the ground as it moves along its flight path. For SLAR systems, the azimuth resolution ρ_{AZ}, which refers to the ability to distinguish objects in the azimuth direction, is determined by the width of the antenna's footprint in the azimuth direction (L_s). This footprint width is constrained by the antenna's side length L_a along this axis. Therefore, the azimuth resolution can be expressed as:

$$\rho_{AZ} = L_s = \frac{\lambda R_0}{L_a} \tag{2.5}$$

Therefore, the spatial resolution in the azimuth direction (along the flight path) of the side-looking radar imaging system is limited by the antenna size, resulting in lower azimuth resolution, which often fails to meet practical application requirements. As shown in Equation 2.5, improving azimuth resolution can only be achieved by either increasing the antenna length or reducing the wavelength. However, in practice, shorter radar wavelengths are more susceptible to atmospheric interference, and the length of the antenna is constrained by the size of the flight platform, making it impractical to extend it too much.

Thus, SAR technique is developed to simulates an equivalent large-aperture antenna to enhance azimuth resolution. The principle of synthetic aperture essentially allows the creation of a longer effective antenna, known as a synthetic aperture, based on a series of acquisitions made by a shorter antenna as it moves along the flight path. Since antenna length is inherently related to the radar system's resolution capability, a longer antenna synthesized can even achieve high-resolution imaging on spaceborne platforms.

2.2.2 SAR Overview

During SAR imaging, the radar antenna transmits microwave signals, which pass through the atmosphere, interact with the Earth's surface, and reflect back to the sensor, capturing both intensity and phase information. This imaging process can be influenced by atmospheric refraction and observational noise (e.g., Bürgmann et al., 2000; Hanssen, 2001; Ferretti et al., 2007; Lu and Dzurisin, 2014). After data collection and processing, each pixel in a SAR image (Single Look Complex, SLC) contains both radar backscatter intensity (amplitude) and phase components related to the slant range. Each pixel in a SAR image is generally expressed in the complex form:

$$y = |y| \exp(j\varphi) \tag{2.6}$$

where y represents the intensity information, and φ represents the phase information (Hanssen, 2001). The intensity value indicates the degree of interaction between the signal and the ground surface. A higher amplitude reflects a stronger interaction, while a lower amplitude suggests a weaker one. In SAR images, the amplitude of the target is determined by the image resolution, target size, and the wavelength of the SAR sensor. Conversely, the phase difference can be used to ascertain the distance between the sensor and the ground pixel, facilitating accurate estimations of the surface's topography or displacement. Generally, when using natural terrain as a target, such as grass or forest trees, these targets are often smaller than the resolution cell. Consequently, the echoes received from a single pixel may be a combination of multiple individual echoes, leading to random variations in the phase values. Additionally, the amplitude may fluctuate significantly, resulting in speckle noise, which can be addressed through multi-looking processing.

By calculating the phase difference between corresponding pixels from two SAR images covering the same area, an interferometric phase image, or interferogram, can be obtained. Interferogram generation is a key focus in InSAR data processing and signal extraction. We will delve further into this topic in later sections. InSAR primarily revolves around extracting information from interferometric phase and coherence data.

Currently, satellite SAR imaging systems are advancing toward multi-platform, multi-band, multi-polarization, multi-mode, high spatial resolution, and high revisit frequency, providing excellent opportunities for expanding radar interferometry theory and applications. SAR spatial resolution has improved from tens of meters in early systems to the current 1-m range. Fully polarimetric satellite SAR systems are now operational, with sensors offering Spotlight, StripMap and ScanSAR imaging modes. Revisit times have reduced from tens of days to as short as a few days, or even one day (with multi-satellite constellation flights, Figure 2.2). Readers could refer to related publications for more details (e.g., Lanari et al., 2001; Eineder et al., 2009; Torres et al., 2012).

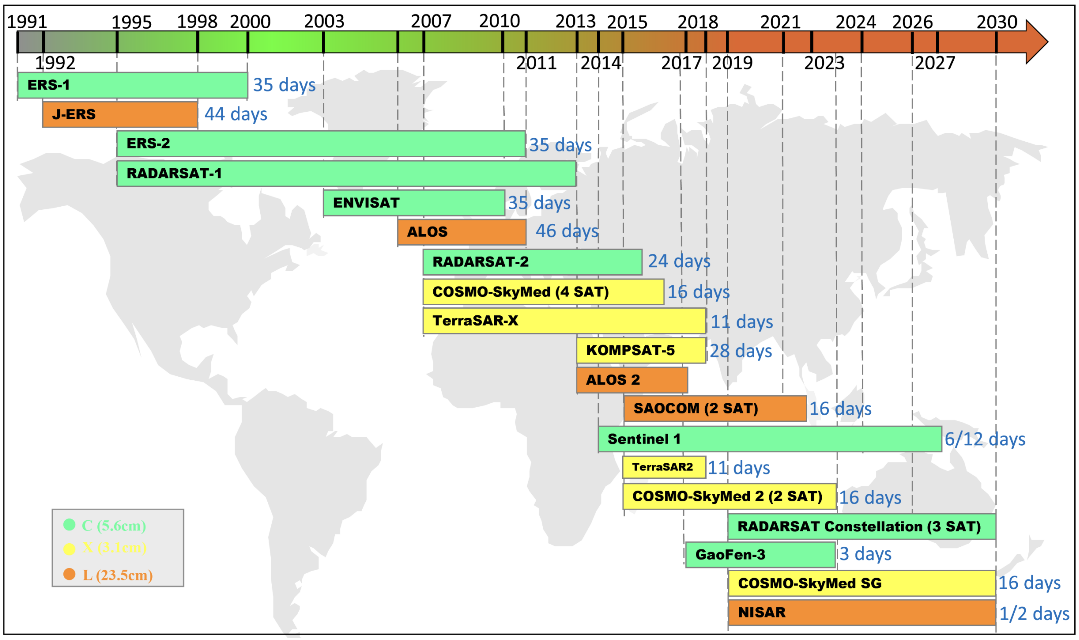

Figure 2.2: Part of past, current and upcoming spaceborne SAR missions, the duration at the end of each mission (days) is the repeat cycle of the satellites.

2.3 Interferometric Synthetic Aperture Radar (InSAR)

2.3.1 InSAR Principle

The phase information of SAR images is needed to generate interferogram. The SAR interferogram is created by pixel-wise cross-multiplying the first SAR image (y_1) with the complex conjugate of the second image (y_2) after aligning and resampling these two SAR images. As a result, the amplitude of the interferogram is the product of the amplitudes of both images, while its phase, known as the interferometric phase, represents the difference in phase between the two images (Ferretti et al., 2007):

$$v = y_1 y_2^* = |y_1||y_2| \exp\left[j(\varphi_2 - \varphi_2)\right] \tag{2.7}$$

and thus we could get the phase differences of the two images:

$$\varphi = \arctan(v) = \varphi_1 - \varphi_2 \tag{2.8}$$

The phase (φ) obtained through the interference of two SAR images from the same region can further be expressed as:

$$\varphi = \varphi_{\text{flat}} + \varphi_{\text{topo}} + \varphi_{\text{atm}} + \varphi_{\text{def}} + \varphi_{\text{noises}} \tag{2.9}$$

From this equation, it can be seen that the initial interferometric phase consists of the flat-earth effect phase (φ_{flat}), the topographic phase (φ_{topo}), the phase caused by surface deformation (φ_{def}), the atmospheric delay phase (φ_{atm}), and random noise (φ_{noises}). Therefore, in the practical application of crustal movement and deformation monitoring, to obtain the phase caused by crustal deformation, it is necessary to calculate and subtract the phases caused by other effects from the initial phase. The calculation methods for each phase component are introduced below.

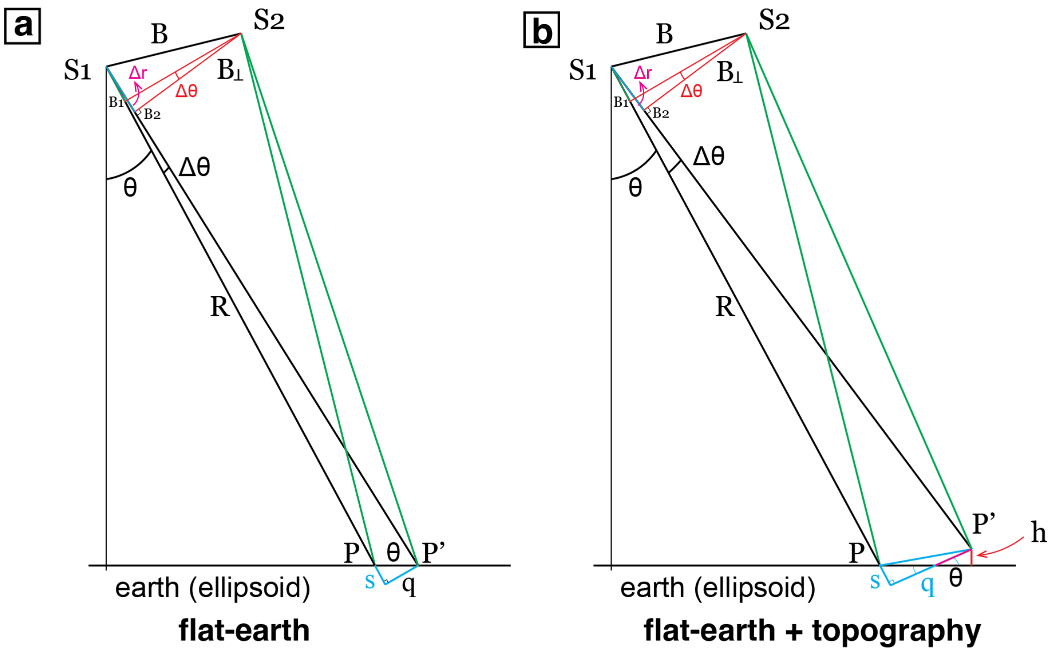

Figure 2.3: InSAR phase variation between two targets (P and P') and satellites ($S1$ and $S2$) with (a) flat earth and (b) topographic effects. R represents the slant range between the satellite and the ground target. The distance between SAR satellites $S1$ and $S2$ is baseline B, while $B_\perp$ represents the component perpendicular to the slant range direction. q and s are the distances between P and P' that are perpendicular and parallel to the slant range direction, respectively. This figure is modified from Lu and Dzurisin (2014).

Flat-Earth Effect Phase: The variation in satellite look angles (θ) causes the interferometric fringes to exhibit regular changes in both the range and azimuth directions. This type of deformation is known as the flat-earth effect phase. Based on the principles of interferometric measurement, even in the absence of topographic relief, the flat-earth effect will induce systematic phase changes on a reference surface (Figure 2.3a). Therefore, the flat-earth effect phase is also referred to as the reference ellipsoid phase. As is shown in Figure 2.3a, the flat-earth effect phase can be expressed as (Ferretti et al., 2007; Lu and Dzurisin, 2014):

$$\varphi_{\text{flat}} = -\frac{4\pi B_\perp s}{\lambda R \tan\theta} \tag{2.10}$$

where $B_\perp$ represents the component perpendicular to the slant range direction. R, λ and s are the slant range, system wavelength and distance between P and P' that is parallel to the slant range direction, respectively (Figure 2.3). The flat earth phase typically manifests as regular parallel fringes in the image.

Topographic Phase: As shown in Figure 2.3b, suppose the imaging target moves from the reference ellipsoid surface to a pixel point at a topographic height of h. In this case, the observed interferometric phase will then contain both the flat earth effect phase and the topographic phase. The topographic phase can be expressed as:

$$\varphi_{\text{topo}} = -\frac{4\pi B_{\perp} h}{\lambda R \sin\theta} \tag{2.11}$$

Crustal Deformation Phase: When the geometric position of a ground object changes relative to the sensor, it is referred to as deformation. The technique of measuring ground deformation through two or more interferometric measurements is known DInSAR. With the continuous development of SAR satellite and InSAR observation techniques, the capability of DInSAR to monitor surface deformation has been further improved. The deformation phase could be rewritten as:

$$\varphi_{\text{def}} = -\frac{4\pi}{\lambda}\Delta R \tag{2.12}$$

where ΔR is the deformation along the slant range direction.

Atmospheric Phase: When the SAR satellite radar signal passes through the atmosphere, variations in the refractive index cause the SAR signal to bend slightly along its propagation path, leading to deviations in the slant range and consequently resulting in phase delay. Since the phase changes caused by crustal deformation are obtained through the differencing of repeat images, atmospheric phase delay is caused by spatial and temporal variations in atmospheric conditions (such as temperature, pressure, etc.) between the two imaging times. If atmospheric conditions remain consistent in both space and time during the two imaging sessions, then DInSAR will not be affected by atmospheric phase delay. However, such consistent atmospheric conditions rarely exist in real observations. In extreme conditions, atmospheric phase delay can reach several tens of cm and may even obscure the real deformation signal, severely impacting the accuracy and reliability of InSAR in monitoring crustal deformation. The methods for correcting atmospheric phase delay will be discussed in subsequent sections.

Random Phase: Random phase noise is caused by the phase difference due to the thermal noise of the satellite system during the two imaging sessions. It also includes errors introduced during the data processing phase.

2.3.2 InSAR Error Sources

InSAR differential techniques have been widely applied in the fields of DEM reconstruction, geological disaster monitoring and early warning, and crustal movement and deformation. However, during actual observations and data processing, the interferometric phase is affected by various errors such as temporal and spatial decorrelation, orbital errors, atmospheric phase delay (tropospheric and ionospheric delays during SAR imaging), and phase unwrapping errors. Therefore, to improve the capability and reliability of InSAR deformation monitoring, it is necessary to adopt appropriate countermeasures to mitigate these errors.

2.3.2.1 Decorrelation Error

The coherence of an interferogram is an important indicator of the accuracy and reliability of InSAR deformation monitoring. Generally, the better the coherence of the interferogram, the higher the signal-to-noise ratio of the phase. Decorrelation includes both temporal and spatial decorrelation. Temporal decorrelation arises from changes in the scattering characteristics of ground targets during revisit periods, while spatial decorrelation is closely related to the spatial baseline of the satellite. Typically, a shorter temporal baseline leads to less variation in ground scatterers, and thus better coherence; similarly, a shorter spatial baseline results in better coherence. In practical applications, it is advisable to select interferometric pairs with shorter temporal and spatial baselines for processing. Furthermore, the penetration capability of the carrier signal is proportional to the radar wavelength. For example, the L-band ALOS-2 SAR images have a longer wavelength compared to the C-band Sentinel-1, allowing the signal to penetrate vegetation and reach the ground, thus maintaining good temporal coherence over longer periods. Therefore, the temporal coherence of long-wavelength radar waves is significantly higher than that of short-wavelength radar waves (Massonnet and Feigl, 1998). In addition, during data processing, it is advisable to apply filtering to the interferogram to suppress noise and improve the signal-to-noise ratio.

2.3.2.2 Digital Elevation Model Error

To obtain a differential interferogram, the topographic phase must be removed from the observed phase, and the most common technique for this is the two-pass differential technique. Using this technique, an external DEM is employed to simulate and subtract the topographic phase. However, errors in the external DEM data are inevitable, and according to the law of error propagation, these errors will directly affect the differential interferometric phase and the final deformation phase obtained. The phase variation caused by DEM errors can be expressed as:

$$\varphi_{\mathrm{dem}} = -\frac{4\pi B_{\perp}}{\lambda R \sin\theta} \cdot \Delta z \tag{2.13}$$

where Δz is the DEM error. Therefore, in DInSAR techniques, it is advisable to choose interferometric pairs with shorter perpendicular baselines. In addition, in MT-InSAR deformation analysis (discussed in later sections), DEM errors can also be treated as unknown parameters and estimated together with deformation parameters.

2.3.2.3 Orbital Error

Due to satellite orbit design or perturbations caused by the Earth's gravitational forces, there are usually deviations between the actual satellite orbit and the predicted orbit. This orbital deviation manifests as residual parallel fringes, with a gradual trend across space. Removing this trend is crucial for obtaining wide-area deformation fields. After phase unwrapping, the residual phase due to orbital errors must be addressed. A common method for removing orbital error phase is polynomial fitting of the residual phase in non-deforming areas. The residual orbital phase can be expressed as:

$$\varphi_{\mathrm{orbit}} = a_0 + a_1 x + a_2 y + a_3 x^2 + a_4 xy + a_5 y^2 \tag{2.14}$$

where φ_{orbit} represents the residual orbital phase, x and y are the pixel coordinates in the radar geometry, and a_i are the unknown parameters determined by least-squares fitting in non-deforming areas.

2.3.2.4 Atmospheric Phase Delay Error

Atmospheric phase delay is caused by the spatial and temporal variations in atmospheric conditions between two imaging times. It is one of the main error sources affecting InSAR deformation monitoring and a key challenge in high-precision InSAR data processing. When using InSAR to study significant deformation processes, such as large coseismic deformation, atmospheric errors are relatively small compared to surface deformation, and their presence does not significantly affect the study of the physical mechanisms involved. However, when InSAR is used to capture subtle postseismic or interseismic deformations, it becomes highly challenging because such deformations are minor, with low signal-to-noise ratios, making the deformation signals easily overwhelmed by noise. Therefore, precise treatment of atmospheric errors is necessary to ensure the accuracy of detecting small-scale deformations.

Atmospheric delay correction methods can be categorized based on the data sources used for correction as follows:

Terrain-related atmospheric delay correction methods: These methods assume that atmospheric phase delay is related to topography through a certain linear or power-law relationship. By estimating the correlation between phase and topography, the atmospheric phase delay is calculated. This method is widely used in studies of large-scale crustal deformation (such as coseismic deformation), but it does not account well for atmospheric turbulence (e.g., Bekaert et al., 2015).

Calibration techniques based on external data: These include using GNSS, ground meteorological data, Medium Resolution Imaging Spectrometer (MERIS), Moderate Resolution Imaging Spectrometer (MODIS), Weather Research and Forecasting model (WRF), and ERA-Interim (ERAI) digital atmospheric models (e.g., Yu et al., 2018; Li et al., 2003, 2011; Jung et al., 2013; Shamshiri et al., 2020).

Spatiotemporal statistical methods: Since atmospheric phase delay appears as a low-frequency signal in the spatial domain and a high-frequency signal in the temporal domain, the differences in the spatiotemporal statistical characteristics of these signals can be used to estimate atmospheric phase delay. Deformation, by contrast, shows low-frequency characteristics in both space and time. Related methods include interferogram stacking and spatiotemporal filtering (used in small baseline subset and permanent scatters InSAR). It is important to note that these methods typically require a certain number of interferograms and are thus only applicable to time-series InSAR analysis techniques (e.g., Zebker et al., 1997; Ferretti et al., 2000; Wright et al., 2001; Cao et al., 2018). We will introduce these techniques in a following Section.

2.3.2.5 Phase Unwrapping Error

The differential interferometric phase obtained from InSAR processing is wrapped within a limited range. To retrieve crustal motion and deformation characteristics, the phase must be unwrapped. Similar to resolving integer ambiguities in GNSS carrier phase measurements, InSAR phase unwrapping involves determining the number of whole phase cycles for each pixel in the interferometric phase map, converting the phase difference to the true phase. Unlike GNSS, where the integer ambiguity is estimated from continuous observations at the same point, InSAR's phase observations are discrete, acquired during satellite revisit cycles. The quality of phase unwrapping largely depends on the signal-to-noise ratio of the interferogram, which is affected by decorrelation, atmospheric phase delay, and other errors. This makes phase unwrapping more difficult, especially in low-coherence areas, where it can even fail. Phase unwrapping errors typically manifest as discontinuities or abrupt changes in the unwrapped phase. These errors can be detected using phase closure residuals (Biggs et al., 2007), where non-zero closure residuals indicate potential phase unwrapping errors in one or more interferograms. Once identified, the corresponding interferogram can be corrected. In practice, it is essential to select high-coherence interferograms for phase unwrapping. In the case of three-dimensional spatiotemporal unwrapping, unwrapping errors in low-coherence areas may propagate, causing the entire unwrapping process to fail. Additionally, applying filters to differential interferograms before unwrapping can improve the signal-to-noise ratio, increasing the likelihood of successful unwrapping.

2.4 Advanced Multi-temporal InSAR (MT-InSAR)

Time-series deformation observation is a widely applied technique primarily used to obtain high-precision surface deformation information. As discussed in the previous section, DInSAR investigates crustal motion and deformation by differencing two radar images acquired from repeat orbits. However, the capability of DInSAR is significantly limited when the study area is covered by snow, vegetation, or when the interferometric pair's spatial baseline exceeds the critical baseline length. Against this backdrop of DInSAR's limitations, MT-InSAR techniques were developed. MT-InSAR effectively overcomes challenges posed by spatial and temporal decorrelation, atmospheric delays, and DEM errors, greatly enhancing and expanding the application of InSAR technology in geoscience. The redundant observations in MT-InSAR over a time series allow it to mitigate the effects of orbit errors, atmospheric delays, DEM inaccuracies, and low coherence, thus enabling the detection of millimeter-scale, slow surface deformations. Over the past 20 years, MT-InSAR technology has undergone rapid development. In this section, we briefly introduce three key techniques: stacking (Sandwell and Price, 1998), Permanent Scatterer InSAR (PS-InSAR) (e.g., Ferretti et al., 2000), and Small Baseline Subset (SBAS) (e.g. Berardino et al., 2002).

2.4.1 Stacking

The simplest time-series InSAR technique is stacking. Stacking was first proposed by Sandwell and Price (1998), and its basic idea is that atmospheric noise exhibits high-frequency characteristics in the time domain with random properties, while deformation shows low-frequency, linear behavior over time. By linearly combining multiple interferograms, the atmospheric phase noise can be significantly reduced, thus improving the signal-to-noise ratio of the deformation signal. For a pixel in n interferograms, its interferometric phase and the temporal baseline of interferogram i are represented as φ^i and B_T^i. Then the linear rate of displacement of this pixel $\hat{v}$ is:

$$\hat{v} = \frac{1}{n}\Sigma_{i=1}^{n}\frac{\varphi^i}{B_T^i} \tag{2.15}$$

A good example is Wright et al. (2001) using InSAR stacking techniques to obtain the subtle interseismic deformation rate of the North Anatolian Fault in Turkey. However, stacking also has some limitations: (1) It assumes that crustal deformation follows a linear pattern, implying steady-state deformation, and thus overlooks potential non-steady-state changes, such as time-varying fault slip rates; (2) The technique also assumes that deformation persists long enough; otherwise, the calculated deformation rate will be underestimated; (3) It is worth noting that tropospheric delay errors are often correlated with topographic variations and cannot simply be considered as random errors. Therefore, mitigating systematic errors such as atmospheric errors before stacking interferograms can help to achieve a more accurate deformation rate field.

2.4.2 PS-InSAR

In 2000, Ferretti et al. (2000) proposed the Permanent Scatterer (PS) InSAR method. The basic principle of PS-InSAR is to use multiple SAR images covering the same area and, through statistical analysis of the amplitude and phase information of all the images, detect certain targets that maintain high coherence over time and space. These targets are referred to as persistent scatterers. Based on the phase time series of these PS targets, deformation and atmospheric delay information can be separated and modeled. Ground targets with radar backscatter characteristics that remain stable over time, such as man-made structures, exposed rocks, or artificial corner reflectors are typical PS points. These PS points are typically smaller than the spatial resolution unit of SAR images but dominate the backscatter signal within the resolution cell, allowing them to maintain high coherence even with large spatial baselines. In time-series datasets, even if no interferometric fringes are visible in individual interferograms, phase information at PS points can be interpolated or fitted to reconstruct the overall interferometric phase (primarily the low-frequency component). However, the conventional PS-InSAR method has limitations, as it discards targets that do not maintain coherence across all interferograms, which can limit its practical application.

2.4.3 SBAS

In 2002, Berardino et al. (2002) introduced the Small Baseline Subset (SBAS) method. Unlike the PS-InSAR method which uses a single master image to form interferometric pairs, SBAS employs a flexible combination of SAR images with spatial baseline thresholds, further mitigating the impact of spatial decorrelation. The fundamental principle is to generate pairs of differential interferograms from SAR images based on time and spatial baseline thresholds, then perform phase unwrapping and estimate unknown parameters such as DEM errors and linear deformation rates using least squares or Singular Value Decomposition (SVD). Finally, spatio-temporal filtering is applied to estimate nonlinear deformation and atmospheric phase components, resulting in an average deformation rate map and surface deformation time series. The SBAS time-series analysis process is shown in Figure 2.4.

SBAS generates a set of small baseline differential interferograms from time-series SAR data, allowing the estimation of deformation rates and time series for coherent surface targets. The key feature of SBAS is its full utilization of SAR data, enhancing both temporal sampling frequency and spatial coverage within the study area. SBAS applies to all image pixels that exhibit sufficiently high coherence, making the algorithm robust. Despite the use of small baseline data to limit topographic error, SBAS also accounts for DEM inaccuracies when generating differential interferograms. Moreover, the dense temporal and spatial information enables SBAS to effectively eliminate atmospheric phase

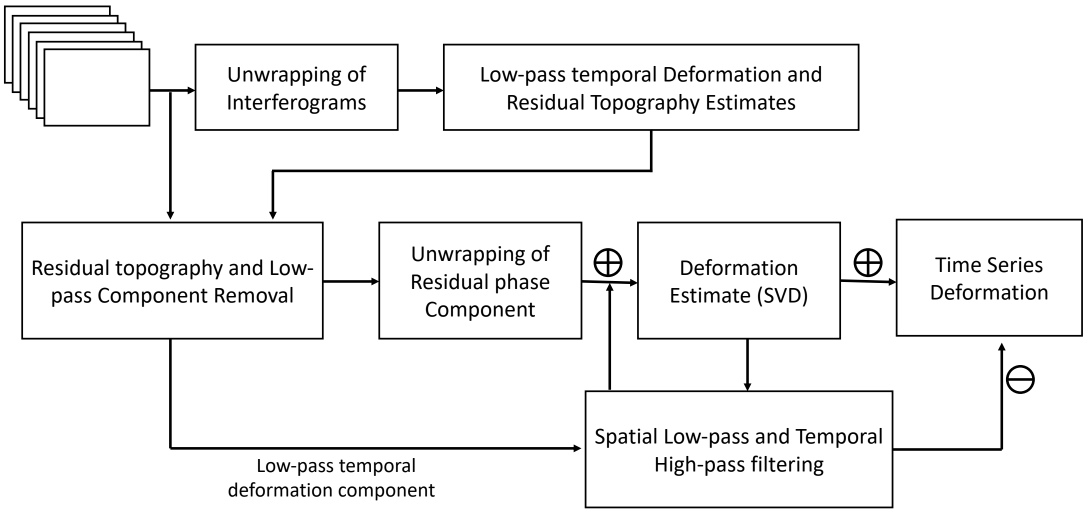

Figure 2.4: A simplified SBAS processing flowchart.

effects. In this study, we use SBAS to calculate postseismic time-series InSAR deformation (please see next section for details).

2.5 Co- and Post-seismic Deformation Retrieval

2.5.1 InSAR Coseismic Deformation

Coseismic deformation extraction primarily employs DInSAR technique using two images acquired before and after the earthquake along the same orbit, closely spaced in time. In this study, the two-pass DInSAR method is used to extract surface deformation information (Massonnet et al., 1993). This method involves processing two SAR images taken before and after the deformation event to generate an interferogram. With the aid of high-precision external DEM data for the region, the topographic phase is simulated, and differential processing is performed on the two interferograms to obtain the topographic phase. As described above, it is also necessary to mitigate or remove other disturbances, such as flat-earth effects, atmospheric influences, and satellite orbit errors, to extract precise phase information related to coseismic deformation. The coseismic deformation extraction process is briefly summarized as follows (Figure 2.5):

1. SAR Image Preprocessing: The raw observation files are converted into SLC images. This process includes spectrum estimation in both azimuth and range directions and range compression. The images are focused and compressed according to the SAR equation to generate SLC data.

2. Image Coregistration: SAR image coregistration involves coarse registration based on orbital information and fine registration using the coherence coefficient method. Coarse registration identifies common points in the master and slave images for

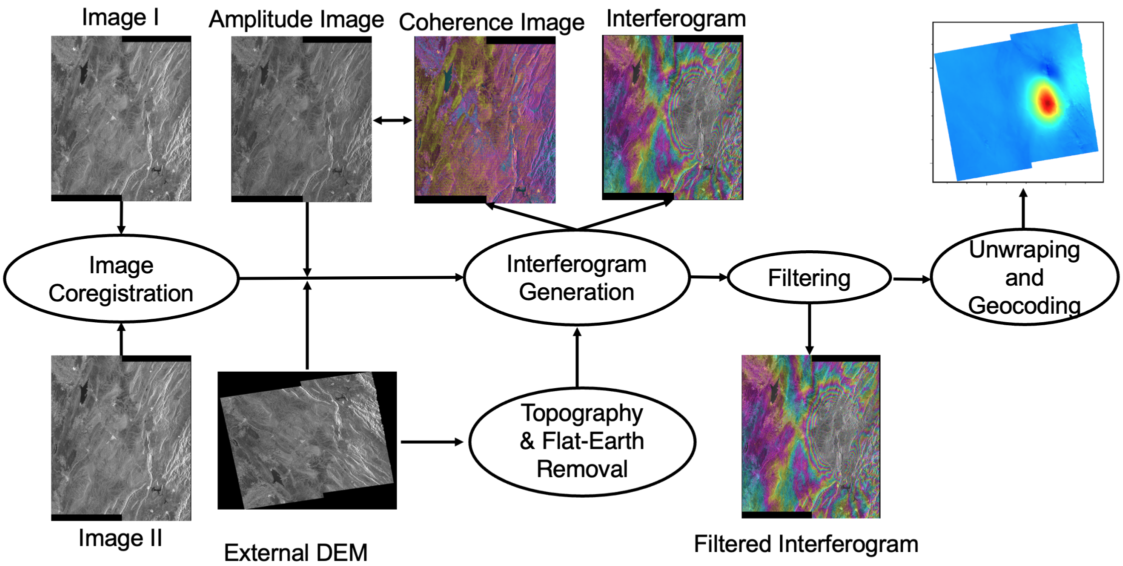

Figure 2.5: A simplified DInSAR data processing flowchart to get the coseismic deformation field of this 2017 Mw 7.3 Sarpol-e Zahab earthquake using a ascending Sentinel-1 image (T072A).

initial alignment, while fine registration uses more common points across the images, employing polynomial fitting to calculate offsets for accurate coregistration.

3. Interferogram Generation: The coregistered master and slave images are conjugately multiplied in phase to generate the interferogram. Due to the side-looking radar's observational method which causes inconsistent resolutions in the range and azimuth directions, multi-looking is applied to suppress noise and ensure that each pixel has consistent width and height.

4. Baseline Estimation: Baseline parameters directly affect the interferogram's coherence and the deformation monitoring results. Accurate baseline estimation is a critical step in the process.

5. Flat-Earth Effect Removal: The flat-earth effect, caused by the Earth's curvature, results in dense parallel fringes in the interferogram even in the absence of surface deformation. To remove the flat-earth phase, a short spatial baseline is selected, and appropriate algorithms are applied to eliminate this interference, leading to more accurate surface deformation information.

6. Topographic Phase Removal: By introducing simulated topographic phase data generated from an external DEM, the topographic phase component is removed from the interferogram.

7. Interferogram Filtering and Coherence Calculation: The interferogram is often affected by noise, so filtering is necessary to ensure the accuracy of subsequent data processing. Common filtering methods include adaptive filtering, median filtering, and mean filtering. Additionally, coherence is calculated to assess the quality of the data.

8. Phase Unwrapping: After removing various phases from the interferogram, phase unwrapping is required. This is a crucial step, involving algorithms such as branch-cut methods and minimum cost flow algorithms.

9. Geocoding: Using the conversion parameters between the radar coordinate system and the geodetic coordinate system obtained from the DEM, the deformation data is projected into the geodetic coordinate system.

2.5.2 InSAR Postseismic Deformation

This study employs the SBAS technique to determine postseismic time-series InSAR deformation. As mentioned earlier, the SBAS method collects a certain number of SAR images and controls the number of interferometric pairs based on predefined temporal and spatial baseline thresholds. The available SAR image data are paired into interferograms according to the preset thresholds, generating a series of short-baseline differential interferograms, successfully addressing the issue of temporal decorrelation. Deformation rates and time series could be obtained by using the SVD method. This technique effectively integrates long-term SAR images and creates more interferometric pairs, which significantly increases the temporal density of deformation monitoring and also mitigates atmospheric errors to a certain extent. This method has been widely applied in monitoring the evolution of interseismic and postseismic deformation (e.g., Fialko, 2006; Jolivet et al., 2015; Guo et al., 2022). The main workflow can be summarized as follows:

1. Acquire a time series of SAR images and designate one image as the master image. Register the other images to the master to generate interferograms.

2. Set appropriate temporal and spatial baseline thresholds and divide all SAR images into several small baseline subsets.

3. Perform interferometric processing on each image pair within the small baseline subsets to generate initial interferometric phases. Use external high-precision DEM data to remove topographic phases, obtain deformation phase maps, and perform phase unwrapping to derive deformation displacements.

4. Extract high-coherence points from the interferogram set and establish a deformation observation equation for the coherent point set. Using the SVD method, estimate surface deformation parameters and elevation errors based on the Weighted Least Squares (WLS) approach.

5. Reduce atmospheric errors through external atmospheric models (e.g., Yu et al., 2018).

In this chapter, we have only provided the basic InSAR theory related to obtaining the coseismic and postseismic deformation fields. The InSAR data processing results related to the 2017 Mw 7.3 Sarpol-e Zahab earthquake will be presented in Chapters 5 and 6. Readers could refer to those chapters for further details.

3 Co- and Post-seismic Deformation Modeling Theory

3.1 Introduction

To study crustal deformation and regional tectonic characteristics using surface deformation signals captured through geodetic techniques, it is essential to first model and analyze the data. For seismic events, a commonly used modeling approach is to infer the properties of the causative fault based on elastic half-space theory. Initially, the relationship between the fault's location and geometric parameters and the observed surface displacements is nonlinear. By employing any nonlinear problem-solving algorithm, we can invert the fault location and geometry from surface observations — a process referred to as source parameter inversion. Once the fault location and geometry are determined, a linear relationship exists between surface displacements and fault slip. Using least squares algorithms, the fault slip distribution can be inverted from surface displacement data — this is known as distributed slip inversion. The distributed slip results reflect the specific slip conditions of different parts of the fault plane, which are useful for analyzing asperities and barriers on the fault and serve as inputs for modeling postseismic deformation. Postseismic processes involve complex geophysical phenomena, including afterslip on the fault plane, viscoelastic relaxation of the lower crust and upper mantle, and poroelastic rebound of the surrounding medium. Modeling postseismic processes is crucial for understanding fault frictional properties and regional rheological structures.

In this chapter, we outline the fundamental theories of coseismic and postseismic deformation modeling. The main structure of this chapter is as follows:

- In Section 3.2, we begin with an introduction to basic elastic dislocation theory, including point source and finite rectangular dislocation models. We then briefly discuss the basic theories behind linear and nonlinear inversions of coseismic deformation.
- Section 3.3 introduces postseismic mechanisms such as poroelastic rebound, viscoelastic relaxation and afterslip.
- Section 3.4 presents a detailed introduction to the PyLith software and FEM modeling.

3.2 Coseismic Deformation Modeling

The theory of earthquake dislocation was originally developed from the elastic half-space dislocation model. In 1958, Steketee (1958) first introduced dislocation theory into seismology and derived the formulas for coseismic surface deformation caused by a point-source dislocation in a semi-infinite homogeneous medium model. Since then, numerous researchers have studied dislocation theory and resulted in many significant contributions. These include studies on the effects of lateral heterogeneity, vertical layers, surface topography, and Earth's curvature on coseismic surface deformation (Mansinha and Smylie, 1971; Sato, 1971; McGinley, 1969; Smylie and Mansinha, 1971; Chinnery and Jovanovich, 1972; Pollitz, 1996). In 1985, Okada (1985) built upon previous research and proposed formulas for calculating coseismic three-dimensional surface deformation and stress induced by both shear and tensile faults. Later, in 1992, Okada (1992) extended this model, making it capable of computing deformation and strain at any depth in a unified elastic half-space homogeneous medium dislocation model. The introduction of the Okada model had a significant impact on the inversion of source parameter distributions constrained by elastic dislocation models and geodetic data.

This section will primarily introduce the fundamentals of faults, elastic dislocation models, and fault parameter inversion.

3.2.1 Elastic Dislocation Basics

The fault plane can be regarded as a dislocation surface in an elastic half-space, and thus, dislocation surfaces can be used to simulate the deformation field caused by earthquakes. Steketee (1958) derived that the surface displacement u_i caused by the dislocation $\Delta u_j(\xi_1, \xi_2, \xi_3)$ across the fault plane Σ in an isotropic medium is:

$$u_i = \frac{1}{F} \iint \Delta u_j \left[\lambda \delta_{jk} \frac{\partial u_i^n}{\partial \xi_n} + \mu \left(\frac{\partial u_i^j}{\partial \xi_k} + \frac{\partial u_i^k}{\partial \xi_j} \right) \right] v_k d\Sigma \tag{3.1}$$

In the equation, δ_{jk} is the Kronecker delta, and λ and μ are the elastic parameters (Lame's constants) of the Earth's medium. v_k is the normal cosine of the dislocation element $d\Sigma$ on the fault plane. The term u_i^j refers to the displacement of the i-th component at the point (x_1, x_2, x_3) caused by the j-th component of a point source of amplitude F located at the point (ξ_1, ξ_2, ξ_3). By integrating the above expression over the dislocation surface, the surface deformation at a corresponding position can be obtained.

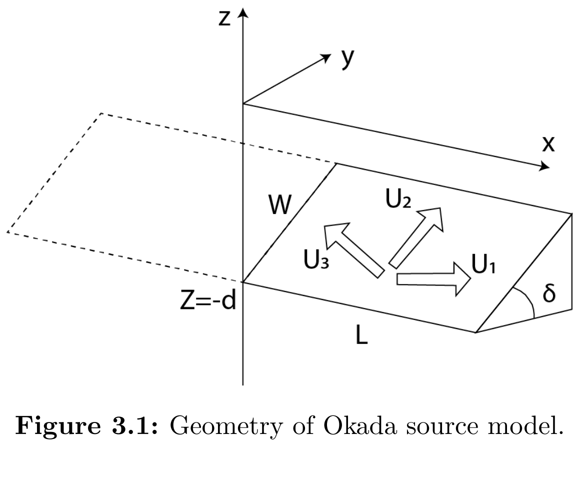

Figure 3.1: Geometry of Okada source model.

Okada (1985) summarized previous research and proposed a general analytical model for fault dislocation, providing formulas for calculating the displacement and strain at corresponding positions on the Earth's surface caused by fault dislocation. Using a Cartesian coordinate system, as shown in Figure 3.1, the fault coordinate system xyz is a right-handed system, with the origin located at the Earth's surface. The x-axis is parallel to the fault strike, the z-axis is perpendicular to the surface and points upward as positive. The slip on the fault plane is divided into strike-slip U_1, dip-slip U_2, and tensile-slip U_3. Additionally, L, W, d and δ denote the fault length, width, focal depth, and fault dip angle, respectively.

3.2.1.1 Point Source

In the Cartesian coordinate system of the Okada model, setting $\xi_1 = \xi_2 = 0$ and $\xi_3 = -d$, we can obtain the surface displacement caused by the point source at $(0, 0, -d)$. Using (x, y, z) instead of x_1, x_2, x_3, and denoting quantities related to the point source with a superscript 0, the expression for the displacement caused by the dislocation can be written as follows:

The surface displacement caused by a point source strike-slip dislocation can be expressed as follows:

$$\begin{cases} u_x^0 = -\dfrac{U_1}{2\pi}\left[\dfrac{3x^2q}{R^5} + I_1^0 \sin\delta\right]\Delta\Sigma \\ u_y^0 = -\dfrac{U_1}{2\pi}\left[\dfrac{3xyq}{R^5} + I_2^0 \sin\delta\right]\Delta\Sigma \\ u_z^0 = -\dfrac{U_1}{2\pi}\left[\dfrac{3xdq}{R^5} + I_4^0 \sin\delta\right]\Delta\Sigma \end{cases} \tag{3.2}$$

Surface displacement caused by a point source dip-slip dislocation:

$$\begin{cases} u_x^0 = -\dfrac{U_2}{2\pi}\left[\dfrac{3xpq}{R^5} - I_3^0 \sin\delta\cos\delta\right]\Delta\Sigma \\ u_y^0 = -\dfrac{U_2}{2\pi}\left[\dfrac{3ypq}{R^5} - I_1^0 \sin\delta\cos\delta\right]\Delta\Sigma \\ u_z^0 = -\dfrac{U_2}{2\pi}\left[\dfrac{3dpq}{R^5} - I_5^0 \sin\delta\cos\delta\right]\Delta\Sigma \end{cases} \tag{3.3}$$

Surface displacement caused by a point source tensile dislocation:

$$\begin{cases} u_x^0 = \dfrac{U_3}{2\pi}\left[\dfrac{3xq^2}{R^5} - I_3^0 \sin^2\delta\right]\Delta\Sigma \\ u_y^0 = \dfrac{U_3}{2\pi}\left[\dfrac{3yq^2}{R^5} - I_1^0 \sin^2\delta\right]\Delta\Sigma \\ u_z^0 = \dfrac{U_3}{2\pi}\left[\dfrac{3dq^2}{R^5} - I_5^0 \sin^2\delta\right]\Delta\Sigma \end{cases} \tag{3.4}$$

which

$$\begin{cases} I_1^0 = \dfrac{\mu}{\lambda+\mu} y \left[\dfrac{1}{R(R+d)^2} - x^2 \dfrac{3R+d}{R^3(R+d)^3}\right] \\ I_2^0 = \dfrac{\mu}{\lambda+\mu} x \left[\dfrac{1}{R(R+d)^2} - y^2 \dfrac{3R+d}{R^3(R+d)^3}\right] \\ I_3^0 = \dfrac{\mu}{\lambda+\mu} \left[\dfrac{x}{R^3}\right] - I_2^0 \\ I_4^0 = \dfrac{\mu}{\lambda+\mu} \left[-xy \dfrac{2R+d}{R^3(R+d)^2}\right] \\ I_5^0 = \dfrac{\mu}{\lambda+\mu} \left[\dfrac{1}{R(R+d)} - x^2 \dfrac{2R+d}{R^3(R+d)^2}\right] \end{cases} \tag{3.5}$$

$$\begin{cases} p = y\cos\delta + d\sin\delta \\ q = y\sin\delta - d\cos\delta \\ R^2 = x^2 + y^2 + d^2 = x^2 + p^2 + q^2 \end{cases} \tag{3.6}$$

3.2.1.2 Finite Rectangular Source

As seen in Figure 3.1, the surface displacement expression caused by a finite rectangular dislocation surface with length L and width W can be obtained by integrating the point source dislocation expressions over the finite rectangular dislocation surface. If the coordinates of any point within the rectangular dislocation surface are (ξ', η'), and they satisfy $0 < \xi' < L$ and $0 < \eta' < W$, then replacing $x - \xi'$, $y - \eta'\cos\delta$ and $d - \eta'\sin\delta$ with x, y and d, the following integral is performed:

$$\int_0^L d\xi' \int_0^W d\eta' \tag{3.7}$$

Perform the following transformation:

$$\begin{cases} x - \xi' = \xi \\ p - \eta' = \eta \end{cases} \tag{3.8}$$

in which p is same to that in Equation 3.6, then the above integration becomes:

$$\int_x^{x-L} d\xi \int_p^{p-W} d\eta \tag{3.9}$$

Finally, by performing the integration, the surface displacement formulas caused by rectangular dislocations in different directions can be obtained (Okada, 1985). The surface displacement caused by a strike-slip dislocation of a rectangular fault:

$$\begin{cases} u_x = -\dfrac{U_1}{2\pi}\left[\dfrac{\xi q}{R(R+\eta)} + \tan^{-1}\dfrac{\xi\eta}{qR} + I_1 \sin\delta\right]\Bigg\| \\ u_y = -\dfrac{U_1}{2\pi}\left[\dfrac{\tilde{y}q}{R(R+\eta)} + \dfrac{q\cos\delta}{R+\eta} + I_2 \sin\delta\right]\Bigg\| \\ u_z = -\dfrac{U_1}{2\pi}\left[\dfrac{\tilde{d}q}{R(R+\eta)} + \dfrac{q\sin\delta}{R+\eta} + I_4 \sin\delta\right]\Bigg\| \end{cases} \tag{3.10}$$

Surface displacement caused by a rectangular source dip-slip dislocation:

$$\begin{cases} u_x = -\dfrac{U_2}{2\pi}\left[\dfrac{q}{R} - I_3 \sin\delta\cos\delta\right]\Bigg\| \\ u_y = -\dfrac{U_2}{2\pi}\left[\dfrac{\tilde{y}q}{R(R+\xi)} + \cos\delta\tan^{-1}\dfrac{\xi\eta}{qR} - I_1 \sin\delta\cos\delta\right]\Bigg\| \\ u_z = -\dfrac{U_2}{2\pi}\left[\dfrac{\tilde{d}q}{R(R+\xi)} + \sin\delta\tan^{-1}\dfrac{\xi\eta}{qR} - I_5 \sin\delta\cos\delta\right]\Bigg\| \end{cases} \tag{3.11}$$

Surface displacement caused by a rectangular source tensile dislocation:

$$\begin{cases} u_x = \dfrac{U_3}{2\pi}\left[\dfrac{q^2}{R(R+\eta)} - I_3 \sin^2\delta\right]\Bigg\| \\ u_y = \dfrac{U_3}{2\pi}\left[\dfrac{-\tilde{d}q}{R(R+\xi)} - \sin\delta\left\{\dfrac{\xi q}{R(R+\eta)} - \tan^{-1}\dfrac{\xi\eta}{qR}\right\} - I_1 \sin^2\delta\right]\Bigg\| \\ u_z = \dfrac{U_3}{2\pi}\left[\dfrac{\tilde{y}q}{R(R+\xi)} + \cos\delta\left\{\dfrac{\xi q}{R(R+\eta)} - \tan^{-1}\dfrac{\xi\eta}{qR}\right\} - I_5 \sin^2\delta\right]\Bigg\| \end{cases} \tag{3.12}$$

where

$$\begin{cases} I_1 = \dfrac{\mu}{\lambda+\mu}\left[\dfrac{-1}{\cos\delta}\dfrac{\xi}{R+d}\right] - \dfrac{\sin\delta}{\cos\delta} I_5 \\ I_2 = \dfrac{\mu}{\lambda+\mu}[-\ln(R+\eta)] - I_3 \\ I_3 = \dfrac{\mu}{\lambda+\mu}\left[\dfrac{1}{\cos\delta}\dfrac{\tilde{y}}{R+\tilde{d}} - \ln(R+\eta)\right] + \dfrac{\sin\delta}{\cos\delta} I_4 \\ I_4 = \dfrac{\mu}{\lambda+\mu}\dfrac{1}{\cos\delta}[\ln(R+\tilde{d}) - \sin\delta\ln(R+\eta)] \\ I_5 = \dfrac{\mu}{\lambda+\mu}\dfrac{2}{\cos\delta}\tan^{-1}\dfrac{\eta(X+q\cos\delta)+X(R+X)\sin\delta}{\xi(R+X)\cos\delta} \end{cases} \tag{3.13}$$

and if the fault dip angle is 90°, that is $\cos\delta = 0$, then

$$\begin{cases} I_1 = -\dfrac{\mu}{2(\lambda+\mu)}\dfrac{\xi q}{(R+\tilde{d})^2} \\ I_3 = \dfrac{\mu}{2(\lambda+\mu)}\left[\dfrac{\eta}{R+\tilde{d}} + \dfrac{\tilde{y}q}{(R+\tilde{d})^2} - \ln(R+\eta)\right] \\ I_4 = -\dfrac{\mu}{\lambda+\mu}\dfrac{q}{R+\tilde{d}} \\ I_5 = -\dfrac{\mu}{\lambda+\mu}\dfrac{\xi\sin\delta}{R+\tilde{d}} \end{cases} \tag{3.14}$$

$$\begin{cases} p = y\cos\delta + d\sin\delta \\ q = y\sin\delta - d\cos\delta \\ \tilde{y} = \eta\cos\delta + q\sin\delta \\ \tilde{d} = \eta\sin\delta - q\cos\delta \\ R^2 = \xi^2 + \eta^2 + q^2 = \xi^2 + \tilde{y}^2 + \tilde{d}^2 \\ X^2 = \xi^2 + q^2 \end{cases} \tag{3.15}$$

where the symbol $\|$ in the formula represents the Chinnery operator, which can be expressed as follows:

$$f(\xi,\eta)\| = f(x,p) - f(x,p-W) - f(x-L,p) + f(x-L,p-W) \tag{3.16}$$

The four terms on the right side of Equation 3.16 represent the displacements caused by the four vertices of the rectangle.

3.2.2 Coseismic Fault Slip Inversion

The source parameter inversion constrained by geodetic data includes the inversion of fault geometry parameters based on uniform slip and the inversion of fault non-uniform slip parameters. This is also known as the two-step method: nonlinear inversion and linear inversion, where nonlinear inversion determines the fault's geometric parameters, and linear inversion determines the slip distribution on the fault plane.

3.2.2.1 Fault Geometry Parameters Inversion

Nonlinear inversion refers to uniform slip inversion, primarily used to invert fault geometry parameters, including fault location, fault depth, strike, dip, fault length, width, and slip angle. The Green's function links surface displacements to the Okada model (Okada, 1985). However, the Okada model involves many parameters, making the inversion problem highly nonlinear. Therefore, forward modeling of surface deformation using different fault geometry parameters is required. By constructing forward simulations of surface deformation based on different fault parameters, the fault parameters that produce the smallest residual between simulated and observed values are selected as the optimal fault parameters. Hence, this process is also known as nonlinear inversion of source parameters. The relationship between fault slip and surface observations is generally expressed as follows:

$$d = G(M) \tag{3.17}$$

where d represents the surface deformation, M represents the fault geometry parameters, and G represents the Green's function matrix, which is used to represent the deformation at specific surface locations caused by unit slip on the fault. There are various algorithms for nonlinear inversion, including simulated annealing, genetic algorithms, particle swarm optimization, artificial neural networks, and multi-scale inversion methods.

3.2.2.2 Fault Slip Distribution Inversion

Due to the complexity of the earthquake rupture process, uniform slip inversion is unable to accurately depict the slip distribution on the fault plane. Therefore, the fault plane can be divided into several rectangular elements, and the slip on each fault element can be obtained through linear inversion. The mathematical model for linear inversion can be constructed using the following formula:

$$d = Gm \tag{3.18}$$

where d represents the surface displacement observed by geodetic observations like InSAR and GNSS, m is the slip on the fault elements, and G is the Green's function matrix (the surface deformation values corresponding to unit dislocation on the fault plane) which could be represented as follow:

$$G = \begin{bmatrix} ss_1^1 & ds_1^1 & ss_1^2 & ds_1^2 & \dots & ss_1^n & ds_1^n \\ ss_2^1 & ds_2^1 & ss_2^2 & ds_2^2 & \dots & ss_2^n & ds_2^n \\ \dots & \dots & \dots & \dots & \dots & \dots & \dots \\ ss_k^1 & ds_k^1 & ss_k^2 & ds_k^2 & \dots & ss_k^n & ds_k^n \end{bmatrix} \tag{3.19}$$

where ss_k^n and ds_k^n represent the contributions of the strike-slip component and dip-slip component on nth fault patch to kth observation point, respectively. The least squares principle is used to determine the optimal fault slip model, where the smoothing factor is adjusted to minimize the residuals between the observed values and the model, thus obtaining the optimal slip model. The mathematical model can be expressed as follows:

$$\Gamma = \min(\|W(Gm - d)\|_2 + \kappa^2 \|Lm\|_2) \tag{3.20}$$

In this equation, $\|\|_2$ denotes the Euclidean norm, W represents the weight matrix for the observed values, G is the Green's function matrix, m is the slip on each fault element, d is the observed value vector, L is the second-order finite difference Laplacian operator, and κ^2 is the smoothing factor.

3.3 Postseismic Deformation Modeling

The postseismic relaxation process is considered to include poroelastic rebound, aseismic afterslip, and viscoelastic relaxation, lasting from several months to hundreds of years, and spatially spreading from a few kilometers to hundreds of kilometers (e.g., Pollitz, 2003; Freed and Bürgmann, 2004; Savage and Langbein, 2008; Jónsson et al., 2003). In this section, we will introduce these mechanisms causing postseismic relaxation deformation. We will begin with a brief introduction to poroelastic rebound, followed by a discussion on viscoelastic relaxation, and finally, we will focus on the modeling of afterslip on fault planes.

3.3.1 Poroelastic Rebound

Poroelastic deformation refers to the ground deformation caused by pore elastic flow within a medium driven by coseismic stress changes. Generally, when the compactive and extensional regions induced by seismic activity in the shallow crust surrounding a fault drive pore fluid flow, poroelastic rebound occurs. Since the duration of an earthquake is very short, the initial stage following rupture is referred to as the "undrained" condition, where there is essentially no fluid movement. Over time, the pore pressure gradient drives water to enter the "drained" condition, during which fluid pressure equilibrium is reestablished, meaning that water flows from areas of high pore pressure to areas of low pore fluid pressure. Typically, these two states can be distinguished by the shear modulus and Poisson's ratio of the elastic medium.

In simulating poroelastic rebound deformation, different Poisson's ratios are often used, and surface deformation is modeled through a dislocation model. The difference in deformation between the two states is then calculated to simulate the surface deformation caused by poroelastic rebound (e.g., Peltzer et al., 1996; Jónsson et al., 2003):

$$u_{\mathrm{poro}}(x, y) = u(x, y; \nu_{\mathrm{undrained}}) - u(x, y; \nu_{\mathrm{drained}}) \tag{3.21}$$

where $u_{\mathrm{poro}}(x, y)$ represents the deformation from the poroelastic rebound mechanism at the ground station coordinates (x, y), $\nu_{\mathrm{undrained}}$ and ν_{drained} are the Poisson's ratios under undrained and drained conditions, respectively, $u(x, y; \nu_{\mathrm{undrained}})$ and $u(x, y; \nu_{\mathrm{drained}})$ are the modeled surface displacements under undrained and drained conditions, respectively. From the above equation, it can be seen that, in addition to the Poisson's ratio, the magnitude of deformation caused by pore rebound also depends on the coseismic rupture model. Poroelastic rebound deformation generally concentrates in the near-fault area and is typically small in magnitude (on the order of several centimeters). Poroelastic rebound also exhibits certain time decay characteristics, as it is a gradual recovery process, but it generally lasts only a few months (Jónsson et al., 2003).

3.3.2 Viscoelastic Relaxation

Similar to poroelastic rebound, the coseismic stress changes induced by an earthquake may also load the lower crust and upper mantle, leading to viscoelastic deformation. Viscoelastic relaxation is typically thought to occur over a longer timescale than afterslip and poroelastic rebound, meaning it only becomes more significant after long-term deformation (years). In addition to the coseismic fault slip distribution, the primary factors controlling viscoelastic relaxation include characteristics of the Earth model, such as the thickness of elastic and viscoelastic layers, lateral rheological structures, and viscosity variations. Postseismic deformation data contains valuable information about the rheological structure of the lithosphere, and through reasonable subdivision of the lithospheric layers, postseismic deformation can be used to estimate the lithosphere's rheological properties. The mechanical properties of viscoelastic solids are generally described by two parameters: elastic modulus and viscosity. For viscoelastic bodies, the internal stress has a constitutive relationship with both strain and strain rate. Currently, three main rheological models are applied in the study of postseismic deformation dynamics: the Maxwell model, the Kelvin (Voigt) model, and the Burgers model.

3.3.2.1 Maxwell Model

The one-dimensional viscoelastic structure of a Maxwell body is composed of an elastic spring in series with a viscous dashpot (Figure 3.2; Karato, 2008). Under external force, the spring and dashpot experience the same stress, and the total strain of the deformed body is the sum of the deformations of the two components ($\epsilon = \epsilon_{\mathrm{spring}} + \epsilon_{\mathrm{dashpot}}$). The

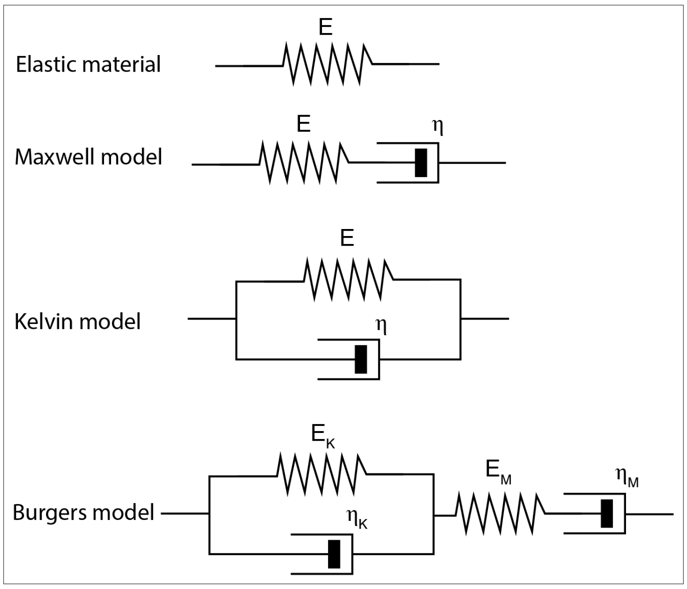

Figure 3.2: Various models of elastic and non-elastic deformation. E and η represent Young's modulus and viscosity coefficient, respectively.

stress-strain relationship can be described as follows (in a one-dimensional medium, the elastic parameter is represented by Young's modulus E; however, in a three-dimensional medium, the shear modulus μ is used instead of Young's modulus E to characterize the viscous deformation caused by shear forces):

$$\dot{\epsilon} = \frac{\sigma}{\eta} + \frac{\dot{\sigma}}{E} \tag{3.22}$$

where σ is the stress, η is the viscosity, $\dot{\epsilon}$ and $\dot{\sigma}$ represent the time derivatives of strain and stress, respectively. The spring responds instantaneously to stress loading, and the initial strain is elastic strain. Over time, due to viscous deformation, the strain increases linearly, and the deformation formula can be expressed as:

$$\epsilon(t) = \frac{\sigma}{E}(1 + \frac{t}{\tau_M}) \tag{3.23}$$

where $\tau_M = \eta/E$ is the Maxwell time. At the Maxwell time, the viscous strain becomes comparable to the elastic strain. This model is well-suited for materials where elastic and viscous deformations occur independently. Therefore, it effectively describes the instantaneous displacement during an earthquake and the long-term cumulative displacement after the event.

3.3.2.2 Kelvin Model

The one-dimensional structure of a Kelvin body is represented by a spring and a dashpot in parallel (also known as the Voigt model). In the parallel configuration of the Kelvin rheological body, viscous and elastic deformations are coupled. The strain in the elastic and viscous parts must be the same ($\epsilon = \epsilon_{\text{spring}} = \epsilon_{\text{dashpot}}$), and the total strain is shared by both components. The stress-strain relationship can be described as:

$$\sigma = E\epsilon + \eta\dot{\epsilon} \tag{3.24}$$

For the Kelvin model, the strain will reach a finite value over an infinite time, and it cannot exceed the elastic deformation of the spring itself. As shown in the following equation:

$$\epsilon(t) = \frac{\sigma}{E}[1 - \exp(-\frac{t}{\tau_M})] \tag{3.25}$$

The characteristic time to reach a finite limiting strain is the same as the Maxwell time defined earlier $\tau_M = \eta/E$. The Kelvin model does not exhibit instantaneous deformation because the deformation of the viscous element takes time to develop, which results in an infinite instantaneous elastic constant, even though this is physically unrealistic. The strain variation over time in the Kelvin body starts from zero and increases to a maximum value, with the strain rate gradually decreasing over time. This model is useful for describing the short-term effects in postseismic deformation.

3.3.2.3 Burgers Model

The one-dimensional structure of the Burgers rheological model consists of a Maxwell body and a Kelvin body in series. The shear modulus of the Maxwell body and the Kelvin body is usually kept equal. The constitutive stress-strain relationship of the Burgers body is as follows:

$$\begin{cases} \epsilon = \epsilon_{\mathrm{M}} + \epsilon_{\mathrm{K}} \\ \sigma = \sigma_{\mathrm{M}} = \sigma_{\mathrm{K}} \end{cases} \tag{3.26}$$

The comprehensive stress-strain relationship can be expressed as:

$$\sigma + \left(\frac{\eta_K}{E_K} + \frac{\eta_M}{E_K} + \frac{\eta_M}{E_M}\right)\dot{\sigma} + \frac{\eta_K}{E_K}\frac{\eta_M}{E_M}\ddot{\sigma} = \eta_M\dot{\varepsilon} + \frac{\eta_K\eta_M}{E_K}\ddot{\varepsilon} \tag{3.27}$$

The viscoelastic deformation response of the Burgers body is the sum of the deformation effects of the Maxwell and Kelvin bodies. Under a sudden stress load, the deformation response of the surrounding rock exhibits characteristics similar to the instantaneous step displacement during an earthquake, a rapid viscoelastic relaxation response shortly after the earthquake, and long-term cumulative deformation.

The calculation methods for viscoelastic relaxation deformation typically include analytical (semi-analytical) methods and numerical simulations. An example of an analytical model is the simulation of postseismic effects of an infinite strike-slip fault, where an elastic layer overlies a homogeneous viscoelastic half-space Earth model (Nur and Mavko, 1974; Savage and Prescott, 1978). Wang et al. (2006) adopted a semi-analytical method and developed the PSGRN/PSCMP program in Fortran to simulate the response of a layered viscoelastic model to coseismic stress loading. This program is based on the theory of viscoelastic-gravitational dislocation, taking into account the vertical layering differences in viscous materials. It can simultaneously simulate postseismic deformation, geoid changes, and gravity variations.

Pure numerical models primarily include the FEM models for power-law rheology (Hearn et al., 2002; Freed and Bürgmann, 2004). FEM is a highly efficient computational method that solves differential or integral equation systems using numerical techniques. Its modeling foundation lies in discretizing a continuous large element into a finite number of smaller elements, followed by iterative numerical calculations on each element using the computational power of modern computers. A widely used finite element numerical simulation software is PyLith (Aagaard et al., 2013), developed by the Computational Infrastructure for Geodynamics (CIG). In this thesis, to simulate the viscoelastic response after the 2017 Sarpol-e Zahab earthquake, we used the Maxwell rheological model along with the PSGRN/PSCMP and PyLith software to simulate the postseismic viscoelastic contribution. A more detailed introduction to the PyLith software will be provided in Section 3.4.

3.3.3 Afterslip

The postseismic afterslip model is one of the most commonly used mechanisms to explain postseismic deformation. This is primarily due to the stress perturbation caused by the coseismic slip distribution on the fault, leading to aseismic slip in areas surrounding the coseismic rupture. Postseismic afterslip modeling can generally be divided into kinematic afterslip and physical afterslip. In this section, we will give a brief introduction of these afterslip models.

3.3.3.1 Kinematic Afterslip

The process of calculating kinematic afterslip (free afterslip) is similar to the linear inversion used to obtain the coseismic fault slip distribution. This requires calculating the Green's function for rectangular dislocation elements on the fault plane, using postseismic deformation observations to invert the fault slip during the postseismic period. Compared to stress-driven afterslip, kinematic inversion has more free parameters, which often allows for a better fit to the observational data, although it may sometimes produce non-physical solutions (Zhao et al., 2017; Guo et al., 2022). The results of kinematic afterslip inversion are highly sensitive to the quantity, quality, and spatial distribution of data, as well as the assumptions and smoothing applied to the model. Nevertheless, its intuitive mapping capability enables us to make the most of the information contained in the data. Therefore, although kinematic afterslip does not have a clear physical interpretation, it still provides valuable insight into the location of afterslip and can complement and validate physical afterslip models.

3.3.3.2 Stress-driven Afterslip

The process of earthquake rupture, propagation, and termination is primarily controlled by the mechanical properties and frictional characteristics of the rocks on the fault plane. There are several forms of rate-and-state constitutive law that have been used to model laboratory observations of rock friction, for example, the Dieterich (or aging) law and the Ruina (or slip) law (Dieterich, 1979; Ruina, 1983). Here we give the Dieterich law as an example (Figure 3.3, the readers could refer to the related papers (e.g., Scholz, 2019) for more details):

$$\begin{cases} \mu = \mu(V,\theta) = \mu_0 + a\ln\dfrac{V}{V_0} + b\ln\dfrac{V_0\theta}{D_c} \\ \dot{\theta} = \dfrac{d\theta}{dt} = 1 - \dfrac{V\theta}{D_c} \end{cases} \tag{3.28}$$

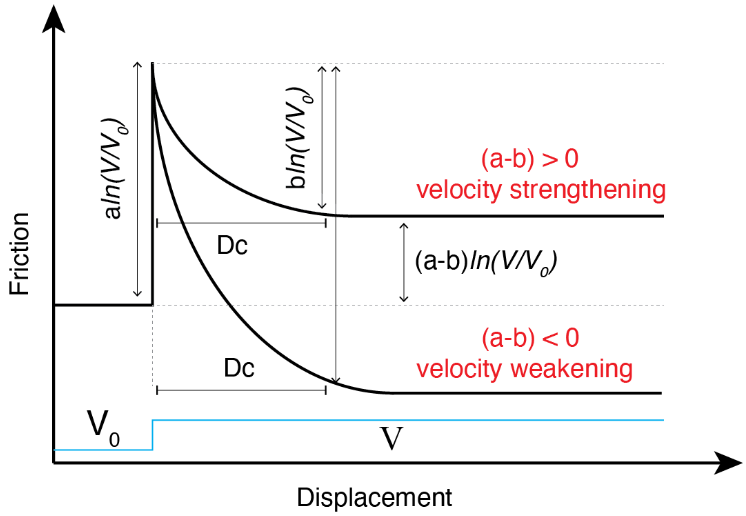

Figure 3.3: A schematic diagram illustrating the main features of rate-and-state friction in laboratory experiments.

In above full rate-and-state friction law, the μ is the function of sliding velocity V and state variable θ. μ_0 is the friction when the velocity is V_0. The introduction of the state variable θ allows transient behavior observed in non-steady-state experiments and healing in hold-and-slip experiments, thus, the friction coefficient is rate- and state-dependent (Avouac, 2015). The D_c is the characteristic slip distance, over which the friction coefficient μ evolves from the direct effect gradually to a new steady-state value (Figure 3.3). The slip distance D_c for laboratory samples is in the μm range, however, its values for natural faults are still an open question (Scholz, 2019; Fukuda et al., 2009).

As is shown in Figure 3.3, if $a-b<0$, indicating velocity-weakening friction, could lead to dynamic instabilities. The situation $a-b<0$ provides a necessary but not a sufficient condition for instability (e.g., Ruina, 1983; Ben-Zion, 2001). On the other hand, when $a-b>0$, the material is said to be velocity strengthening, and will always be stable. When the seismic asperity is surrounded by this velocity-strengthening region, we expect afterslip to occur around the rupture in response to the sudden stress changes.

In Equation 3.28, steady-state friction occurs when $\theta = D_c/V$. The friction at steady-state velocity V is then:

$$\mu = \mu_0 + (a-b)\ln\frac{V}{V_0} \tag{3.29}$$

Steady state occurs when the derivative of the state variable with respect to time is zero ($d\theta/dt = 0$), meaning that the state variable θ does not change over time. As the slip distance increases to D_c, the friction coefficient gradually approaches a steady-state value. To achieve this steady-state condition, constant normal stress and slip velocity must be maintained (Avouac, 2015), and the slip distance must be much greater than the characteristic slip distance D_c (Ben-Zion, 2001). Based on the steady-state mechanism, we can derive this purely rate-dependent (state-independent) friction law, which is widely used for modeling stress-driven afterslip after earthquakes (Barbot et al., 2009):

$$V = 2V_0 \sinh \frac{\Delta\tau}{(a-b)\sigma} \tag{3.30}$$

In Chapter 5, we use Equation 3.30 to model the afterslip evolution 3 yeas after the 2017 Mw 7.3 Sarpol-e Zahab earthquake.

3.3.3.3 Full Afterslip

Here, we define the "full" afterslip as the fault slip when the coseismic stress changes fully released. In this case, we do not consider the relaxation (evolution) process of the afterslip. In Chapter 6, we utilize 4.5-year InSAR observations and FEM models to explore the full friction afterslip associated with the 2017 Mw 7.3 Sarpol-e Zahab earthquake. Below we give a brief derivation of the full afterslip.

Based on Coulomb friction law, the shear and normal stresses acting between the surfaces during sliding could be written as (Byerlee, 1978):

$$\tau = C + \mu \cdot \sigma \tag{3.31}$$

where τ is the shear stress resolved on the fault, C is the fault cohesion, μ is the effective friction coefficient and σ is the normal stress acting on the fault plane. We assume the fault is cohesionless and normal and shear stresses resolved onto it could be decomposed into a background stress (τ_{bg} and σ_{bg}) and a coseismic perturbation ($\Delta\tau$ and $\Delta\sigma$). Then we neglect the stress changes due to the afterslip and aftershocks, thus:

$$\tau_{bg} + \Delta\tau = (\mu_0 + \Delta\mu)(\sigma_{bg} + \Delta\sigma) \tag{3.32}$$

where μ_0 and $\Delta\mu$ are the base friction coefficient before earthquake and friction strengthening of the fault after being loaded by the earthquake, respectively. $\Delta\mu$ is expected as a small value which is only a few percent of the fault strength μ_0. We assume that the preseismic Coulomb stress resolved on the fault is negligible: $\tau_{bg} - \mu_0 \cdot \sigma_{bg} \approx 0$ compared to the coseismic stress change, then we get:

$$\Delta\tau = \mu_0 \cdot \Delta\sigma + \Delta\mu \cdot (\sigma_{bg} + \Delta\sigma) \tag{3.33}$$

For strike-slip events, the coseismic normal stress change $\Delta\sigma$ usually could be ignored (e.g., Barbot et al., 2009; L. Wang, 2018); for thrust faulting like this 2017 Sarpol-e Zahab earthquake, we chose to keep this item in our simulations in Chapter 6. For simplicity, we specify the normal stress σ_{bg} as the overburden stress (lithostatic load) and then is resolved on the frictional fault. Thus we can get the relationship between coseismic shear and normal stress perturbations ($\Delta\tau$ and $\Delta\sigma$) and friction strengthening ($\Delta\mu$) within the afterslip zone is given by:

$$\Delta\tau = \mu_0 \cdot \Delta\sigma + \Delta\mu \cdot (\rho g h \cos\theta + \Delta\sigma) \tag{3.34}$$

where ρ is the density of the material, g is the gravitational acceleration (9.80665 m/s^2), h is the fault depth and θ is the fault dip angle.

3.4 Finite Element Method Modeling

In this thesis, PyLith software (Version 2.2.1) is also used for modeling the co- and post-seismic deformation (Aagaard et al., 2013). PyLith is an open-source finite element software for simulation of crustal deformation across spatial scales ranging from meters to hundreds of kilometers and temporal scales ranging from milliseconds to thousands of years. Its primary applications are quasi-static and dynamic modeling of earthquake faulting.

PyLith supports 2D and 3D static, quasi-static (neglecting inertia), and dynamic (including inertia) formulations of the governing equations, which can be isotropic elastic, linear Maxwell viscoelastic, generalized Maxwell viscoelastic, power-law viscoelastic, and Drucker-Prager elastoplastic. A variety of elastic and viscoelastic bulk rheologies are supported. Boundary conditions include Dirichlet (prescribed displacements and velocities), Neumann (traction), point forces, and absorbing boundaries. Cohesive elements are used to implement slip across interior surfaces (faults) with both kinematically-specified fault slip and slip governed by fault constitutive models. PyLith also includes an interface for computing static Green's functions for fault slip.

Here, we present several examples using the PyLith software. All simulations are based on a 3D mesh with spatial extents of $[-3, 3]$ km in both the x and y directions, and $[-4, 0]$ km in the z direction.

The first example is an elastic, static problem with Dirichlet boundary conditions and prescribed kinematic fault slip. The Dirichlet (displacement) boundary conditions (roller boundary condition) specify zero displacement in both the x and y directions on the negative and positive x-faces, and zero displacement in the z direction on the negative z-face. The model includes a vertical fault with a combination of left-lateral and reverse slip. The left-lateral component of slip is constant at 2 m within the upper crust and decreases linearly to zero at the base of the model. The reverse slip component is 0.25 m at the surface and linearly decreases to zero at a depth of 2 km. Figure 3.4 shows the simulated displacement field within the 3D domain.

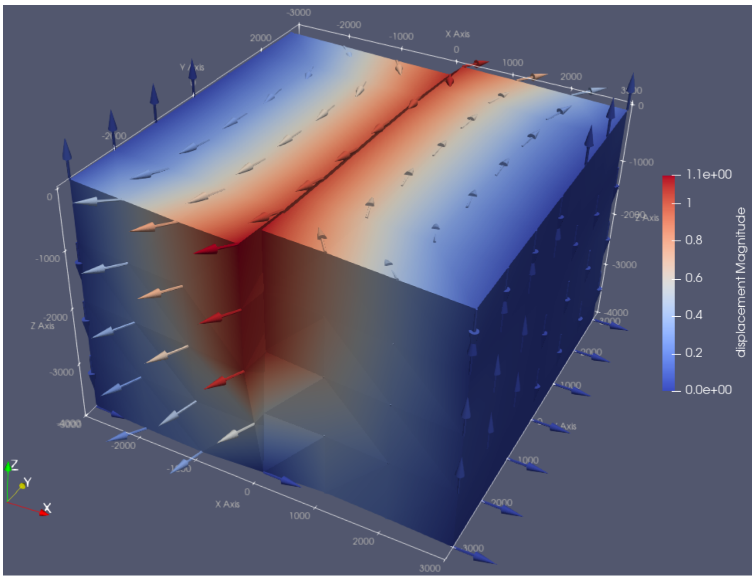

Figure 3.4: Displacement magnitude based on first example using PyLith software.

Another example demonstrates static fault friction. This simulation is also based on an elastic medium. We apply axial (x-direction) displacements on both the positive and negative x-faces to maintain a compressive normal traction on the fault surface; otherwise, no frictional resistance would occur. The prescribed displacements are 1 m in the x-direction and 3 m in the y-direction (Dirichlet displacement boundary conditions). These displacements are large enough to overcome the fault friction, leading to slip. We set the static coefficient of friction on the fault to 0.6 and the cohesion to 0 Pa. Figure 3.5 illustrates the resulting fault slip distribution from the simulation.

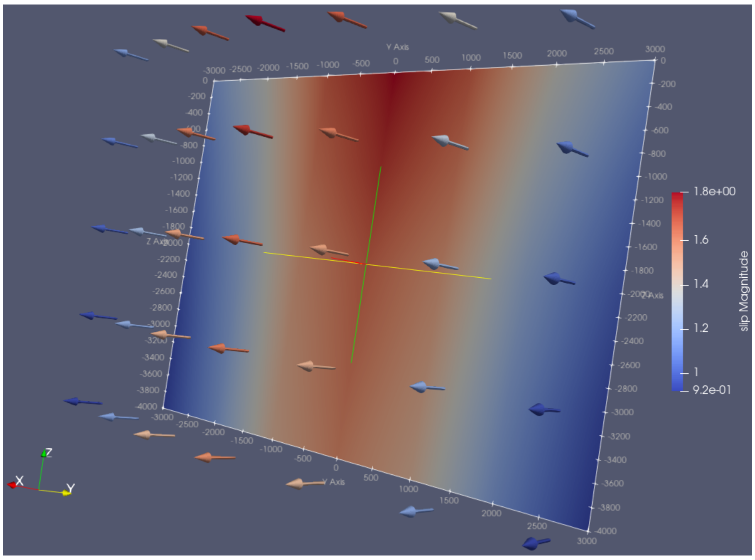

Figure 3.5: Fault slip magnitude based on second example using PyLith software.

In this thesis, we construct 2D finite element models to simulate both co- and post-seismic deformation. Dirichlet boundary conditions are applied by fixing the displacements normal to the model boundaries, with prescribed zero values.

We compute the static Green's functions on the fault plane and use optimization techniques based on InSAR-derived coseismic deformation fields to infer the coseismic slip distribution. From the obtained slip distribution, we derive the corresponding stress changes on the fault plane, which enables further investigation of stress-driven fault afterslip. A full afterslip model is employed to simulate the frictional properties on the fault surface.

We primarily use an elastic medium to model the co- and post-seismic deformation, while the Maxwell viscoelastic contribution to the post-seismic response is also incorporated by considering a viscoelastic body. Further details can be found in Chapter 6.

4 Background of the 2017 Mw 7.3 Sarpol-e Zahab Earthquake

4.1 Introduction

On 12 November 2017, an earthquake with a magnitude of Mw 7.3 and focal depth of approximately 21 km struck about 50 km north of Sarpol-e Zahab city, in Kermanshah Province in western Iran, which is also very close to the Iran and Iraq border (Figure 4.1). Because this event is the largest one in this region since instrumental records began recording, it is very important for us to study this event to have a better understanding of the earthquake mechanisms and further seismic hazard evaluation.

In the following chapters of this thesis, we take the 2017 Mw 7.3 Sarpol-e Zahab earthquake as an example to analyze the co- and post-seismic models. In this chapter, we firstly introduce the tectonic background of the earthquake, then we summarize the current research status based on previous studies. We extend earlier studies in the next two chapters which will walk through the details of our co- and post-seismic deformation modeling using analytical and numerical solutions.

4.2 Tectonic Background

The ongoing collision between the Eurasian and Arabian plates has led to the formation of one of the most tectonically and seismically active intracontinental orogens: the northwest-southeast striking Zagros Mountains in southwestern Iran. The convergence velocity between the Eurasian and Arabian plates is ∼2-3 cm/yr, almost half of which is accommodated by the Zagros mountain belt (Figure 4.1, Khorrami et al. 2019; Vernant et al. 2004). In northwestern Zagros, the deformation rate is partitioned as ∼5 mm/yr dextral strike-slip motion along northwest-southeast trending faults, and ∼4 mm/yr shortening perpendicular to the mountain belt, while in southeastern Zagros, the deformation is ∼9 mm/yr pure shortening perpendicular to the belt (Walpersdorf et al., 2006).

Contemporary active deformation around the ZFTB is mainly derived from seismic and aseismic deformation triggered by thrust and strike-slip faulting (e.g., Barnhart and Lohman, 2013; Copley et al., 2015; Motagh et al., 2015), folding and uplift of sedimentary cover (e.g., Berberian, 1995), and ductile thickening of the basement (Allen et al., 2013). The Phanerozoic sedimentary cover rock reaches a thickness of ∼8–13 km, overlying the Phanerozoic crystalline basement. Much work has been done to explore thin and thick-skinned shortening related to the Phanerozoic sedimentary succession and deep basement faulting in the Zagros belt (e.g., Falcon, 1969; Molinaro et al., 2005; Mouthereau et al., 2012; Talebian and Jackson, 2004). Moderate magnitude earthquakes (∼M 5–6) have been widely distributed in the ZFTB, but the characterization and contribution of such seismicity to cover basement interaction are still not fully understood (e.g., Copley et al., 2015; Motagh et al., 2015; Nissen et al., 2011; Talebian and Jackson, 2004). A Hormuz salt unit in Fars Arc and shales in the Lurestan Arc due to the strong mechanical contrast between sedimentary cover and basement are suspected as a decoupling layer at the cover basement interface (e.g., Alavi, 2007; McQuarrie, 2004), which may impede propagation of fault ruptures to the surface in this region. Under such a geological and tectonic environment, many blind thrust faults that cut through the sedimentary cover, grow in the ZFTB and contribute to the current topography of the Zagros. Thus, inferring the geometry of these blind faults becomes challenging. The major faults within the ZFTB consist of the Main Recent Fault, the Mountain Front Fault (MFF), the High Zagros Fault (HZF), and the Zagros Foredeep Fault (ZFF) (Figure 4.1b, Berberian 1995).

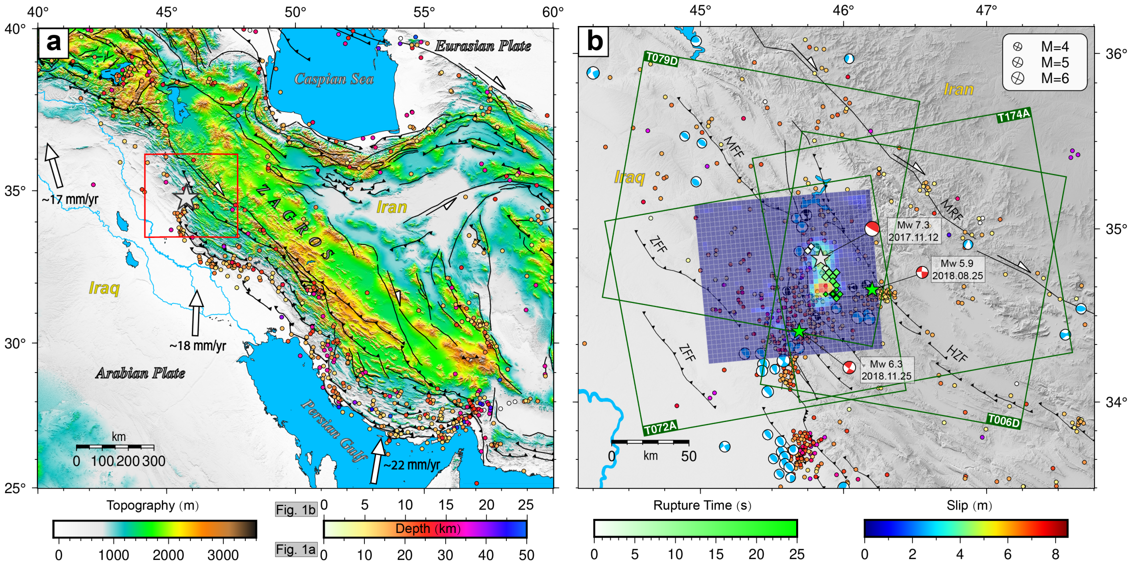

Figure 4.1: Tectonic background of the 2017 Sarpol-e Zahab earthquake. (a) The colored dots are earthquakes (from 1976 to 2021) from the Global Centroid Moment Tensor (GCMT) catalog (https://www.globalcmt.org). The red box indicates the area of figure b. (b) Detailed tectonic map of the seismogenic area. The blue beach balls are from the GCMT catalog. Colored dots are earthquakes (from 2006 to 2021 with M > 3.5) from the Iranian Seismological Center (IRSC, http://irsc.ut.ac.ir). Dark green boxes indicating the spatial extent of Sentinel-1 imagery and the coseismic slip distribution are from Guo et al. (2022). Black beach balls are from Nissen et al. (2019). Red beach balls are the focal mechanisms of the 2017 Sarpol-e Zahab mainshock and two ~M 6 aftershocks. The green rhombuses represent the rupture time of the mainshock, which is mapped from Nissen et al. (2019).

The destructive 2017 Mw 7.3 Sarpol-e Zahab event occurred along a shallowly east-dipping ($\sim 15°$) reverse fault with dextral components in the Lurestan Arc of the ZFTB. Several ~M 6 earthquakes in the sedimentary cover followed the mainshock, such as the 25 August 2018 Mw 5.9 event, and 25 November 2018 Mw 6.3 event (Figure 4.1b). However, these two large aftershocks along steeply dipping dextral strike-slip faults may reveal strain partitioning in the northwestern Zagros belt as the overall convergence direction between the Eurasian and Arabian plates changes from orthogonal shortening in south-eastern Zagros to oblique shortening in northwestern Zagros (e.g., Talebian and Jackson, 2004). The 2017 Sarpol-e Zahab mainshock is located in a crystalline basement, where the seismicity interactions between sedimentary cover and basal basement due to the possible existence of the weak Hormuz shale as a decoupled layer is still an open question (e.g., Barnhart et al., 2018; Nissen et al., 2011; Wang and Bürgmann, 2020).

4.3 Current State of Research

Several studies have been performed to better understand the seismic and aseismic slip of the 2017 Sarpol-e Zahab earthquake using geodetic observations, but some debate still remains, for example, the number of coseismic slip asperities (e.g., Feng et al., 2018; Nissen et al., 2019; Vajedian et al., 2018; Yang et al., 2018), the existence of downdip afterslip (e.g., Liu and Xu, 2019; Wang and Bürgmann, 2020) and the postseismic contribution from viscoelastic relaxation (e.g., Barnhart et al., 2018; Lv et al., 2020; Wang and Bürgmann, 2020). Additionally, previous studies also have used different fault geometries to explore the fault-slip models. They use either a planar (e.g., Feng et al., 2018; Yang et al., 2018; Liu and Xu, 2019; Nissen et al., 2019) or a ramp-flat fault, in which the mainshock ruptured the "ramp" part, whereas the afterslip is explained by the "flat" part (e.g., Barnhart et al., 2018; Wang and Bürgmann, 2020; Fathian et al., 2021).

Geologically, the mainshock with a centroid depth of ~16 km ruptured the "ramp" which is located within the underlying Precambrian crystalline basement (e.g., Barnhart et al., 2018). The cover–basement interface which is regarded as a low-friction "flat" is, therefore, inferred as the primary location where the afterslip of this 2017 Mw 7.3 event occurred (e.g., Barnhart et al., 2018; Wang and Bürgmann, 2020; Fathian et al., 2021). However, geologic-constrained studies and many published structural cross-sections through the northwest Zagros suggest that the 2017 Mw 7.3 event may be related to a more complicated fault structure. This structure includes basement splay faults within the northwest ZFTB that have penetrated and offset the overlying structures of the sedimentary cover. Given the structural complexity in the foreland of mountain range, the 2017 Mw 7.3 Sarpol-e Zahab earthquake presents a valuable opportunity to explore the seismogenic faults in the northwest Zagros. This not only plays a significant role in modulating the seismic cycle and evaluating regional seismic hazards but also enhances our understanding of the relationship between the basement-involved faulting and thick- and thinskinned shortening in the northwest Zagros.

In next two chapters, we extend earlier studies and investigate both co- and post-seismic models of the 2017 Mw 7.3 Sarpol-e Zahab event with InSAR data. In Chapter 5, we use InSAR observations to investigate the fault geometry and afterslip evolution within 3 years after a mainshock based on analytical solutions. As a follow-up research of Chapter 5, we dive into more details utilizing ~4.5-year InSAR data and 2D FEM models incorporating various fault geometries such as planar faults, ramp-flat faults, and the combined models of ramp-flat and splay faults to explore frictional afterslip process due to coseismic stress changes following the mainshock in Chapter 6.

5 Analytical Models for Co- and Post-Seismic Deformation

5.1 Introduction

In this chapter[1], we use InSAR observation to investigate the fault geometry and afterslip evolution within 3 years after the 2017 Mw 7.3 Sarpol-e Zahab earthquake. Coseismic and postseismic slip models are analyzed using analytical models. The main structure of this chapter is as follows:

- In Section 5.2, we introduce our InSAR data processing strategy to get the coseismic and postseismic deformation fields, the time span of the postseismic time series are ∼3 years.
- Section 5.3 explains coseismic modeling strategy. We analyze the optimal coseismic fault model from planar and a range of listric faults with coseismic interferograms. Coseismic resolution tests are also conducted to evaluate how sensitive the InSAR observations are to the slip asperities.
- In Section 5.4, we explore the fault geometry and transient aseismic slip evolution for the first 4, 7, 10, 12, 24, and 36 months after the mainshock. We use kinematic, stress-driven afterslip models, as well as the combination models of afterslip and viscoelastic response to explain the postseismic data. The deep afterslip downdip of the coseismic rupture from the perspective of data accuracy and model resolution are analysed.
- In Section 5.5, we compare the existing postseismic models and discuss the complexity of fault friction, the reactivation of the MFF system and/or shallower multiple detachments that were most likely triggered by the mainshock, given our inversion results and the structural geology background of the Zagros.
- Section 5.6 is a brief conclusion of this chapter.

[1] This chapter expands upon the paper published by the candidate from the publication Guo et al. (2022). Co-authors of this publication are acknowledged.

5.2 InSAR Observations

5.2.1 Coseismic Deformation

Four tracks of Sentinel-1 SLC data cover the seismogenic zone of the 2017 event. The SLC data from two ascending tracks (T072A and T174A) and two descending tracks (T006D and T079D) are processed with GAMMA software (Wegnüller et al., 2016). The topography effect is removed by a 30-m (1 arc sec) DEM from the Shuttle Radar Topography Mission (SRTM, Farr et al. 2007). A 10 by 2 multilook factor for range and azimuth directions are performed to improve the signal to noise ratio. Generic Atmospheric Correction Online Service (GACOS) for InSAR products (Yu et al., 2018) are used to reduce atmospheric delay error from differential interferograms (Figure 5.1). The full Variance-Covariance Matrix (VCM), constructed using a 1D exponential covariance function with far-field nondeforming area in coseismic interferograms (Feng et al., 2013), indicates that the far-field noise is less than 1 cm after atmospheric delay correction with GACOS.

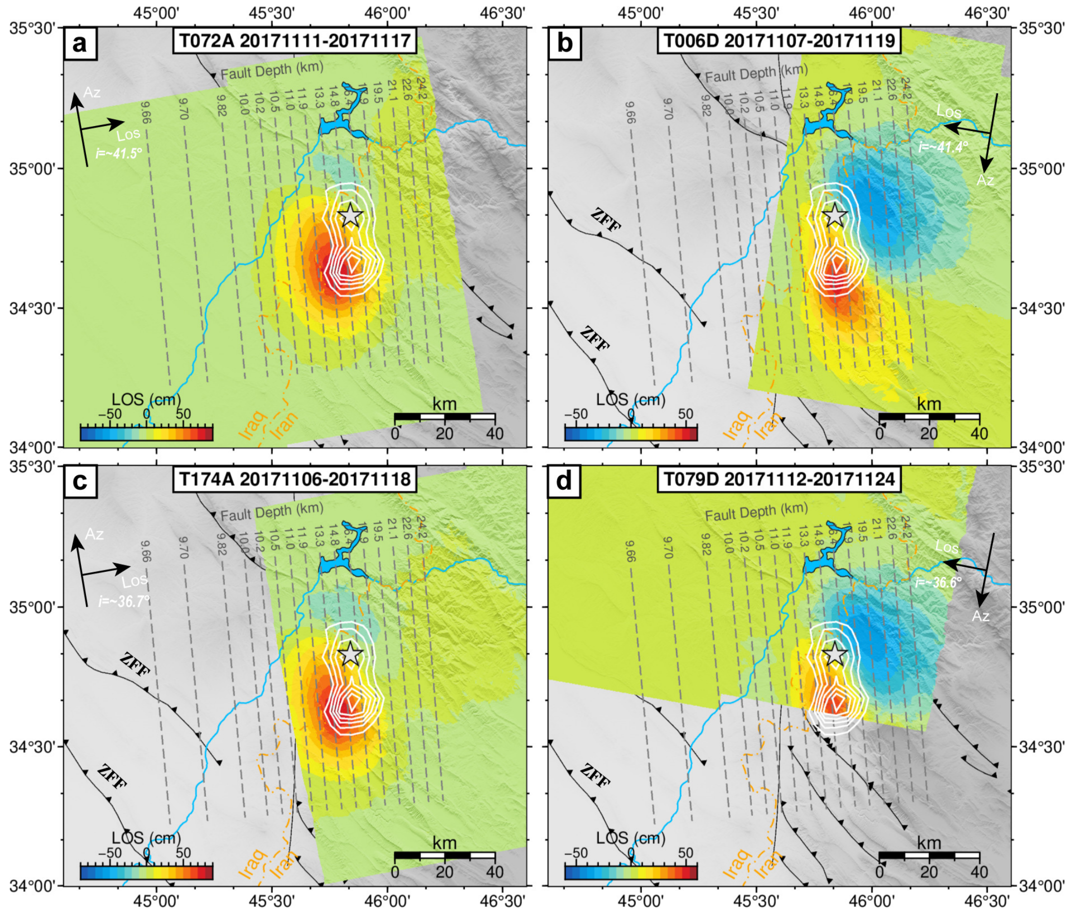

Figure 5.1: Coseismic interferograms from (a) T072A, (b) T006D, (c) T174A and (d) T079D of the 2017 Sarpol-e Zahab earthquake. Gray dashed lines represent the fault depth of the ramp-flat model. White contours and gray star represent our preferred coseismic slip model at 1-m intervals and the epicenter of the Mw 7.3 mainshock, respectively.

Coseismic interferograms from ascending data T072A and T174A suggest that the maximum and minimum LOS displacements are approximately 85 and -21 cm, respectively (surface motion toward the satellite is positive, Figure 5.1). For the descending data T006D and T079D, the maximum and minimum LOS displacements are approximately 50 and -39 cm, respectively (Figure 5.1). The difference in the sense of range measurements between the ascending and descending tracks indicates a significant contribution from east-west coseismic deformation. The coseismic interferograms also contain information from early postseismic deformation because of the 12-day revisit time of the Sentinel-1 satellite.

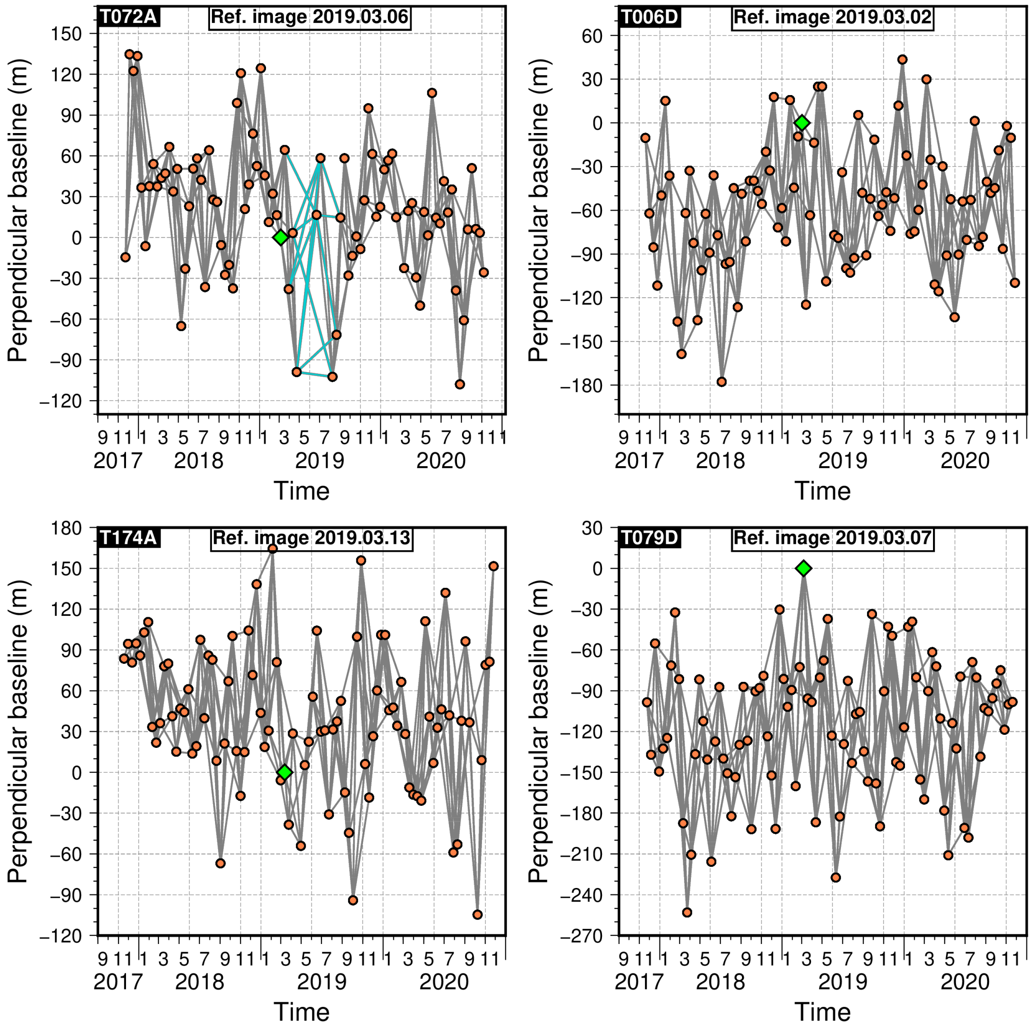

Figure 5.2: The 3-year baseline networks for the 4 sentinel-1 tracks. The green diamond represents the reference image. For T072A, we re-selected 13 interferogram pairs (cyan lines) with 9 SLC data between 18 March 2019 and 02 September 2019 to form at least 3 interferogram pairs for every single SLC data.

5.2.2 Postseismic Deformation

5.2.2.1 Time Series Analysis 3 Years after Mainshock

To analyze postseismic deformation, we perform multitemporal interferometry analysis in four tracks of Sentinel-1 data based on the SBAS technique (Berardino et al., 2002). We

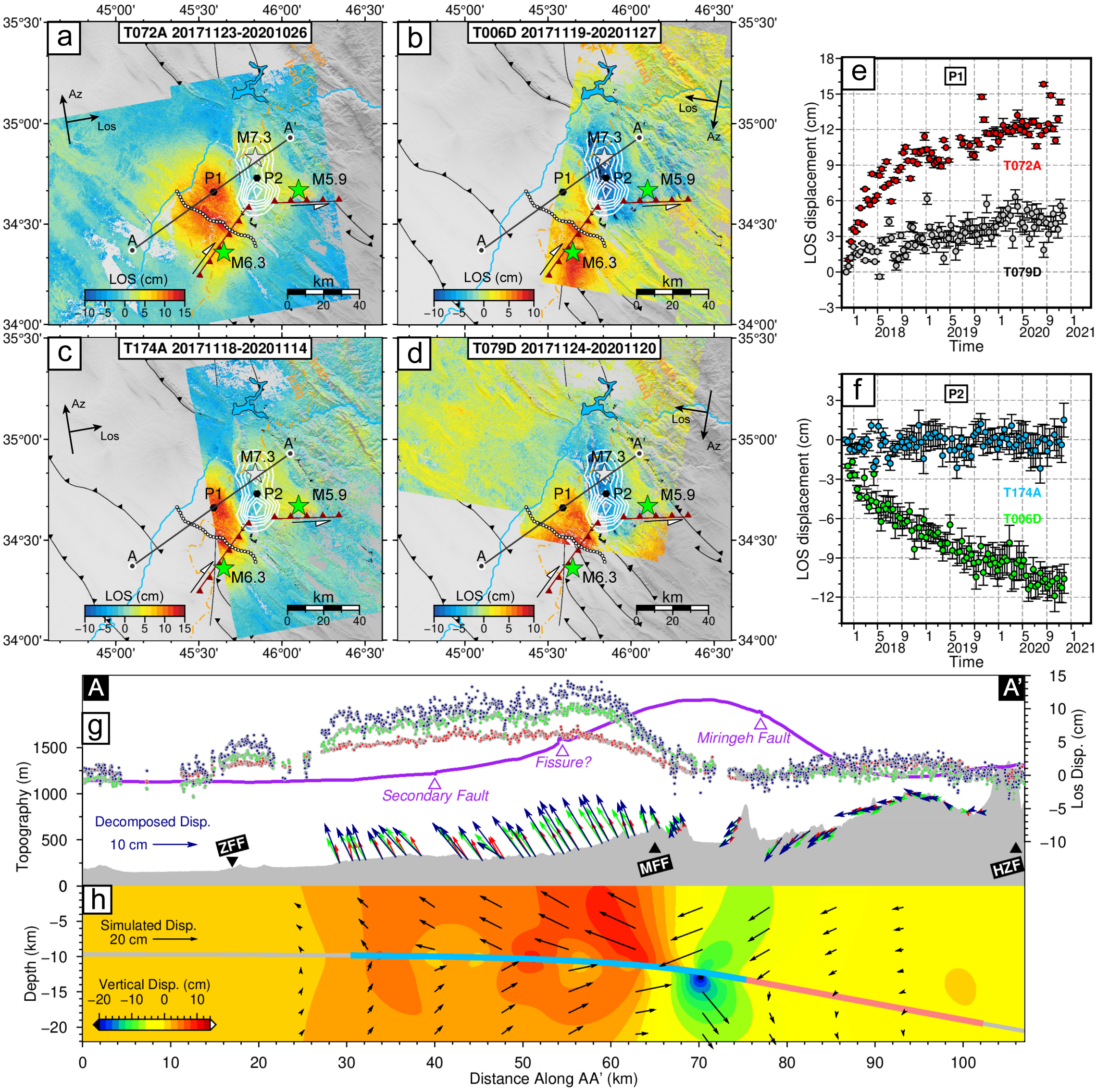

Figure 5.3: Postseismic InSAR observations. (a-d) represent the ∼3-year cumulative postseismic LOS displacements of T072A, T006D, T174A and T079D, respectively. White contours and gray star represent our preferred coseismic slip model at 1-m intervals and the epicenter of the Mw 7.3 mainshock, separately. Green stars and dark red faults represent the locations of the two bigger aftershocks and the corresponding fault traces from Fathian et al. (2021). White dots (black outline) are the surface trace of the secondary fault indicated by the coseismic interferogram discontinuity and field survey (Vajedian et al., 2018). Profile AA' which is nearly orthogonal to the geological structures corresponds to the surface observations and simulations of Figure 5.16. (e-f) are the LOS displacement time series of P1 and P2, respectively, the error bars are the standard deviations from pixels within a radius of 30 meters. (g) shows the contribution of postseismic deformation to topography along profile AA'. The red, green and dark blue dots represent the postseismic LOS displacements of 4 months, 1 year and 3 years after the mainshock, respectively. The purple line indicates the coseismic LOS displacements which are scaled by a factor of 5. The red, green and dark blue vectors are the 2.5-dimension deformation (quasi-eastward and quasi-upward) of 4 months, 1 year and 3 years after the mainshock, separately, which are decomposed from ascending track T072A and descending track T079D. (h) shows the 3-dimension displacements in depths along profile AA', which is simulated from the 3-year kinematic afterslip model. The gray line indicated a ramp-flat fault, the light red and light blue lines show the approximate scopes of coseismic rupture and postseismic afterslip, respectively.

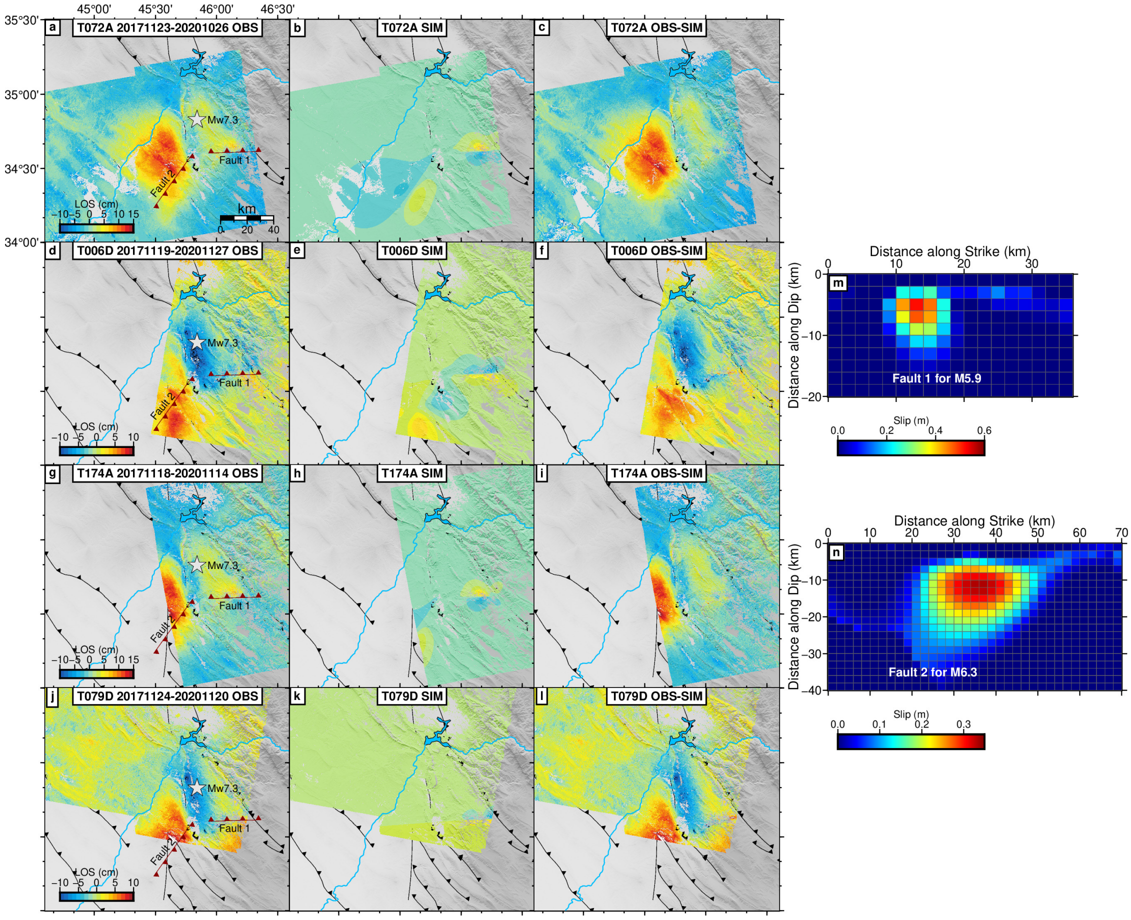

Figure 5.4: 3-year postseismic deformation of 2017 Sarpol-e Zahab earthquake for T072A, T006D, T174A and T079D (a, d, g, j); the simulated surface displacements of the Mw 5.9 and Mw 6.3 earthquake for T072A, T006D, T174A and T079D (b, e, h, k), which are from the fault models (m-n) proposed by Fathian et al. (2021); (c, f, i, l) are the cleaner results after the reducing of the simulations (b, e, h, k) from original observations (a, d, g, j). The gray star is the epicenter of the mainshock. The red faults (Fault 1 and Fault 2) are surface traces of fault models from Fathian et al. (2021).

construct a network of high-coherence small baseline interferograms covering 3 years after the 2017 Sarpol-e Zahab earthquake. The thresholds of 200 m and 50 days are selected for the spatial and temporal baselines. The SBAS method of StaMPS software (Hooper et al., 2004) is used for time series analysis after differential interferometric processing with GAMMA. The measurement points are selected using a coherence threshold of 0.3. After correcting for the atmospheric delay using GACOS products and the DEM errors, we finally obtain the InSAR time series and cumulative LOS displacements for 3 years following the 2017 event. As shown in Figure 5.3e-f, the 3-year cumulative range changes at P1 and P2 are approximately 15 cm and -12 cm for ascending track 072A and descending track 006D, respectively.

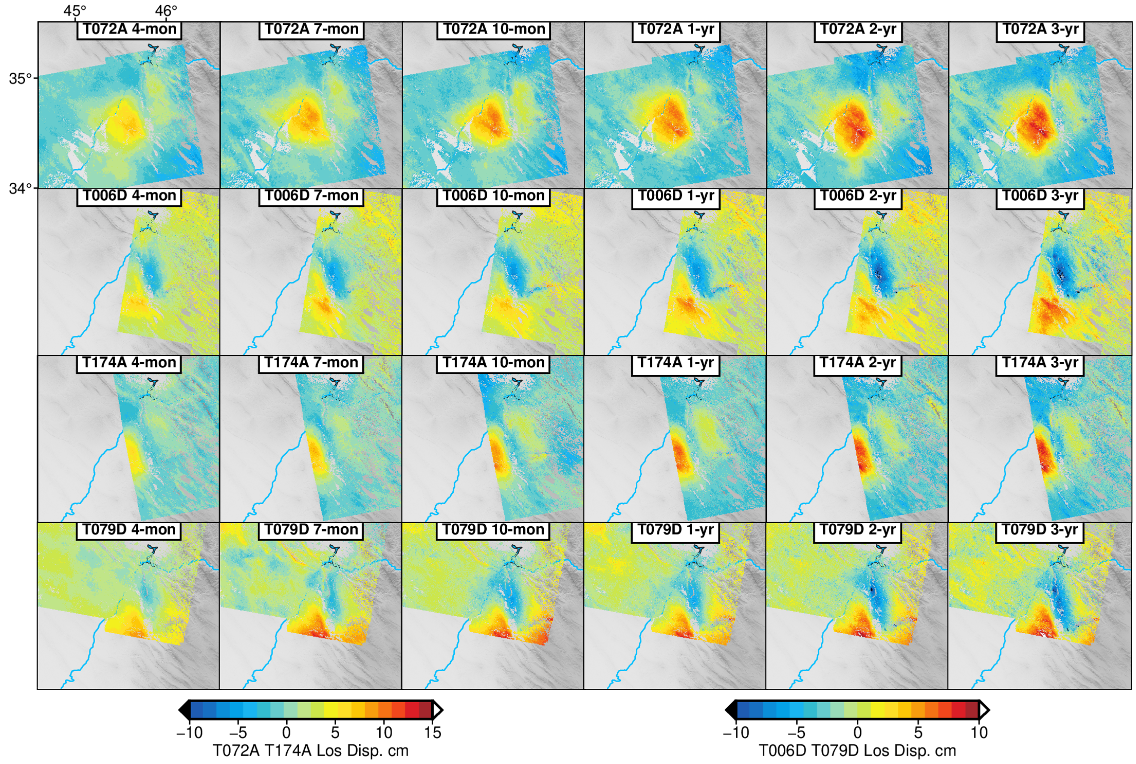

Figure 5.5: InSAR time series of T072A, T006D, T174A and T079D after reducing the coseismic deformation of the 25 August 2018 Mw 5.9 and 25 November 2018 Mw 6.3 earthquake. Please note the different color bars of ascending and descending tracks.

5.2.2.2 The Impact of Aftershocks on Postseismic Deformation

Note that in Figures 5.3a-d, there is some localized signal contamination due to the coseismic and postseismic deformation of the two large aftershocks: the Mw 5.9 earthquake on 25 August 2018 and the Mw 6.3 earthquake on 25 November 2018 (Figure 5.3a-d). Here, the fault models of these two aftershocks proposed by Fathian et al. (2021) (Figure 5.3a-d and Figure 5.4) are used for forward modeling to get the resulted surface displacements, and then we take the difference between our original InSAR time series and the simulations to obtain a cleaner postseismic time series (Figure 5.4 and 5.5). In the following sections, the coseismic deformation of the two aftershocks is reduced from all of the time series influenced by these two large events (Figure 5.5) and is then employed for further analysis and inversions.

5.3 Coseismic Fault Models

5.3.1 Coseismic Deformation Inversion

The four coseismic interferograms are downsampled with a quadtree sampling approach (Jónsson et al., 2002; Figure 5.6) to reduce the computation, and then the nonlinear global search is performed for the fault parameters. The Multipeak Particle Swarm Optimization (MPSO) approach, which is based on a hybrid minimization algorithm (e.g., Feng et al., 2013, 2017), is used for nonlinear global optimization. The causative fault of the 2017

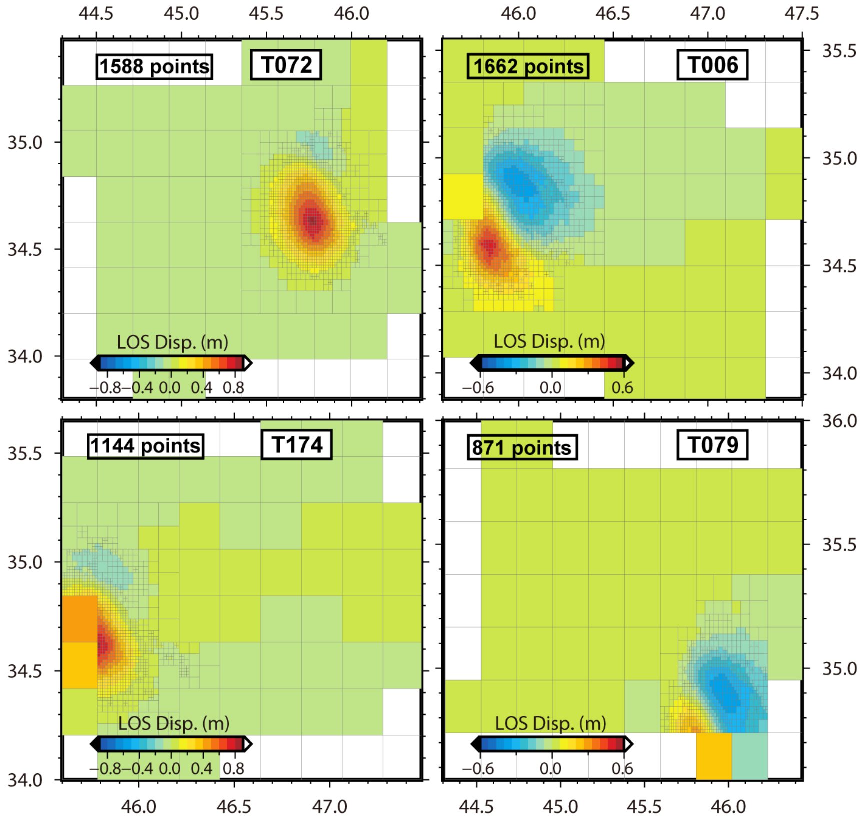

Figure 5.6: The downsampled points from 4-track coseismic interferograms with quadtree sampling approach (Jónsson et al., 2002), totally 5265 points.

Sarpol-e Zahab earthquake is modeled as a single rectangular dislocation with uniform slip in a homogeneous, elastic half-space assuming a shear modulus of 33 GPa and a Poisson ratio of 0.25. The preferred fault model is a blind, almost north-south trending (a strike of 354.7°), east-dipping (a dip of 17.17°) fault with a rake of 143.74°. The mainshock mainly ruptured a 40 km long and 18 km wide fault with a uniform slip about 3.7 m, the centroid depth from our nonlinear inversion is about 16 km, indicating the mainshock ruptured a basement-involved fault. The uncertainties of these model parameters are evaluated by a Monte Carlo bootstrap simulation technique with 100 simulations perturbed with observation noises based on VCM. Our preferred fault geometry is consistent with the uniform models proposed by previous studies (e.g., Feng et al., 2018; Barnhart et al., 2018; Wang and Bürgmann, 2020).

After that, we carry out linear inversions for the distributed slip on the fault plane (e.g., Xu et al., 2019). The fault geometry derived from nonlinear inversion was fixed and we extended along-strike fault length and along-downdip fault width to 100 km, before the fault plane is discretized to fault patches with 3 km by 3 km. We find that the fault model with a dip angle of 15° fits the coseismic displacements best from a variety of planar faults.

Fathian et al. (2021) proposed a listric fault to model coseismic deformation based on the relocated aftershocks while other studies used a simply planar fault only (e.g., Feng et al., 2018; Barnhart et al., 2018; Wang and Bürgmann, 2020). Here, different from Fathian et al. (2021), we attempt to search for a listric fault model from the perspective of coseismic data fitting. We fix the upper fault depth at 13.4 km, which is derived from our nonlinear inversion and then test a range of dip angles from 13° to 25° (hereafter called the initial dip) at this depth. We construct the following equation to constrain the fault:

$$\mathrm{dip}_n = \begin{cases} a \cdot (13.4 - n) + \mathrm{dip}_{n+1}, & n < 13.4, \\ b, & n = 13.4,\ b \in [13, 25] \\ -a \cdot (n - 13.4) + \mathrm{dip}_{n-1}, & n > 13.4, \end{cases} \tag{5.1}$$

where n is depth (km) of fault patch; dip_n represents the dip angle of fault patch at the depth of n km; a controls the curvature of the fault model ($a \in [0 : 0.2 : 8]$), b is the initial dip of the nonlinear-inversion upper fault boundary where the depth is 13.4 km. Here we test a range of initial dips for b from 13-25° with 1° intervals. A particular case is that the fault would be planar and the dip angle would be b if $a = 0$. The same smoothing factor and rake constraints with abovementioned planar fault are imposed in the inversions. Our results show that, however, the best-fitting fault model is still a single planar fault dipping 15°, which can explain the InSAR observations well enough (Figure 5.7a). The misfit of the listric fault with $a = 4$, $b = 22°$ is not significantly worse than that of the planar fault dipping 15° (Figure 5.7a and 5.7c) because the fault geometries produced coseismic rupture are very similar. Even though the coseismic slip favors a planar fault model, the postseismic slip along listric fault may also be triggered in case of the Mountain Front Fault (MFF) system is reactivated (see Section 5.5).

The coseismic slip model reveals a unilaterally southward rupture for the mainshock involving the sequential rupture of two asperities, along a dextral-thrust fault (Figure 5.7b). The main coseismic slip area is concentrated at a depth range of ~13-19 km with maximum slip exceeding 7 m. The geodetic moment is estimated to be 1.0×10^{20} Nm, corresponding to a moment magnitude of Mw 7.3. The surface deformation predicted by the coseismic model is in good agreement with the observations (Figure 5.8). Our coseismic model confirms two asperities (Figure 5.7b), which is similar to the InSAR-derived results of some previous studies (e.g., Barnhart et al., 2018; Feng et al., 2018), while others proposed only one simple asperity (e.g., Wang and Bürgmann, 2020). It is worth noting that a finite fault model from seismic waveforms and backprojection results also favor two apparent parts which produce separate peak slips and energy release (Nissen et al., 2019).

5.3.2 Coseismic Checkerboard Tests

To evaluate how sensitive the InSAR observations are to the slip asperities, we also conduct the resolution tests with both coarse (with asperities of $\sim 24 \times 24$ km, Figure 5.9a-d) and fine (with asperities of 15×15 km, Figure 5.9e-h) checkerboard patterns of unit slip in which strike (dextral) slip is 0.6 m and dip (thrust) slip is 0.8 m. Forward calculations are carried out firstly to simulate the surface deformation at every downsampled points of coseismic interferograms (Figure 5.6) and the Gaussian noises which are based on the standard deviations of far-field noises are added to the synthetic surface observations. Under the same parameterizations as above inversions, we invert the slip distribution and to see how well the input models are recovered. Despite the diminishing resolution and increased smearing with depth, as is shown in Figure 5.9, the coseismic slip asperities and both the strike- and dip-slip components at the depth range of 10-20 km can be overall recovered by both coarse and fine checkerboard slip pattern with the recovery of more than 70%, which is defined as recovery $= \left(1 - \frac{\sum_{i=1}^{n} |S_i - S'i|}{\sum_{i=1}^{n} |S_i|}\right) \times 100\%$, where S_i and S_i' represent the input slip and inverted slip of i_{th} patch, respectively, and the n is the number of

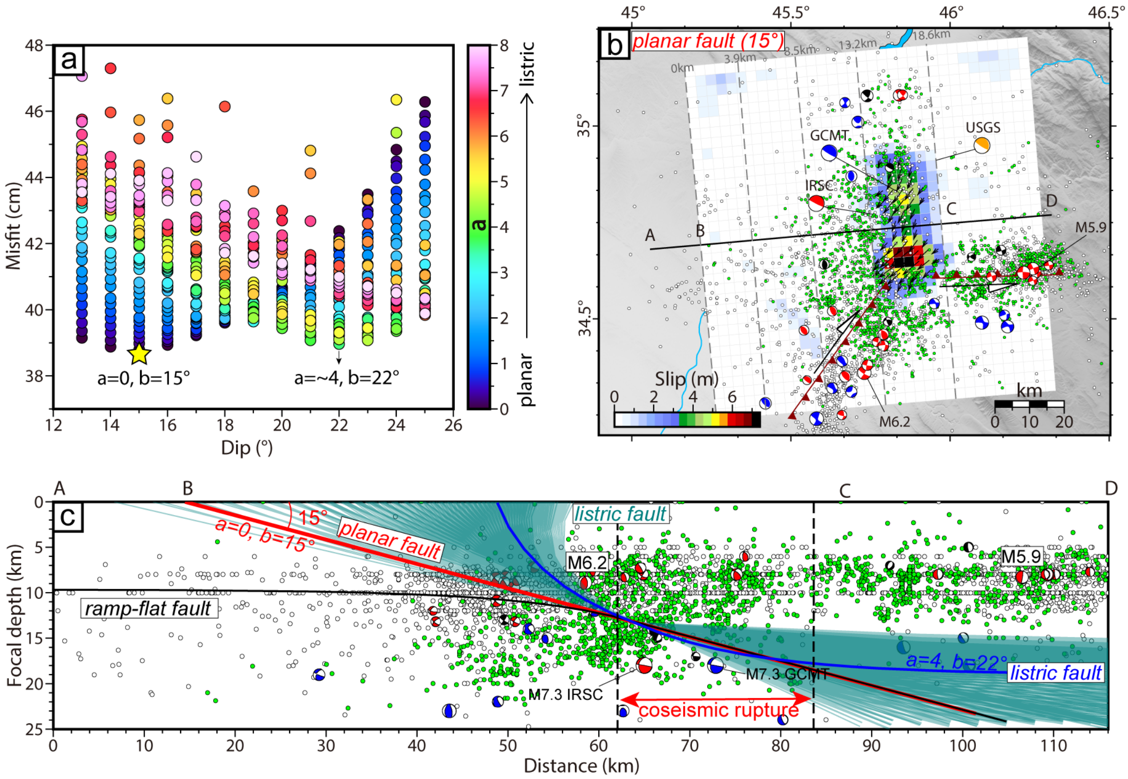

Figure 5.7: Fault geometry searching results and slip distribution. (a) The searched fault models with Equation 5.1. The optimal fault (yellow star) is a planar fault with dipping 15°. (b) Slip distribution with the planar fault dipping 15°. The two dark red, strike-slip faults of M 5.9 and M 6.3 events are from Fathian et al. (2021). (c) is the seismicity projection of profile AD in (b) along depth. The green and white dots indicate the relocated aftershocks within about 2 months from Fathian et al. (2021) and aftershocks within about 3 years from Iranian Seismological Center (IRSC) catalogue, respectively. The red, blue and black beach balls are the focal mechanisms from IRSC, Global Centroid Moment Tensor (GCMT) and Nissen et al. (2019), respectively. The cyan lines indicate all of the tested listric fault models. The red, blue and black lines are the planar fault model dipping 15°, the listric fault model with $a = 4$, $b = 22°$ and the ramp-flat model proposed in Section 5.4, respectively.

patches with input slip. The comparison between coarse and fine slip patterns shows that the larger the slip asperity is, the better the models could be recovered.

Overall, the checkerboard tests reveal that the InSAR observations in this study have a good recovery of coseismic slip distribution (Figure 5.9), and thus, we attribute the difference in asperity numbers in previous studies to the difference in fault parameterization (e.g., fault location and depth), inversion configurations (e.g., smooth factor) and input data among previous studies.

5.4 Postseismic Fault Models

In this section, we explore the fault structure based on kinematic afterslip inversions and search for an optimal mechanical afterslip model that features varied frictional properties along the fault plane. Then, we explore the possibility of the combination of stress-driven

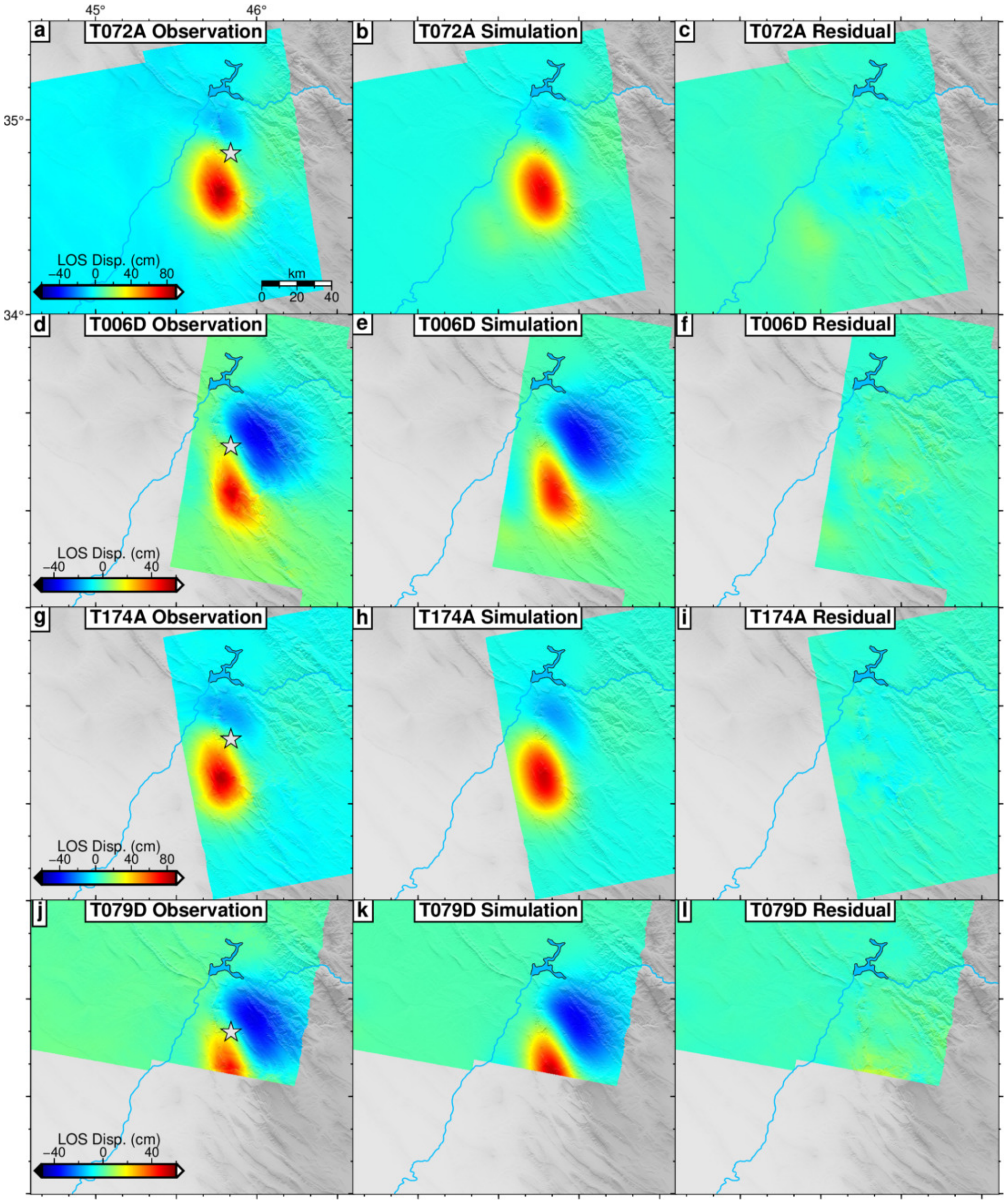

Figure 5.8: The observations (first column), simulations (second column) and residuals (third column) of T072A (a-c), T006D (d-f), T174A (g-i) and T079D (j-l) based on the coseismic model. The gray star is the epicenter of the mainshock.

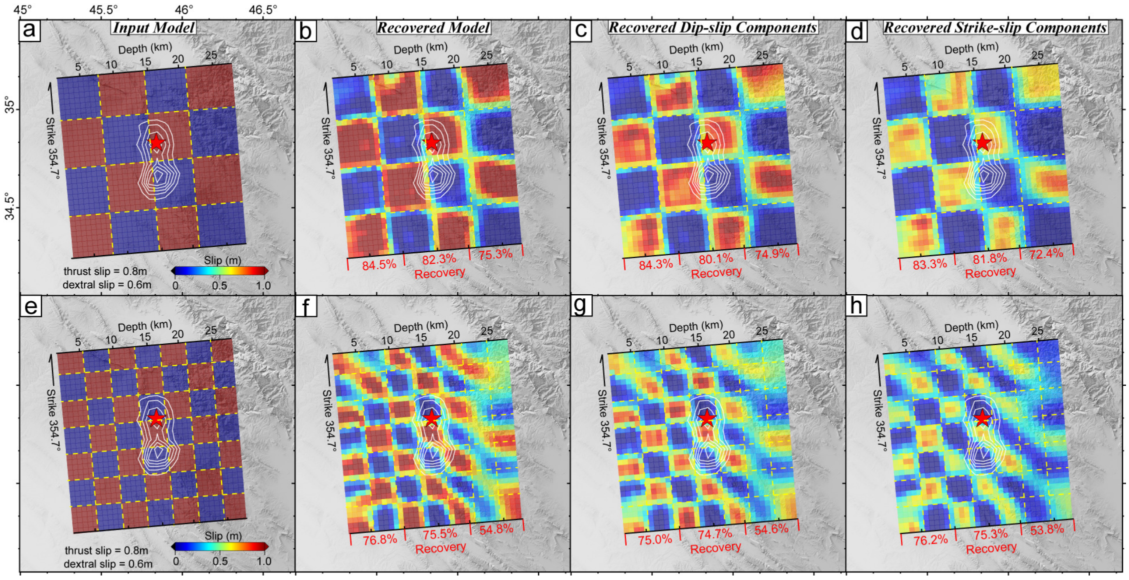

Figure 5.9: Checkerboard tests for the coseismic model resolution. Coarse (a) and fine (e) input models with 1-m slip are used for simulating synthetic surface displacements. The slip patterns (b and f), dip- (c and g) and strike-slip (d and h) components are recovered by the synthetic InSAR displacements.

afterslip and viscoelastic relaxation as a possible postseismic model. Finally, a detailed analysis of the downdip afterslip is conducted. Here, we do not take the poroelastic rebound into consideration because the predicted poroelastic contribution 1 year after the 2017 mainshock was lower than 5 mm, and the spatial pattern of the simulations was in contrast to the postseismic observations (Wang and Bürgmann, 2020).

5.4.1 Kinematic Afterslip Models

Previous studies have suggested that the postseismic deformation of the 2017 Sarpol-e Zahab event was mainly dominated by afterslip, while the viscoelastic and poroelastic contributions were negligible (Barnhart et al., 2018; Wang and Bürgmann, 2020). Under such assumptions, they indicated that the mainshock and afterslip activated a ramp-and-flat structure. Here, we perform more detailed searches than previous studies to derive the fault structures with postseismic deformation of 4, 7, 10, 12, 24, and 36 months after the mainshock (Figure 5.5). We downsample the InSAR postseismic observations uniformly around the main deformation area (Figure 5.10) and seek a time-invariant fault geometry that is able to satisfactorily match the InSAR observations, given estimates of their uncertainties.

Initially, we attempt to search for a flat-ramp-flat structure. We fixed the middle ramp part with a dip angle of 15°, and the angles of the updip and downdip flat part are allowed to vary above (4–16 km) and below (18–26 km) a certain depth, respectively (hereafter called the updip and downdip transition depths). Our results indicate that a wide range of downdip angles can fit the data equally well (Figure 5.11), which indicates that the data cannot resolve the downdip fault geometry well. However, both the kinematic and stress-driven afterslip models can identify the downdip afterslip, although it is much smaller than the updip afterslip (see Section 5.4.4 for analysis about the downdip afterslip).

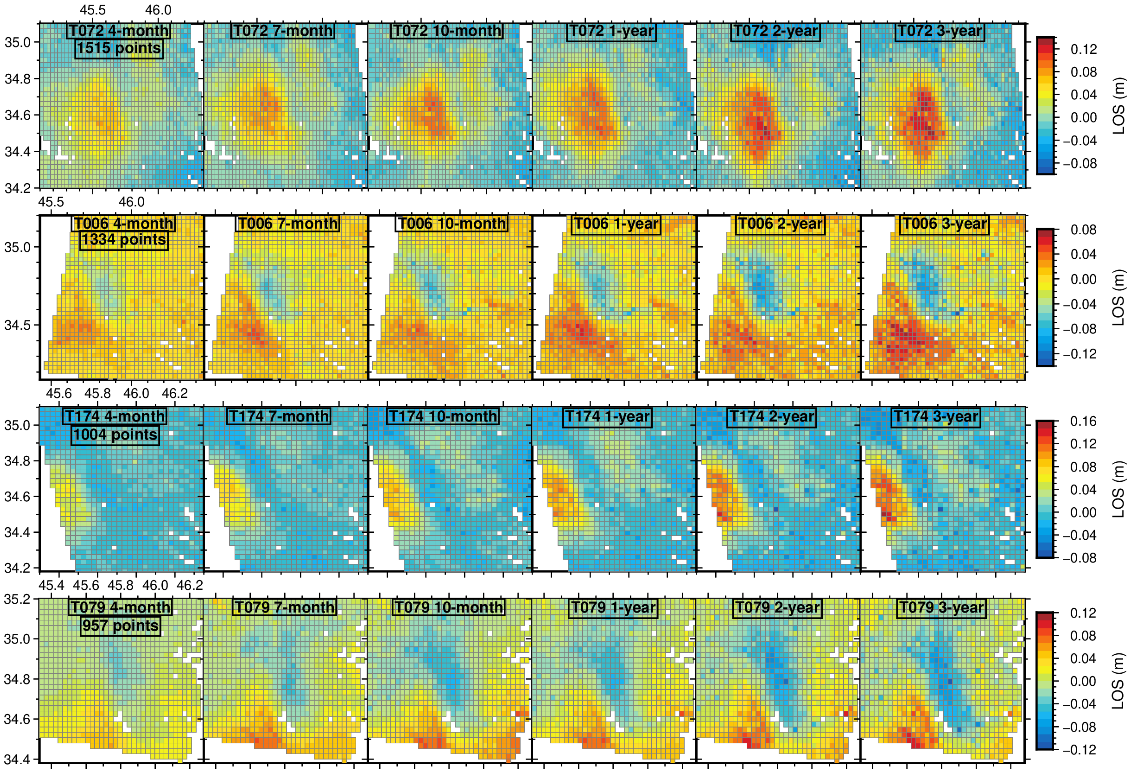

Figure 5.10: The downsampled points from 4-track postseismic InSAR time series. Please note different color bars for each row.

For the updip geometry, the results show that the updip angle should be lower than 15°, but the data have little resolution for the transition depth and dip angles smaller than 15° (Figure 5.11). To reduce the number of searching parameters, we fix the downdip angle to 15° so that there are only two variables (updip angle and transition depth), and we reselect the updip angle and transition depth. The results show that the updip angle and transition depth should be lower than 10° and ∼12 km, respectively, based on the 4-month, 2-, and 3-year postseismic observations (Figures 5.12a, 5.12e and 5.12f). However, the updip geometry cannot be constrained very well by the postseismic observations at 7, 10 months, and 1 year after the event (Figures 5.12b–d), which may be attributed to observation noise (Figure 5.13).

Additional searches are also performed based on the 8-, 9-, 13-, and 15-month postseismic observations, the results are found to be similar with those of 4-month, 2-, and 3-year postseismic observations (Figure 5.14). In addition to the residual noises, considering the variations in transition depth, geological background and local stratigraphic profile, a more complex fault structure is likely to be triggered (see Section 5.5). Overall, most postseismic observations favor a ramp-flat structure in which the flat angle should be lower than 10°, but the refined structure of updip geometry cannot be resolved very well with InSAR observations.

Because it is difficult to make a compromise between the updip angle and upper transition depth, and considering the interface between the sedimentary cover and basement, we propose a ramp-flat fault (anti-listric fault, to be strict) model with a variable dip at depth with the following equation:

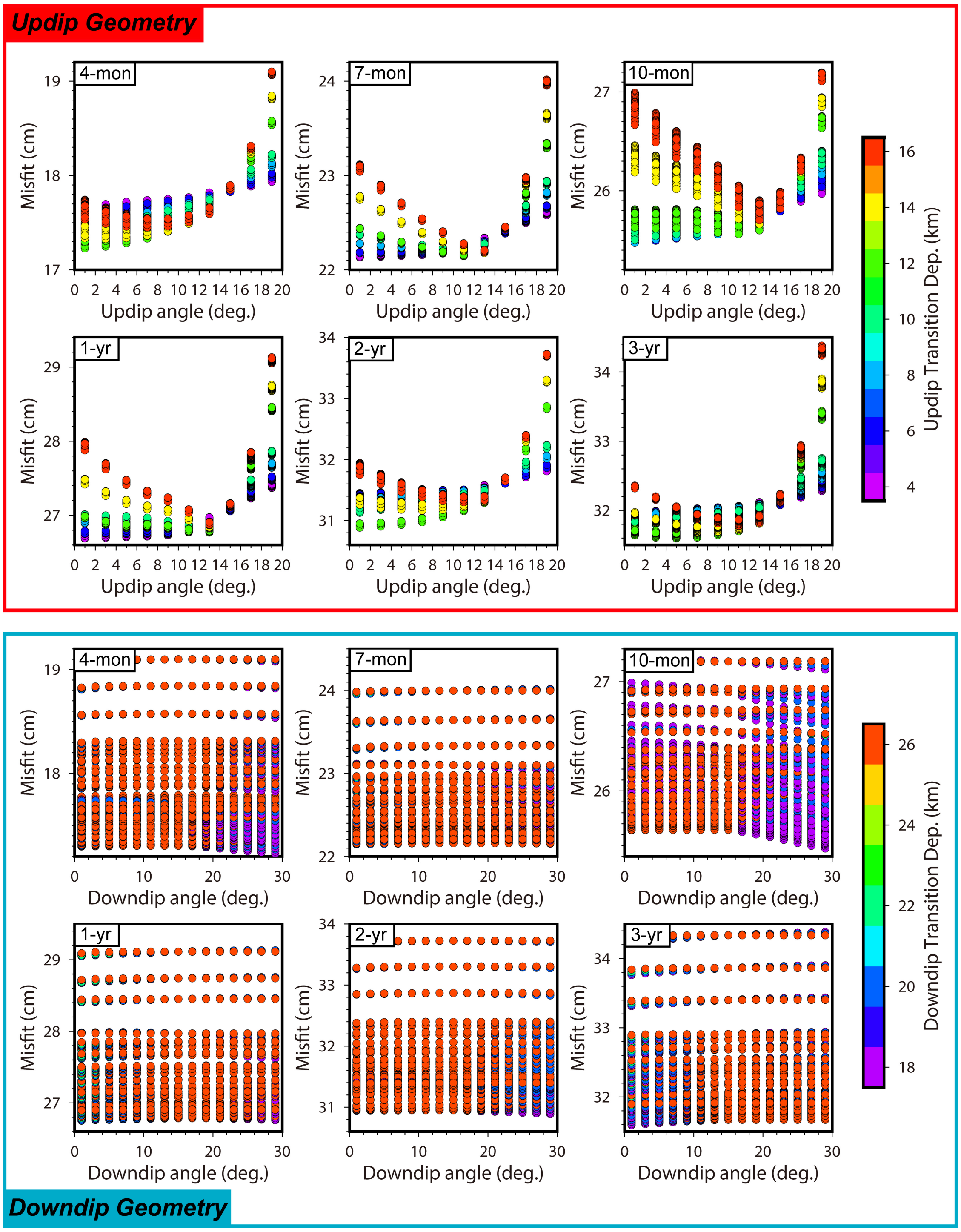

Figure 5.11: Misfit for searching the dip angles and transition depths of updip and downdip fault geometry with the observations of 4, 7, 10 months and 1, 2, 3 years after the mainshock.

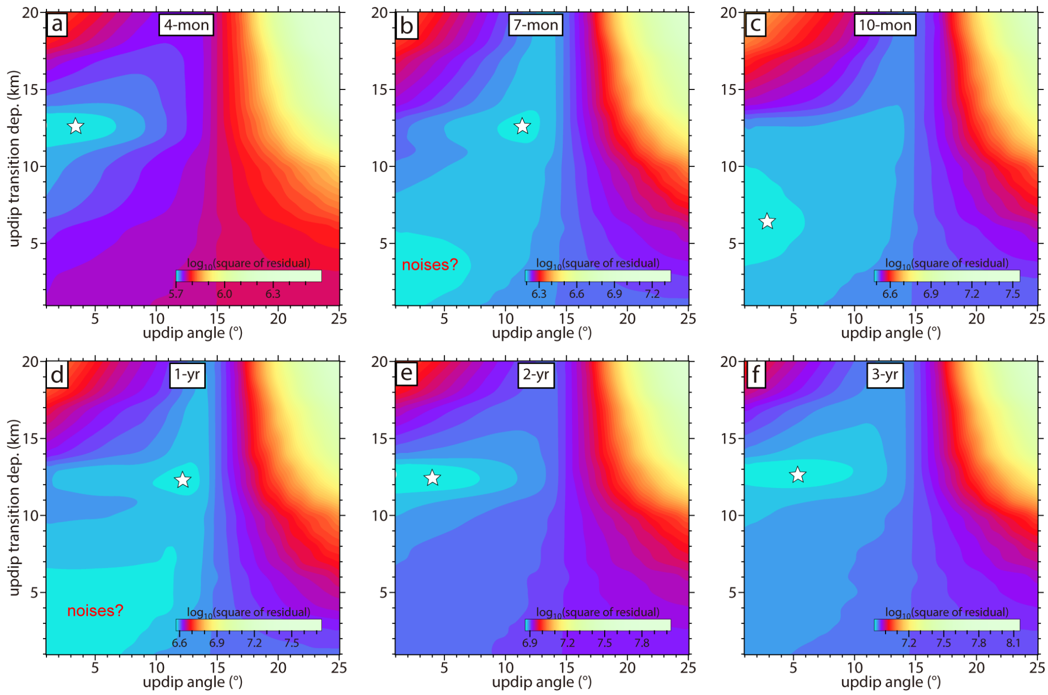

Figure 5.12: Misfit for searching the updip angles and transition depths with the postseismic observations of 4, 7, 10 months and 1, 2, 3 years after the mainshock. Star indicates the best searching result.

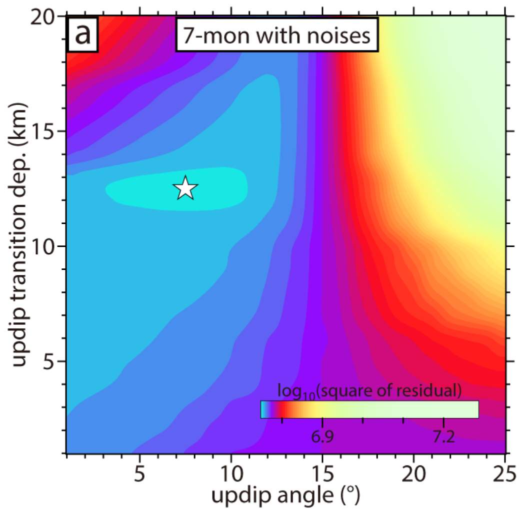

Figure 5.13: The results of searching the dip angles and transition depths of updip fault geometry with the 7-month observations perturbed with the Gaussian noises which are based on the standard deviations of far-field noises.

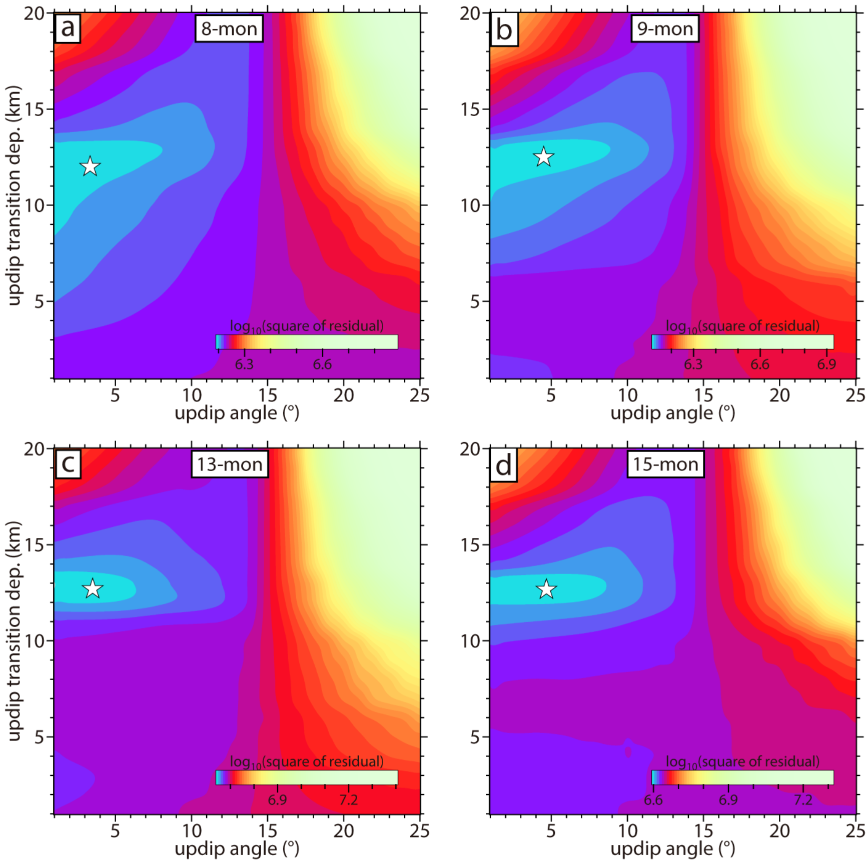

Figure 5.14: The results of searching the dip angles and transition depths of updip fault geometry with the observations of 8, 9, 13 and 15 months after the mainshock.

$$\mathrm{dip}_n = \begin{cases} -4 \cdot (13.4 - n) + \mathrm{dip}_{n+1}, & n < 13.4, \\ 15, & n \geq 13.4, \end{cases} \tag{5.2}$$

the symbols used, and their meanings, are the same as those in Equation 5.1. We adopted $a = -4$ (dip angle would be 0 at ~10 km) since the basement depth is approximately 8-13 km. Moreover, this ramp-flat fault is consistent with the aftershock locations updip of the coseismic rupture (Figure 5.7c), and this model strongly resembles the ramp-flat structure proposed by Barnhart et al. (2018) and Wang and Bürgmann (2020). The ramp-and-flat model can not only explain the postseismic deformation but can also produce a slightly smaller misfit (38.3 cm) for coseismic inversion than the planar model (38.9 cm). Therefore, we take the ramp-flat coseismic model as our preferred model in the following inversions.

As shown in Figure 5.15, the afterslip model based on the ramp-flat fault is mainly concentrated updip of the coseismic rupture, despite some localized deep afterslip. The spatiotemporal evolution of the kinematic afterslip model agrees well with the aftershock locations updip of the fault, which indicates that the aftershocks may have been triggered by aseismic afterslip. The 3-year maximum kinematic afterslip is approximately 1.2 m, which is similar to that of the stress-driven afterslip model (Figure 5.18 and 5.19, see Section 5.4.2 for details). The cumulative moment release calculated from the 3-year

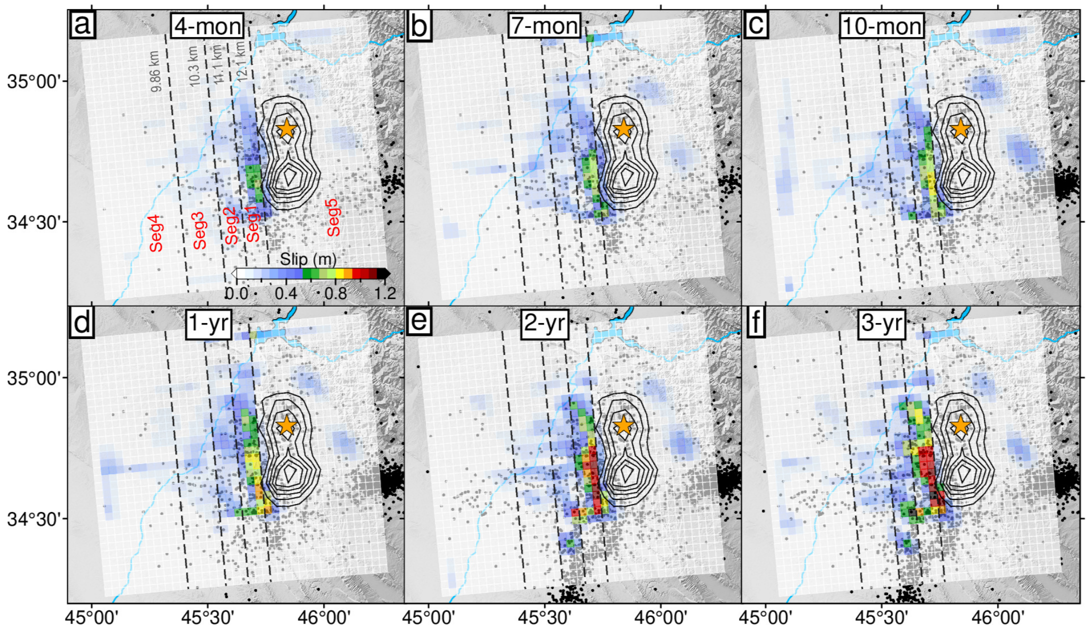

Figure 5.15: Spatiotemporal evolution of aftershocks and kinematic afterslip model. Black contours and orange star represent the coseismic slip model at 1-m intervals and the epicenter of the Mw 7.3 mainshock, respectively. The black dots indicated the aftershocks are from IRSC catalogue. The black dashed lines which divide the fault plane into 5 parts (seg 1-5) represent the fault depth.

afterslip model is approximately 2.6×10^{19} Nm, which is equivalent to the moment of a Mw 6.9 earthquake. The kinematic afterslip model can predict the InSAR observations spatiotemporally well (Figure 5.16).

5.4.2 Stress-Driven Afterslip Models

We calculate the time-dependent evolution of rate-strengthening friction faults to coseismic stress change with the application of Unicycle codes (Barbot et al., 2017). The fault slip rate controlled by a purely rate-strengthening friction law can be shown as (e.g., Barbot et al., 2009):

$$V = 2V_0 \sinh \frac{\Delta\tau}{(a-b)\sigma} \tag{5.3}$$

This is a steady state simplification of the rate-and-state friction law (e.g., Marone, 1998a; Marone et al., 1991), where V_0 and $a-b$ represent the reference slip rate before the coseismic shear stress changes $\Delta\tau$ are applied and frictional parameter of the material, respectively, and σ is the effective normal stress on the fault. Here V_0 does not correspond directly to the interseismic slip rate (e.g., Barbot et al., 2009). The steady state assumption is valid as the magnitude of the afterslip for the 2017 Sarpol-e Zahab earthquake ($>10^{-1}$ m) is greater than the laboratory-derived values of D_c which are on the order of 10^{-5} m (e.g., Marone, 1998a). In our simulations, we select the main coseismic area at depths of ∼12–20 km with coseismic slip > 0.8 m as the Unicycle input model. V_0 and $(a-b)\sigma$, which are considered constitutive parameters, are searched based on the misfit between InSAR observations and simulations.

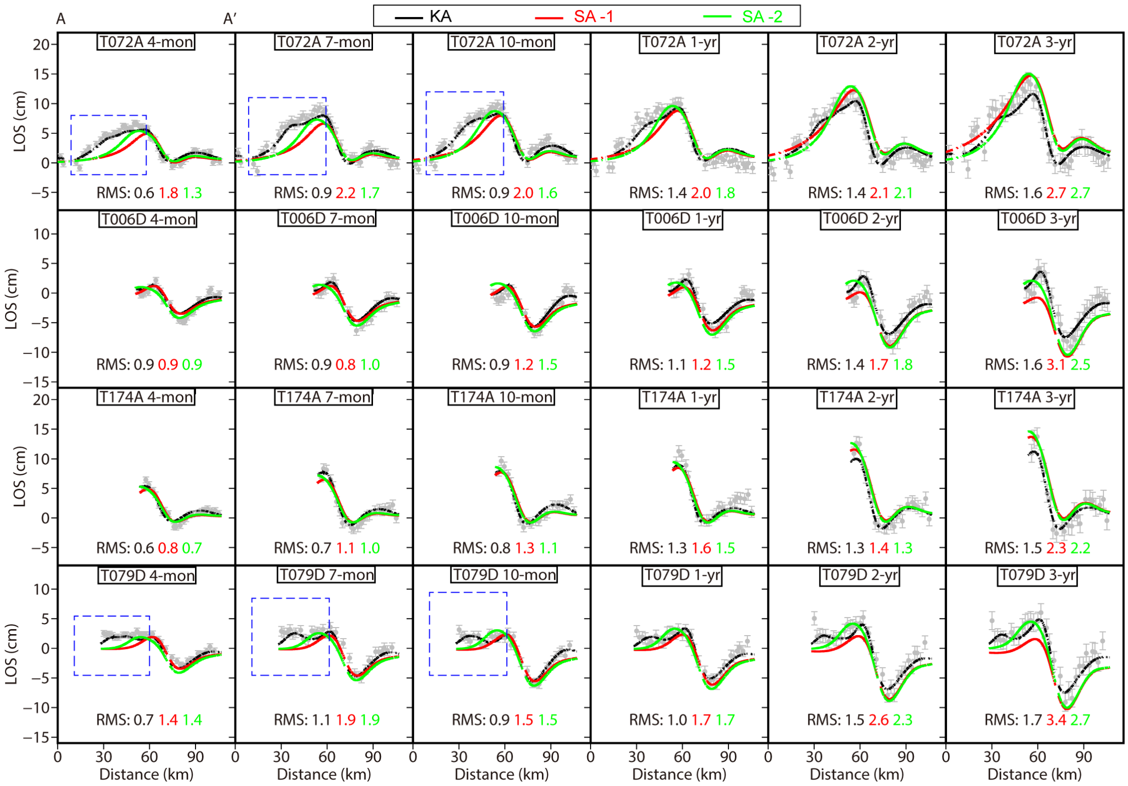

Figure 5.16: Fitting between InSAR observations and simulations from 4 months to 3 years after the mainshock along profile AA' in Figure 5.3a-d. The gray error bars are based on the InSAR observations, which represent the far-field noises from VCM. The black, red and green lines represent the simulations from Kinematic Afterslip (KA) and Stress-driven Afterslip model 1 (SA-1 model) and Stress-driven Afterslip model 2 (SA-2 model), respectively. The blue dashed boxes indicate the underfitting between observations and simulations from stress-driven afterslip models.

We search five parameters including V_0 and $(a-b)\sigma$ updip and downdip of the coseismic rupture and the transition depth where the fictional properties of fault rocks change. Initially, the 3-year postseismic deformation time series from the four tracks of Sentinel-1 images are used for searching the five parameters. We employ the simulated annealing algorithm (e.g., Kirkpatrick et al., 1983) to search the global optimal solutions of the constitutive parameters, but there is still a possibility of obtaining the local minima due to the complexity of the chosen parameters for simulated annealing. Thus, we perform a number of iterative operations with different chosen parameters of the algorithm, initial values and boundary constraints. The solution that yields the minimum data misfit is selected as the final optimal solution. The results show that the updip V_0 and $(a-b)\sigma$ are 0.078 m/yr and 0.56 MPa, respectively; for the downdip part of the fault, V_0 and $(a-b)\sigma$ converge to 0.009 m/yr and 1.84 MPa, respectively; the optimal transition depth is approximately 12.14 km (Table 5.1; Figure 5.17). This model (herein referred to as the SA-1 afterslip model, Figure 5.18) reflects the friction contrast between the updip and downdip sections of the fault and requires afterslip downdip of the coseismic rupture to explain 3-year postseismic deformation, which confirms the results of Wang and Bürgmann (2020). However, this afterslip model cannot predict the temporal evolution of the postseismic deformation well; for example, it underestimates the early postseismic deformation (Figure 5.16).

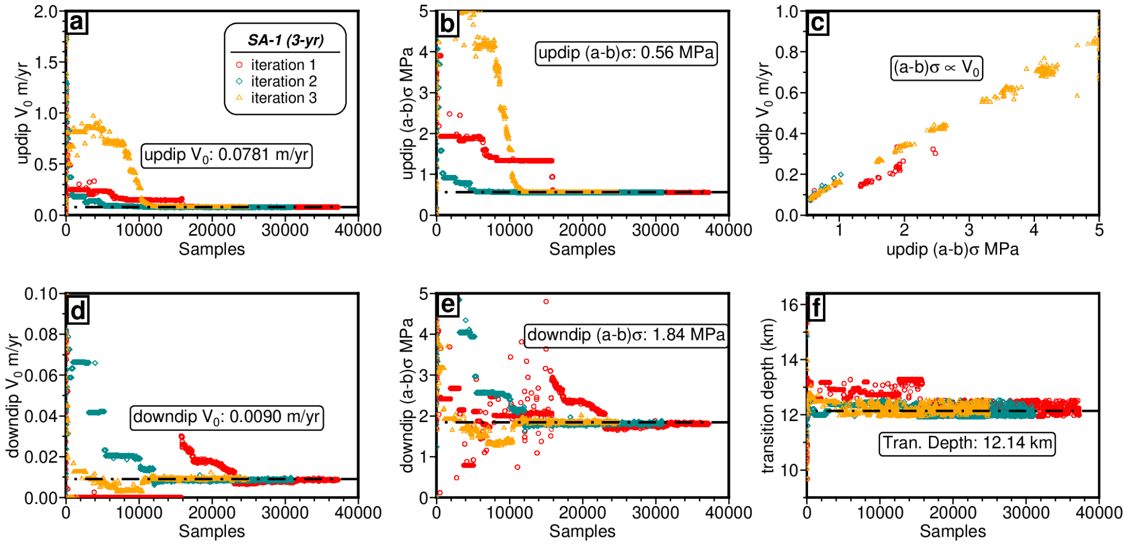

Figure 5.17: Convergence process with simulated annealing algorithms for V_0 and $(a-b)\sigma$ updip (a and b) and downdip (d and e) of the coseismic rupture, as well as the transition depth (f), based on the 3-year postseismic deformation time series. The trade-off correlation between updip V_0 and $(a-b)\sigma$ are shown in (c). The black dash-dotted line represents the optimal parameter.

Table 5.1: Constitutive parameters derived from this study and previous work.

data/source	updip flat		downdip ramp		transition depth (km)
	$(a-b)\sigma$ (MPa)	V_0 (m/yr)	$(a-b)\sigma$ (MPa)	V_0 (m/yr)	
4-month	0.56[a]	0.084	1.84[a]	0.0200	12.14[a]
7-month	0.56[a]	0.084	1.84[a]	0.0195	12.14[a]
10-month	0.56[a]	0.084	1.84[a]	0.0175	12.14[a]
1-year	0.56[a]	0.084	1.84[a]	0.0168	12.14[a]
2-year	0.56[a]	0.084	1.84[a]	0.0114	12.14[a]
3-year	0.56	0.084	1.84	0.0090	12.14
Wang and Bürgmann (2020)	2.7	1.42	0.073	0.06	-

[a]Note. the variable is fixed.

Our purpose is to seek a rate-strengthening afterslip model that is capable of estimating InSAR observations spatiotemporally. We attempt to verify whether the depth-varying fault friction is responsible for the underfitting of the SA-1 model in Figure 5.16, which is reasonable because of the weak sedimentary multilayers along depth (see Section 5.5). Considering that the afterslip is mainly concentrated around the updip section of the fault, there are four segments for the updip part of the coseismic rupture (seg 1-4 in Figures 5.15a, 5.18a and 5.19a). Because more fault segments and too many searching parameters would make it difficult to obtain convergence, as well as the trade-off between $(a-b)\sigma$ and V_0 (Figure 5.17c), we choose to fix some parameters according to the search results

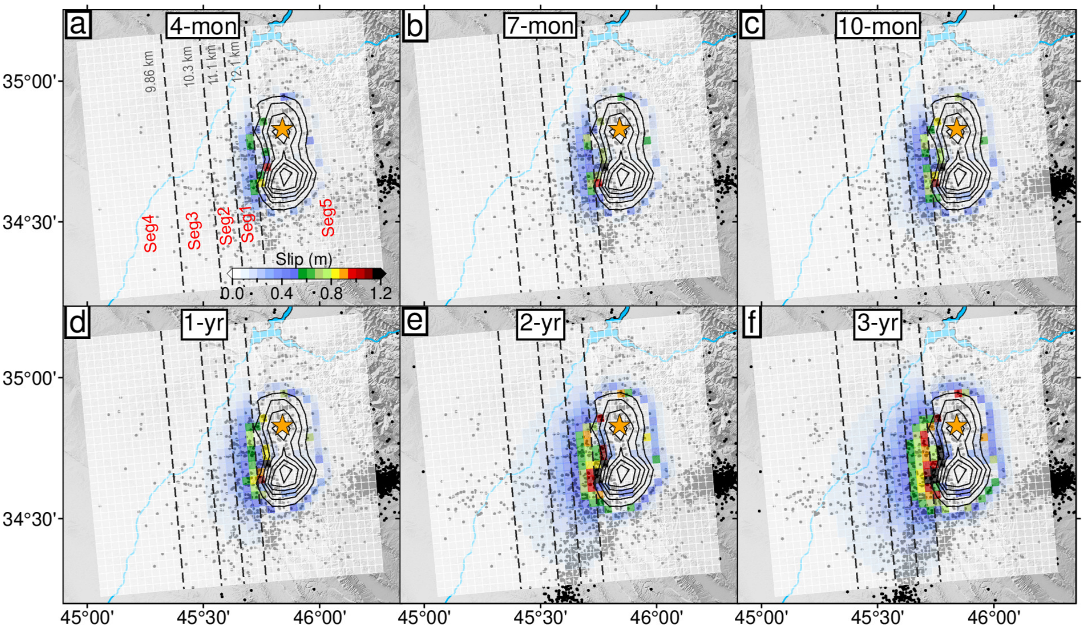

Figure 5.18: Spatiotemporal evolution of aftershocks and stress-driven afterslip model 1 (SA-1 model). Black contours and orange star represent the coseismic slip model at 1-m intervals and the epicenter of the Mw 7.3 mainshock, respectively. The black dots indicated the aftershocks are from IRSC catalogue. The black dashed lines which divide the fault plane into 5 parts (seg 1-5) represent the fault depth.

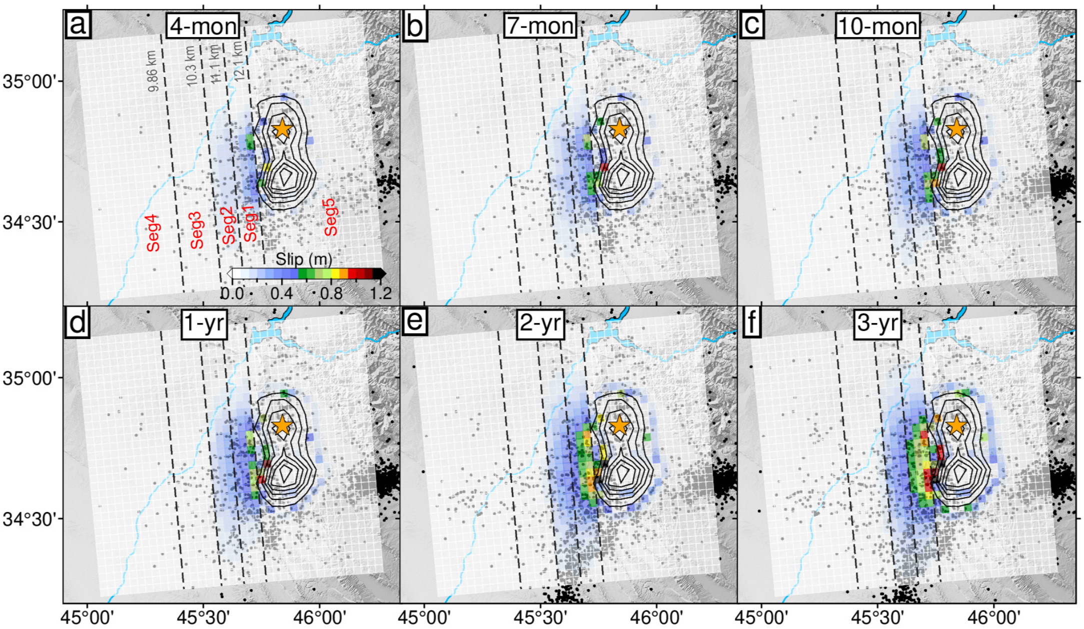

Figure 5.19: Similar to SA-1 model in Figure 5.18, this is the spatiotemporal evolution of aftershocks and stress-driven afterslip model 2 (SA-2 model).

of the SA-1 model (Table 5.1): the $(a-b)\sigma$ and V_0 of the downdip section (seg 5) are fixed at 1.84 MPa and 0.009 m/yr, respectively; we force no afterslip on seg 4 with V_0 to be 0 m/yr because little or no afterslip is indicated by the kinematic and SA-1 afterslip models (Figure 5.15 and 5.18); V_0 is fixed at 0.078 m/yr for seg 1 to seg 3, and then $(a-b)\sigma$ is to be searched.

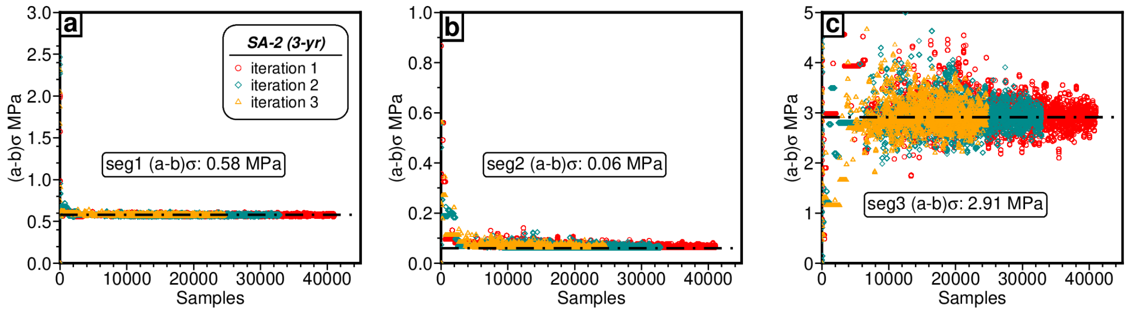

Figure 5.20: Convergence process with simulated annealing algorithms for $(a-b)\sigma$ of seg 1-3 updip of the coseismic rupture. The black dash-dotted line represents the optimal parameter.

As shown in Figure 5.20, the $(a-b)\sigma$ values for seg 1 to seg 3 are 0.58, 0.06, and 2.91 MPa, respectively. Compared with the SA-1 afterslip model which features friction contrast between up- and downdip parts of the fault, this multisegment model (herein called the SA-2 afterslip model, Figure 5.19) can better explain the observations (Figure 5.16). In addition, the sedimentary stratigraphy consists of different lithologies at different depths in this region, for example, limestones, shales, marls, evaporites, and sandstones at depths ranging from 8-12 km from the Cambrian to Triassic (e.g., Casciello et al., 2009; Sadeghi and Yassaghi, 2016; Le Garzic et al., 2019)(please see Section 5.5). Different lithological units could exert a significant control on the friction properties of the fault plane (Floyd et al., 2016; Yassaghi and Marone, 2019). Thus, even though the SA-2 model does not significantly improve the Root Mean Square (RMS) error (Figure 5.16), the depth-varying friction is more physically plausible given the depth-dependent mechanical stratigraphy in this region. However, there is still underfitting between the early postseismic deformation and simulations, and the 3-year postseismic deformation for ascending Track T072A is overestimated (Figure 5.16), which indicates that the fault friction may be more complex than we thought.

5.4.3 The Combination of Stress-driven Afterslip and Viscoelastic Relaxation

The contribution of viscoelastic relaxation is still in question: Wang and Bürgmann (2020) suggested that the viscoelastic relaxation deformation within 1 year is less than 1 cm, while Lv et al. (2020) argued that the viscoelastic contribution from 6 months to 2.5 years after mainshock is relatively significant. In this section, we attempt to explore a combined postseismic mechanism of viscoelastic relaxation and stress-driven afterslip. Based on the 7-month, 1-year and 3-year simulations from SA-2 afterslip model, we adopt PSGRN/PSCMP (Wang et al., 2006) to simulate the corresponding viscoelastic relaxation using a layered elastic model and by exploring a range of Maxwell viscosities (from 1×10^{17} to 1×10^{20} Pa s). The same coseismic slip distribution used for estimating stress-driven afterslip is employed to calculate viscoelastic relaxation. We find that the best-fitting viscosity is no less than 10^{19} Pa s from these three models (Figure 5.21a), which is consistent with the best estimates of the rheological viscosity from Lv et al. (2020). However, the viscoelastic response with a viscosity on the order of 10^{19} Pa s cannot match the deformation pattern of ascending tracks (Figure 5.21b). More importantly, the maximum range change of 3-year viscoelastic relaxation for descending tracks is about 1.5 cm (Figure 5.21b), which is only about one tenth of the 3-year cumulative LOS deformation. Our viscoelastic simulations are in good agreement with Wang and Bürgmann (2020), indicating the viscoelastic relaxation is unlikely to be a dominant postseismic mechanism.

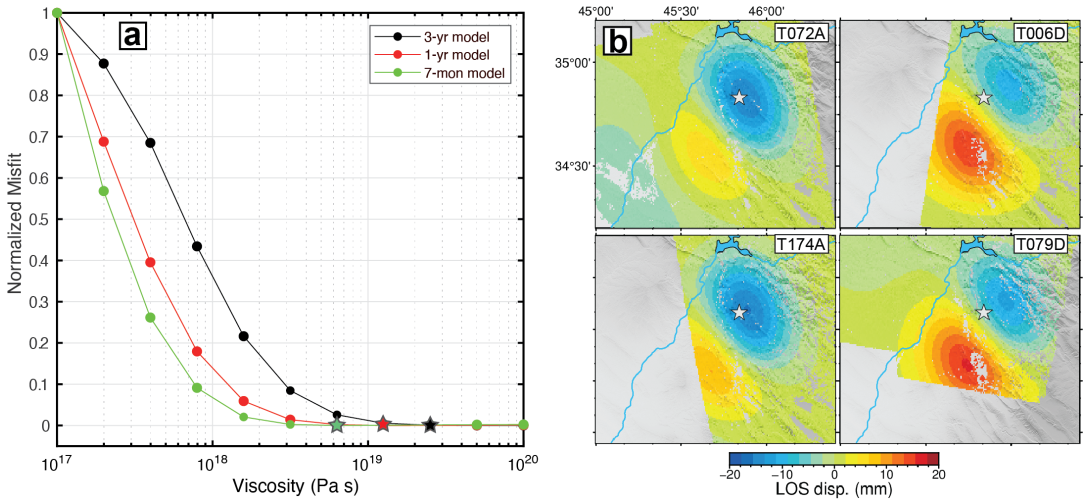

Figure 5.21: Searching result of viscosity and the corresponding simulations due to viscoelastic relaxation. (a) The trade-off between normalized misfit of 7-month, 1-year and 3-year postseismic observations and the viscosities. The green, red and black stars represent the best viscosity based on 7-month, 1-year and 3-year postseismic observations. (b) The simulated LOS displacements of T072A, T006D, T174A and T079D due to the viscoelastic relaxation 3 year after the mainshock, using a layer model with the best estimates of the rheological viscosity from Lv et al. (2020). The viscoelastic simulations are similar to the results of Wang and Bürgmann (2020). The viscosities of Maxwell lower crust between 30 km to 40 km and Maxwell upper mantle lower than 40 km are 1×10^{19} and 3×10^{19} Pa s, respectively. The gray star is the epicenter of the 2017 Sarpol-e Zahab earthquake.

5.4.4 The Analysis about the Downdip Afterslip

Given that the viscoelastic response is negligible, the afterslip therefore should be the dominant postseismic deformation source. The postseismic slip models derived from some previous studies (e.g., Barnhart et al., 2018; Feng et al., 2018; Liu and Xu, 2019) indicate no clear afterslip on downdip section of the coseismic rupture, while Wang and Bürgmann (2020) suggest that the inferred peak afterslip in the downdip section is $\sim$0.3 m. The kinematic and rate-strengthening afterslip models from this study also indicate smaller downdip afterslip than updip (Figure 5.15, 5.18 and 5.19). In this section, the detailed analysis and discussion are performed to identify the deep afterslip downdip of the coseismic rupture.

5.4.4.1 The Impact of Aftershocks on Afterslip

In this study, we firstly removed the coseismic deformation of the two bigger aftershocks (the Mw 5.9 earthquake on 25 August 2018 and the Mw 6.3 earthquake on 25 November 2018) from our InSAR postseismic time series, based on the fault models proposed by Fathian et al. (2021) (Figure 5.4). We find that the two ∼M 6 aftershocks do have an influence on the afterslip models of mainshock, especially the Mw 5.9 aftershock would contribute to the afterslip on downdip part of the mainshock (Figure 5.22). Although afterslip introduced by aftershocks is not too much (Figure 5.22c), it makes the recovery of afterslip details downdip of the mainshock more challenging.

In this study, therefore, the coseismic deformation of the two aftershocks is removed, but we ignore their postseismic signals because the aftershocks are much smaller than mainshock and it is very tricky to separate the postseismic deformation of the aftershocks from that of the mainshock. After reducing the localized signal contaminations of the aftershocks, we attempt to analyze the downdip afterslip from the perspective of the data accuracy and model resolution.

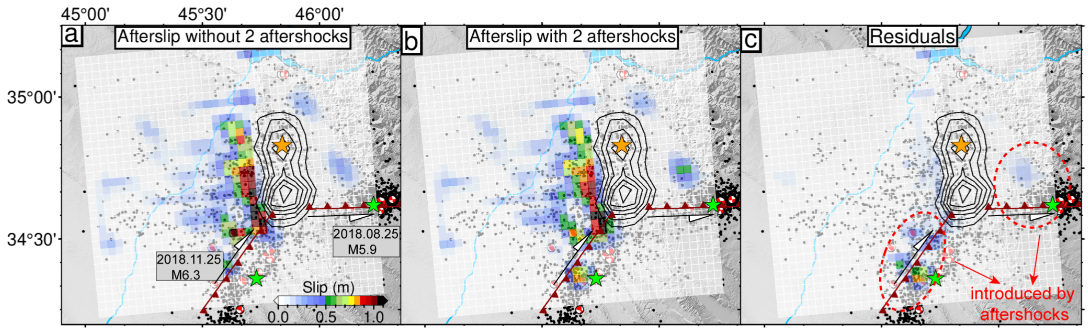

Figure 5.22: ∼3-year kinematic afterslip models after (a) and before (b) removing the coseismic deformation of the two ∼M 6 aftershocks; (c) the difference between (a) and (b). Black contours and orange star represent the coseismic slip model at 1-m intervals and the epicenter of the Mw 7.3 mainshock, respectively. Green stars and dark red faults represent the locations of the two bigger aftershocks and the corresponding fault traces from Fathian et al. (2021). The black dots and red beach balls indicated the aftershocks are from IRSC catalogue.

5.4.4.2 The Impact of Residual Noises on Afterslip

As the topography grows from west to east in the Zagros (Figure 5.3g), the surface deformation downdip of the coseismic rupture may be contaminated by the topography-correlated atmospheric noises. Even though we reduced the atmospheric noises with GACOS (Yu et al., 2018), we firstly compare the noise levels of ∼1-year cumulative postseismic observations between our results and Wang and Bürgmann (2020). We mask the deformation field and selected non-deforming areas in the ∼1-year descending and ascending InSAR observations from Wang and Bürgmann (2020) and our study (Figure 5.23), to calculate far-field deformation which can be regarded as the residual noises after corrections. Our residual noise level is slightly higher than that of Wang and Bürgmann (2020), with the residual noises of ∼13 mm and ∼8 mm from both studies, respectively (Figure 5.23).

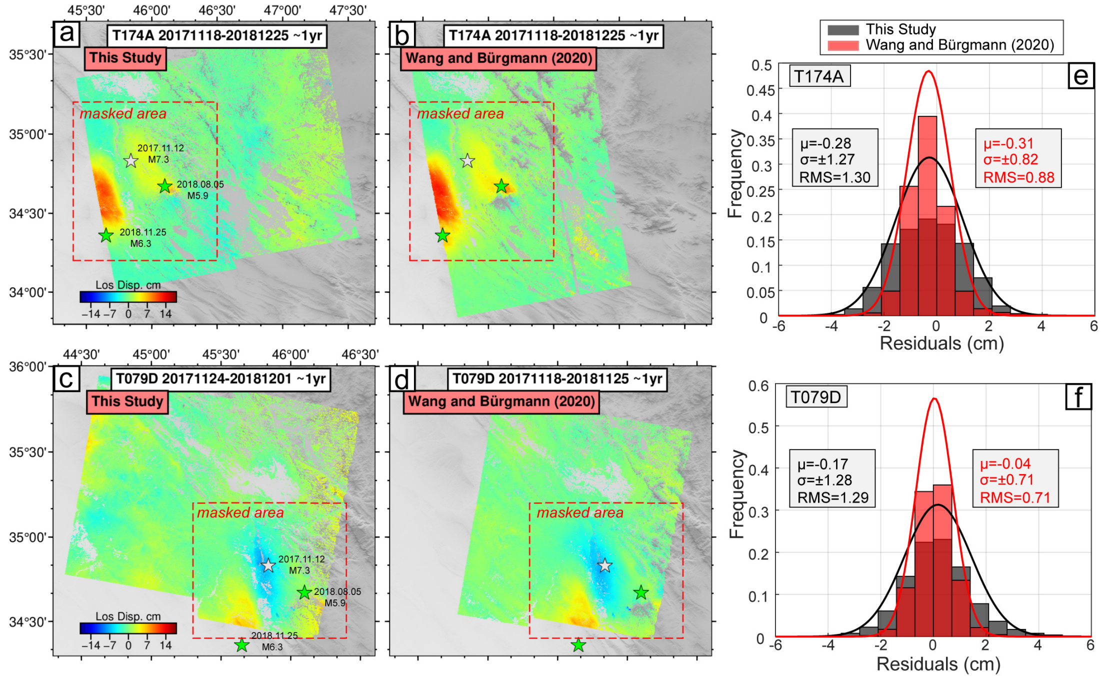

Figure 5.23: ~1-year cumulative postseismic LOS displacements of ascending track T174A (a and b) and descending track T079D (c and d) from our study and Wang and Bürgmann (2020). The red dashed boxes in (a-d) represent the masked areas with deformation fields. The residuals (e and f) are calculated from the non-deforming areas with T174A and T079D.

Then we quantitatively analyze how much influence the residual atmospheric noises would exert on the postseismic afterslip, particularly the afterslip downdip of the coseismic rupture. We generate 100 simulations perturbed with far-field noises based on four-track InSAR observations to estimate the standard deviation from 100 afterslip distributions. The standard deviation could reflect the absolute variability of slip affected by observation noises on every slip patch. Our results show the observation noises have more influence on the strike-slip components than dip-slip components (Figure 5.24). Even though the slip uncertainties downdip of coseismic rupture (maximum ~0.1 m) are much smaller than those of updip section (maximum ~0.2 m), the maximum afterslip is ~0.3 m and ~1.2 m for downdip and updip section of the coseismic rupture (Figure 5.15, 5.18 and 5.19), respectively. Thus, the observation noises could lead to more significant slip errors on downdip section than updip section of the coseismic rupture and could make it more difficult to distinguish the downdip afterslip, which may explain the absence of the downdip afterslip derived from some previous studies (e.g., Barnhart et al., 2018; Feng et al., 2018; Liu and Xu, 2019). Overall, both of our kinematic and stress-driven afterslip models indicate the existence of the downdip afterslip (Figure 5.15, 5.18, 5.19 and Table 5.1), which confirms the results from Wang and Bürgmann (2020). The differences of downdip slip amplitudes between this study and Wang and Bürgmann (2020) may be partly due to the slightly higher noise level of our observations.

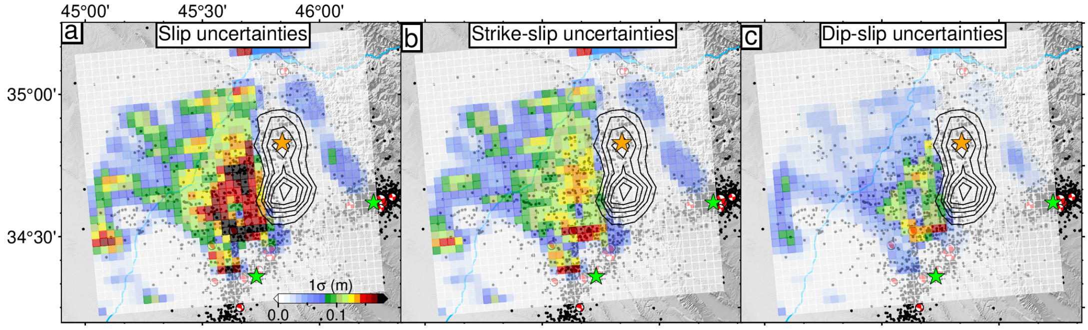

Figure 5.24: Standard deviation calculated with 100 perturbed datasets to simulate the influence of observation noises to model slip. (a), (b) and (c) are the total slip uncertainties, strike- and dip-slip uncertainties, respectively. Black contours and orange star represent the coseismic slip model at 1-m intervals and the epicenter of the Mw 7.3 mainshock, respectively. Green stars represent the locations of the two ∼M 6 aftershocks. The black dots and red beach balls indicated the aftershocks are from IRSC catalogue.

5.4.4.3 Postseismic Checkerboard Tests

Apart from the slip uncertainties from InSAR data noises, the fault model resolution, i.e., the checkerboard tests with ∼0.6- and ∼0.4-m slip also indicate that the afterslip resolution downdip of the coseismic rupture would be lower with the smaller and deeper fault slip (Figure 5.25). Similar with the coseismic checkerboard resolution tests (see Section 5.3.2), we carry out the postseismic checkerboard tests based on the postseismic downsampled points (Figure 5.10) but with smaller fault slip (∼0.6-m and ∼0.4-m, Figure 5.25) which is similar with the afterslip magnitude downdip of the coseismic rupture. Our results show the recovery is only about 50% below the depth of 20 km (Figure 5.25). Rather than being precisely located, the slip asperities downdip direction of the coseismic rupture tend to be smeared over several sub-patches, which suggests the decreased resolving power of downdip slip as the depth increases. Overall, without considering the influence of the aftershocks, clearly distinguishing the downdip afterslip would strongly rely on the data noise level and model resolution.

Stress-driven afterslip models could also provide us some valuable insights into the evolution of downdip afterslip. For stress-driven afterslip model (SA-1 model), because the trade-off between the $(a-b)\sigma$ and V_0 (Figure 5.17c), we fix $(a-b)\sigma$ with 0.56 MPa and 1.84 MPa for updip and downdip part of the fault, respectively (Table 5.1), and search for the V_0 with the time series of the 4-, 7-, 10-month and 1-, 2-year postseismic deformation. The results show that as the afterslip relaxes the coseismic stress changes, the downdip V_0 decays rapidly (Table 5.1), which may be attributed to the short-term existence of the downdip afterslip. Compared with the almost invariant $(a-b)\sigma$ and V_0 of the updip section, the variation of the V_0 may also indicate the friction property evolves with time.

5.5 Discussion

5.5.1 Postseismic Deformation and Topography Growth

The basement-involved faulting is found to significantly contribute to the topography growth and crustal shortening across the foreland of the mountain range via postseismic de-

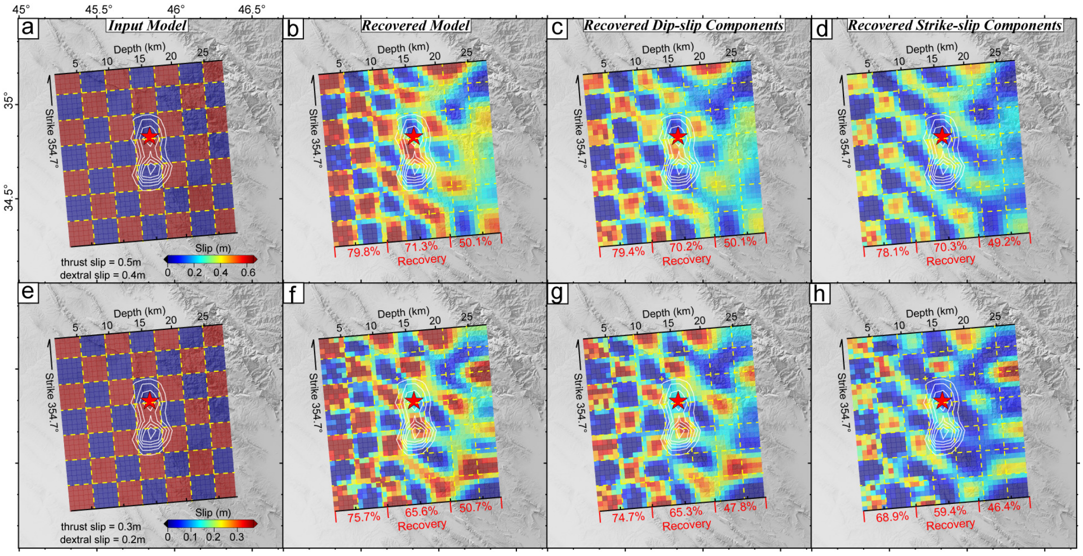

Figure 5.25: Checkerboard tests for the postseismic model resolution. The input models with ∼0.6-m (a) and ∼0.4-m (e) slip are used for simulating synthetic surface displacements. The slip patterns (b and f), dip- (c and g) and strike-slip (d and h) components are recovered by the synthetic InSAR displacements. The recovery is defined as recovery $= \left(1 - \frac{\sum_{i=1}^{n} |S_i - S'i|}{\sum_{i=1}^{n} |S_i|}\right) \times 100\%$, where S_i and S_i' represent the input slip and inverted slip of i_{th} patch, respectively, and the n is the number of patches with input slip.

formation. The 2.5-dimension (2.5D) deformation fields decomposed from ascending track T072A and descending track T079D indicate a long-wavelength postseismic deformation (∼80 km) along profile AA' (Figure 5.3a-d and 5.3g, Figure 5.26). The decomposed 2.5-dimension deformation is consistent with the simulations of the kinematic afterslip model (Figure 5.3g-h), though the decomposed displacements neglect the south-north component because of the near-polar satellite orbits. In Figure 5.3g and Figure 5.26, postseismic deformation clearly contribute to the topography uplift western of MFF (from Zagros Foredeep Fault to MFF), while minor subsidence occurs east of the MFF (from MFF to High Zagros Fault). The westward movements across these faults highlight the aseismic contribution to the crustal shortening in the foreland of the Zagros.

Afterslip could continue for several decades after the mainshock (e.g., Zhou et al., 2016) and such long-lived postseismic slip may be related with the fold growth. Daout et al. (2021) proposes kinematic folding models which feature anelastic fold buckling to explain the shallow, long-term (more than 10 years), short-wavelength postseismic deformation of Mw ∼6 thrust earthquakes in the North Qaidam fold-and-thrust system. For the 2017 Sarpol-e Zahab earthquake, however, the longer-wavelength postseismic signals may indicate the deeper postseismic deformation sources (Figure 5.26), while the shorter-term (∼3 year in this study) postseismic observations may mainly be attributed to localized afterslip or more complex deep structures. We will discuss the reactivation of the complex structures in Section 5.5.4. As for the contribution of distributed aseismic deformation to the surface growth, longer postseismic observations may be needed to help us have a better understanding whether there is long-lived postseismic contribution to the topography growth in this region (Daout et al., 2021).

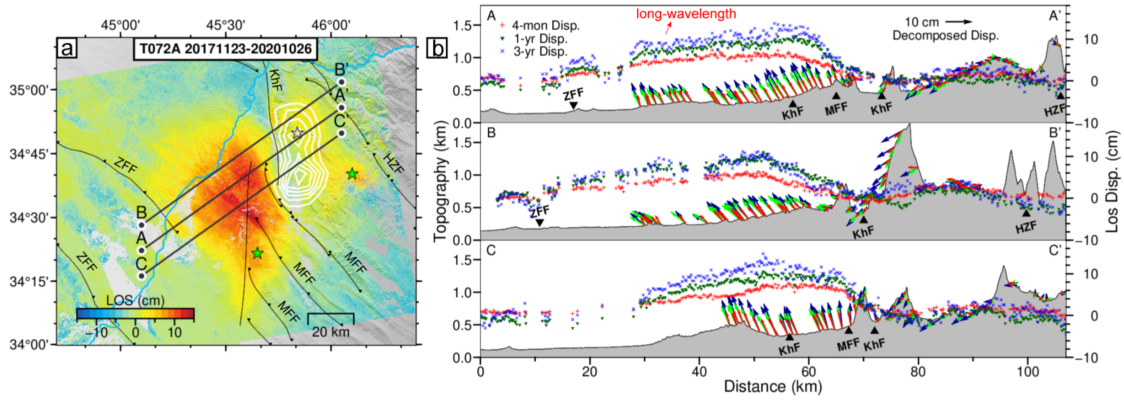

Figure 5.26: The contribution of postseismic deformation to topography.(a) ∼3-year cumulative postseismic deformation of ascending track T072A. White contours and gray star represent the coseismic slip model at 1-m intervals and the epicenter of the Mw 7.3 mainshock, respectively. The green stars are the two ∼M 6 aftershocks. (b) shows the contribution of postseismic deformation to topography along profile AA', BB' and CC' in (a). The red, green and dark blue vectors are the 2.5-dimension deformation (quasi-eastward and quasi-upward) of 4 months, 1 year and 3 years after the mainshock, separately, which are decomposed from ascending track T072A and descending track T079D.

5.5.2 Comparison with Previous Afterslip Models

5.5.2.1 Kinematic Afterslip Models

The studies from Barnhart et al. (2018) and Wang and Bürgmann (2020) using about 4-month and 1-year postseismic deformation, respectively, support a ramp-and-flat structure beneath the foreland of the Zagros. Both of the studies suggest significant afterslip concentrated on the shallow dipping (∼1-10°) flat updip of the coseismic rupture. In this study, we use 4-, 7-, 10-, 12-, 24- and 36-month postseismic data to search the postseismic fault structure. Our result confirms the dip angle of the updip afterslip plane should be lower than 10° and the data have limited resolution for smaller dip angles. Dutta et al. (2021) recently proposed a Bayesian method to simultaneously estimate the non-planar fault geometry and the distributed fault slip, which may be helpful for parameterizing the refined fault geometry. However, in this study, we choose not to do more investigations about the fault geometry and we propose a ramp-flat fault to model the spatiotemporal evolution of the postseismic deformation, given the depth of basal decollement in this region. Barnhart et al. (2018) and Wang and Bürgmann (2020) indicate the optimal afterslip depth is about 10-14 km, which is also similar to our study as models in our study with transition depth at ∼12 km yield minimum data misfit (Figure 5.12 and 5.14). Our kinematic afterslip models also favor a minor deep afterslip, which is in agreement with Wang and Bürgmann (2020).

5.5.2.2 Stress-driven Afterslip Models

Comparing with four parameters searched by Wang and Bürgmann (2020) with Bayesian inversion, we initially searched five constitutive parameters of rate-strengthening afterslip model which consists of two fault segments (SA-1 afterslip model) with simulated annealing algorithm. However, we find a multi-segment fault model with lateral friction variation

(SA-2 afterslip model) could better explain the spatiotemporal evolution of the postseismic deformation, which indicates that there is not only the friction contrast between the updip and downdip part of the fault plane (Wang and Bürgmann, 2020), but also a depth-varying friction heterogeneity along fault plane.

For the two-segment SA-1 afterslip model, however, our preferred results are different from Wang and Bürgmann (2020). Based on the 1-year postseismic deformation, Wang and Bürgmann (2020) derived the best values of V_0 and $(a-b)\sigma$ to be 1.42 m/yr and 2.7 MPa for updip, 0.06 m/yr and 0.073 MPa for downdip part, which is very different from ours: 0.078 m/yr and 0.56 MPa for updip, 0.0090 m/yr and 1.84 MPa for downdip part (Table 5.1). Such a difference may partly result from the trade-off of V_0 and $(a-b)\sigma$ (Figure 5.17c), which is also suggested by Wang and Bürgmann (2020). The trade-off between V_0 and $(a-b)\sigma$ is expected as equivalent V on the fault patches would be produced with low values of V_0 or high values of $(a-b)\sigma$ (see Equation 5.3). This strong trade-off would lead to non-unique solutions and make it difficult to distinguish the models. Furthermore, the real physical meaning of V_0 may be rather complex (e.g., Barbot et al., 2009; Perfettini and Avouac, 2007). Given such strong trade-off and the ambiguity of physical meanings of the constitutive parameters, one of $(a-b)\sigma$ and V_0 is usually chosen to be fixed in some studies (e.g., Tian et al., 2020, 2021).

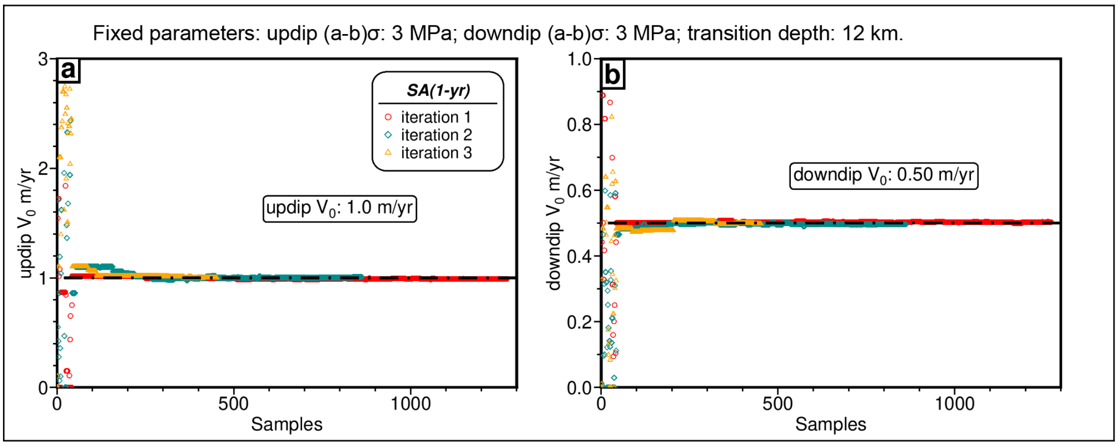

Figure 5.27: Convergence process with simulated annealing algorithms for updip and downdip of the fault with fixed constitutive parameters $(a-b)\sigma$ and the transition depth, based on the simulations perturbed with observation noises. The black dash-dotted line represents the optimal parameter.

To examine the data sensitivities for these constitutive parameters of the two-segment SA-1 afterslip model, we fixed V_0 and $(a-b)\sigma$ with 1.0 m/yr and 3.0 MPa for updip, 0.5 m/yr and 3.0 MPa for downdip part and transition depth of 12 km, to get the evolution of the simulations. Then we add Gaussian noises with 1-cm standard deviation (Figure 5.23) to the simulations to get the perturbed simulations which are used as "observations" for searching the parameters. Firstly, we search the up- and down-dip V_0 with the transition depth and up- and down-dip $(a-b)\sigma$ being fixed; then the up- and down-dip $(a-b)\sigma$ is searched with the transition depth and up- and down-dip V_0 being fixed. The results show that, under the disturbance of observation noises, the constitutive parameters can converge to the original values rapidly (Figure 5.27 and 5.28), which indicates that the existing noise level may not affect the convergence of the parameters. Therefore, without

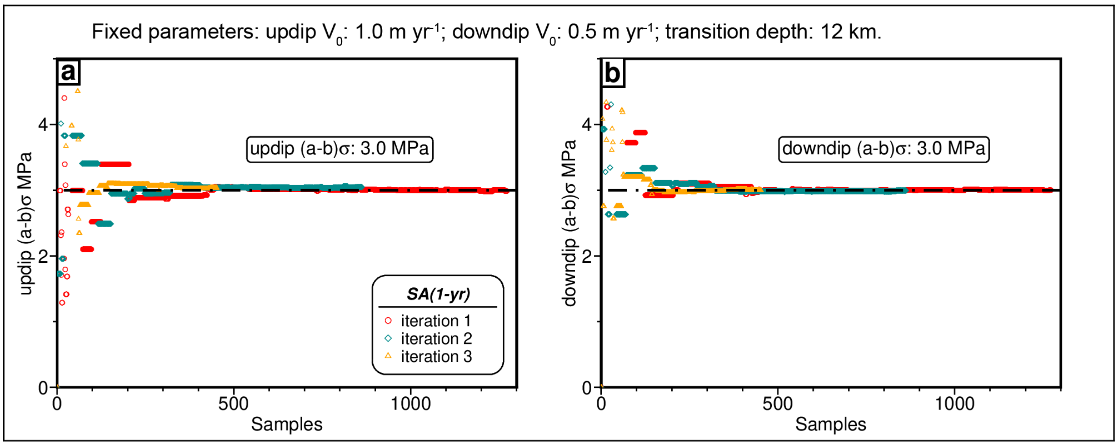

Figure 5.28: Same to Figure 5.27 but with updip and downdip V_0 and transition depth being fixed.

considering the observations noises, the difference of the searched parameters between this study and Wang and Bürgmann (2020) may attribute to the strong trade-off between V_0 and $(a-b)\sigma$, the difference of InSAR observations used for searching as well as the difference of the input coseismic model and the fault configuration used for stress-driven afterslip modeling.

5.5.3 The Location of Afterslip and the Contribution from Viscoelastic Flow

Afterslip is a rather complex physical process and has not been clearly understood yet. In the framework of rate-and-state friction law, the coseismic rupture usually initiates and propagates in the velocity-weakening area and its propagation tends to be impeded by the shallower unconsolidated sediments. This sediment layer with velocity-strengthening properties then would be strongly loaded and drives afterslip in consequence (Marone et al., 1991). At the downdip direction of the coseismic rupture in midcrustal depths, a transition of fault friction from velocity-weakening stick slip to velocity-strengthening brittle creep would be expected because the temperature gets higher with depth (e.g., Marone, 1998b; Perfettini and Avouac, 2004). However, ductile flow may also be activated at depth (e.g., lower crust or upper mantle) where temperature gets higher enough to produce dislocation creep (Perfettini and Avouac, 2004). Overall, as predicted by rate-and-state dependent friction law, in most cases afterslip tends to occur at the periphery of the coseismic rupture, where slip deficit is left by mainshocks.

For some thrust earthquakes which share similar tectonic settings with the 2017 Sarpol-e Zahab earthquake like the 1999 Chi-chi, the 2005 Kashmir and the 2015 Gorkha earthquake, the significant afterslip occurred at the downdip portion of the fault, in conjunction with possible viscoelastic relaxation (e.g., Hsu et al., 2002; Zhao et al., 2017; Wang and Fialko, 2014, 2015, 2018; Diao et al., 2021). However, much smaller deep afterslip downdip of the coseismic rupture than updip (Figure 5.15, 5.18 and 5.19) is required by our kinematic and mechanical afterslip models for this 2017 Sarpol-e Zahab event; the viscoelastic response is also negligible as the estimated viscosity should be greater than 10^{19} Pa s, which confirms the result from Wang and Bürgmann (2020). The existence of minor downdip afterslip is physically reasonable (e.g., Zhao et al., 2017; Diao et al., 2021) because of the velocity-strengthening frictional properties at depths below the coseismic rupture. Prominent afterslip updip of the coseismic rupture from our afterslip models coincides with the strong frictional contrast between updip and downdip portion of the fault. Such frictional contrast may correspond to stratigraphic relations between sedimentary cover and crystalline basement (Figure 5.29). The transition depth from both of kinematic and rate-strengthening afterslip models is convergent to 12-13 km which also agrees well with the Hormuz evaporites according to stratigraphic profiles of this region (Figure 5.29, e.g., Casciello et al., 2009; Vergés et al., 2011), indicating the possible depth of cover-basement interface. Chen et al. (2018) performed joint inversion using satellite radar and teleseismic data and found the coseismic rupture velocity is more rapid downdip ($\sim$3.2 km/s) of the fault than updip ($\sim$1.5 km/s), which supports the assumption that the mainshock ruptured the cover-basement interface and was impeded by the updip sedimentary rocks. Subsequently, the loose sediments with velocity-strengthening properties are more prone to drive afterslip Marone et al. (1991). The existence of such a low friction interface due to the transition between different geological units may be the reason that the spatial location of afterslip following the 2017 Sarpol-e Zahab event is different from other events shared similar tectonic settings.

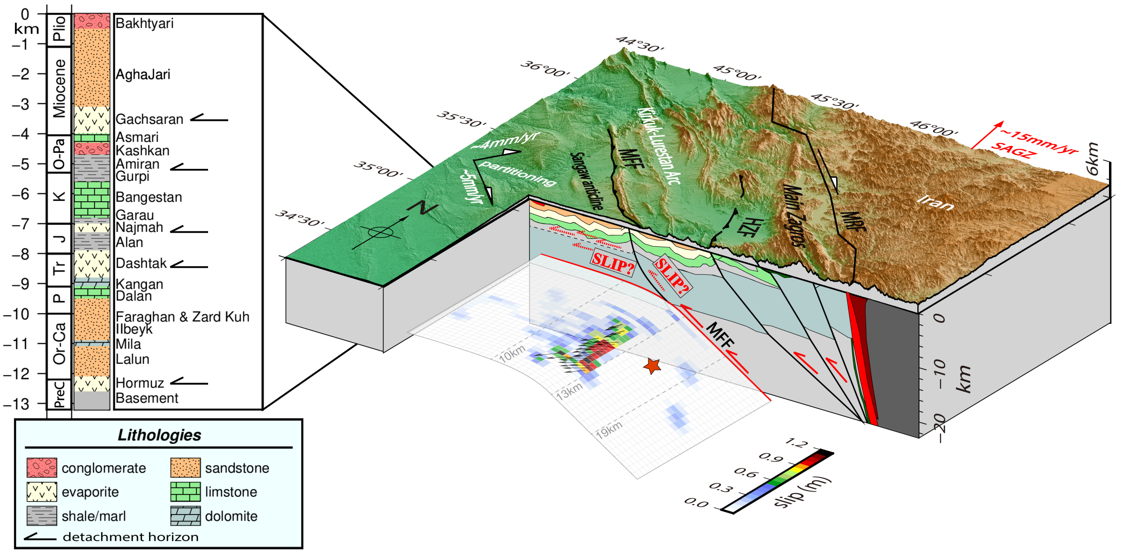

Figure 5.29: 3-D block diagram showing the tectonics, fault geometry, kinematic afterslip of 3 years after the mainshock and stratigraphic column in northwestern Zagros. The geological cross-section data is from National Iranian Oil company. The GPS velocity (SAGZ site) is from Khorrami et al. (2019). The simplified stratigraphic profile with approximate depths for Lurestan Salient is modified and referred from previous studies: Casciello et al. (2009); Vergés et al. (2011); Sadeghi and Yassaghi (2016); Le Garzic et al. (2019). Red star represents the epicenter of the 2017 Sarpol-e Zahab earthquake. Stratigraphy ages and main faults are abbreviated as follows: Plio, Pliocene; O-Pa, Oligocene-Eocene-Palaeocene; K, Cretaceous; J, Jurassic; Tr, Triassic; P, Permian; Or-Ca, Ordovician-Cambrian; PreC, PreCambrian; MRF: Main Recent Fault; HZF: High Zagros Fault; MFF: Mountain Front Fault.

5.5.4 The Underfitting of Stress-driven Afterslip Models

The spatiotemporal pattern of postseismic slip for the 2017 Sarpol-e Zahab earthquake may be even more complex. As shown in Figure 5.16, the rate-strengthening afterslip model tends to underestimate the earlier part of the postseismic deformation west of the deformation field for T072A and T079D (the blue dashed boxes in Figure 5.16). Such far-field underfitting is unlikely to be attributed to the poroelastic rebound and viscoelastic relaxation, because the former mainly contribute to near-field range changes (e.g., Peltzer et al., 1998) while the latter is negligible. The signal contamination from the two ∼M 6 aftershocks, i.e., the 2018 Mw 5.9 event and the Mw 6.3 event, can also be ruled out because it is far from the northwestern deformation area along profile AA' (Figure 5.3 and 5.26). Given our afterslip inversions, geological data and local structures, some inferences about this underfitting are discussed as follows:

5.5.4.1 A More Complex Frictional Heterogeneity of Fault Plane

Compared with the stress-driven afterslip models, the kinematic afterslip model can explain the deformation spatiotemporally (Figure 5.16), which may be due to a more complex spatial heterogeneity of frictional properties of the fault rock. In this study, we divide the fault into five segments with different frictional properties and we have to fix some constitutive parameters, otherwise too many searching parameters would make it difficult to simulate the postseismic deformation. Even though such a multi-segment model with depth-varying fault friction is proposed, the real frictional properties along the fault may be even more complex. Liu and Xu (2019) studied the coseismic and postseismic fault slip based on the logarithmic model which can be associated with the simple 1D spring-slider analogue model (e.g., Marone et al., 1991), and then they discussed the frictional properties of the seismogenic fault of the 2017 Sarpol-e Zahab earthquake. They derived a complex distribution of the friction parameter $a-b$ of the fault plane, even though the result would strongly rely on the priori assumptions of model parameters (e.g., the average thickness of the velocity-strengthening region). In this study, the rate-strengthening regime is a steady-state approximation of the complete rate-and-state friction law, the trade-off between V_0 and $(a-b)\sigma$ as well as the ambiguity of their physical meanings make the characterization of the fault rheology a difficult challenge, while the number of parameters of the complete rate-and-state friction law may be too large to reliably estimate (for example, the afterslip of Nias, Parkfield and Denali earthquakes in full rate-and-state law analyzed by Helmstetter and Shaw (2009)). Hence, in this chapter, we choose not to give more in-depth discussion about the frictional strength of the fault based on the rate-and-state friction law. In next Chapter 6, we will explore such possibility of a more complex fault geometry and fault friction using longer InSAR observations and FEM models.

5.5.4.2 The Reactivation of the Blind Mountain Front Fault

With the integration of geological field data, seismic reflection profiles and well data, Tavani et al. (2018) concluded that the 2017 mainshock ruptured along the blind MFF which also matches our geological cross section data well (Figure 5.29). The reactivated MFF and the inherited structures break through the basal basement to the sedimentary cover in the vicinity of the mainshock (Figure 5.29), and are supposed to be responsible for the multiple geological structures triggered during the mainshock, for example, the Miringeh fault (Tavani et al., 2018; Figure 5.3g). Such thrusting system is also considered as one of the folding mechanisms (e.g., McQuarrie, 2004; Alavi, 2007) and has been constructed to model the anticline evolution on the top of MFF in Lurestan Arc (Emami et al., 2010). Thus, except for the significant postseismic slip occurred on the cover-basement interface at the depth of ~12 km indicated by our kinematic and stress-driven afterslip models, the updip portion of the MFF or the inherited structures in sedimentary cover may also be reactivated by the mainshock and possible postseismic slip was triggered there (Figure 5.29).

5.5.4.3 Triggered Slip on the Shallower Detachment Horizons

O'Brien (1950) firstly subdivided the Zagros vertical profile into five major structural units from shallow to deep: incompetent group, upper mobile group, competent group, lower mobile group and basement group. Even though the "competent group" at the depth of ~5-10 km was established by this mechanical stratigraphy, multiple weak detachment horizons, often of shales, marls or evaporites, are present from northwest to southeast of Lurestan salient (Figure 5.29, e.g., Casciello et al., 2009; Sadeghi and Yassaghi, 2016; Le Garzic et al., 2019). The weak sedimentary multi-layers in which the folds and thrust faults developed are prone to deform and directly control the distribution and process of the folds in this region (Casciello et al., 2009; Vergés et al., 2011). Thus, we suggest the rupture of the 2017 Sarpol-e Zahab earthquake may propagate across these decoupling horizons. A similar interpretation by Copley et al. (2015) was suggested for the 2014 Mw 6.2 Mormori earthquake in this region. The possible triggered postseismic slip on the local detachments (Figure 5.29) may further couple and contribute to the fold evolutions within the sedimentary cover. The structural interpretation for this assumption is that the stress changes due to the 2017 mainshock were not fully decoupled by the low friction interface (Hormuz unit) at the cover-basement transition, and then upward propagated into the incompetent detachment levels along MFF (Figure 5.29). Overall, the basement thrusting system may pierce into the Phanerozoic cover and multiple decoupling layers are involved and triggered by the mainshock (Figure 5.29). Thus, the two-layer decoupled model would be not enough to interpret the complex interaction between the thin-, thick-skinned shortening and the seismicity in the Zagros (e.g., Barnhart et al., 2018; Wang and Bürgmann, 2020). The 2017 Sarpol-e Zahab event may be regarded as a representative example in the Zagros which contributes to both of the thick- and thin-skinned shortening in seismic and aseismic way.

5.6 Conclusion

The 2017 Mw 7.3 Sarpol-e Zahab earthquake is the largest instrumentally recorded event to have ruptured in the ZFTB. The coseismic and postseismic models associated with this event are investigated with InSAR observations in this study. The main conclusions of this work are as follows:

1. Linear inversions reveal a planar fault which is capable of explaining the coseismic deformation better than the listric faults. The coseismic rupture highlights a unilaterally southward rupture involving sequential rupture of two asperities along a dextral-thrust fault.

2. The kinematic afterslip model can predict the spatiotemporal variations in the postseismic deformation well. A multi-segment stress-driven afterslip model which features depth-varying friction is required to better explain the evolution of postseismic deformation, compared with a two-segment stress-driven afterslip model. The transition depth inverted from kinematic afterslip and rate-strengthening afterslip models is ∼12 km, which can be best explained by the cover-basement interface.

3. The best-fitting viscosity based on the combination mechanisms of viscoelastic relaxation and stress-driven afterslip models is greater than 10^{19} Pa s, in which the viscoelastic contribution to the postseismic deformation is negligible.

4. Both the kinematic and stress-driven afterslip models feature minor afterslip (∼0.3 m) downdip of the coseismic rupture, although resolving it clearly would strongly rely on data accuracy and model resolution.

5. The mismatch between the early postseismic deformation west of deformation field and stress-driven afterslip simulations can be explained either by a more complex spatial heterogeneity of frictional property of the fault rock, or by triggered slip on more complex geological structures, for example, the updip of MFF and the inherited structures, as well as the multiple detachment horizons there.

6 In-depth Exploration of Fault Complexity Revealed by Frictional Afterslip

6.1 Introduction

In last chapter (Chapter 5), we discussed the possibilities of the reactivation of the complex MFF and a more complex frictional heterogeneity on it because of the underfitting of the stress-driven afterslip models. According on geologic cross-section data, the fault structure includes basement splay faults within the northwest ZFTB that have penetrated and offset the overlying structures of the sedimentary cover. This complexity may be considered as a reason why the stress-driven afterslip models proposed in Chapter 5 underestimated early postseismic deformation to the west.

In this chapter[1], to further explore the fault structural complexity and the fault frictional complexity of the 2017 Mw 7.3 Sarpol-e Zahab earthquake following Chpter 5, here we employ models based on 2D FEM constrained by InSAR observations to model the $\sim$4.5-year postseismic deformation of the 2017 Mw 7.3 Sarpol-e Zahab event. We first process about 4.5 year InSAR observations of two tracks of Sentinel-1 data to get the postseismic deformation field and then explored the coseismic kinematic models with planar faults using the InSAR coseismic deformation from our previous work (Guo et al., 2022). Based on the best coseismic slip model and by gradually increasing the fault structure complexity, we developed frictional afterslip models incorporating three types of fault geometries. These include (1) planar faults, (2) ramp-flat faults, and (3) the combined models of splay and ramp-flat faults. Our aim was to explore the influence of geometrically complex fault structures and their frictional variations on postseismic surface displacements. For simplicity, we only considered 2D FEM models along a profile AA' shown in Figure 6.1. The structure of this chapter is as follows:

- Section 6.2 explains the InSAR processing strategy and InSAR time series results.
- Section 6.3 presents the FEM modeling strategy and results. We explain the model setups and approach in which three different fault structures are explored and then we give the modeling results.
- In Section 6.4, we firstly discuss the influence of other factors (viscoelastic relaxation, data noise, medium parameters) to the modeling results and the insights from relocated aftershocks and geologic cross-sections. Then we give a further discussion about the fault complexities of other big earthquakes occurred in similar tectonic background.
- Section 6.5 is a brief conclusion of this chapter.

[1] This chapter expands upon the paper published by the candidate from the publication Guo et al. (2024). Co-authors of this publication are acknowledged.

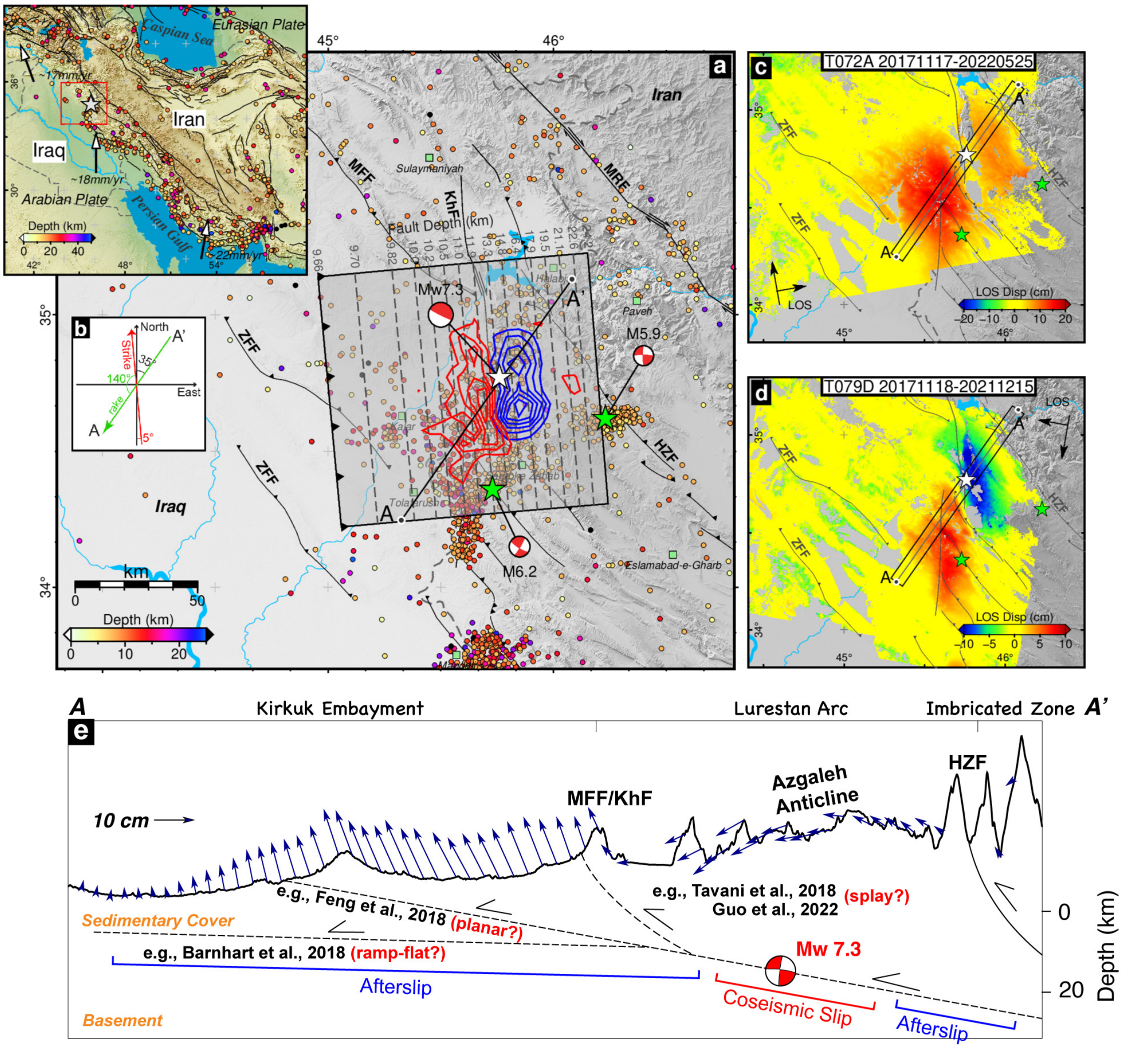

Figure 6.1: Tectonic background and the InSAR results of the 2017 Mw 7.3 Sarpol-e Zahab earthquake, postseismic InSAR observations and conceptual faults derived and modified from previous studies. (a) tectonic setting of the mainshock. The finite element method models used in this study are constructed along profile AA'. The white and green stars are the mainshock and the two ~M 6 aftershocks respectively. The black box represents the ramp-flat fault plane proposed by our previous study (Guo et al., 2022). The blue and red contours with 1- and 0.2-m intervals indicate the coseismic slip and cumulative 3-year kinematic afterslip from Guo et al. (2022), respectively. The colored dots are the earthquakes (from 2006 to 2022) from IRSC with magnitudes larger than M 3. (b) is a schematic diagram showing the strike direction and slip direction of the fault proposed by our previous work (Guo et al., 2022). (c) is the ~4.5-year cumulative postseismic deformation of ascending track T072A. (d) is same with (c) but it shows a descending track T079D. (e) indicates the conceptual faults derived and modified from previous studies, including planar fault (e.g., Feng et al., 2018), ramp-flat fault (e.g., Barnhart et al., 2018; Wang and Bürgmann, 2020) and splay fault (e.g., Tavani et al., 2018). The dark blue vectors are the 2.5-dimension deformation 4 years after the mainshock, which are decomposed from ascending Track T072A and descending Track T079D. The width of the swath in (c) and (d) is 8 km. The red beach balls are the focal mechanisms of the 2017 Mw 7.3 mainshock and two ~M 6 aftershocks. ZFF: Zagros Foredeep Fault; MRF: Main Recent Fault; HZF: High Zagros Fault; and MFF: Mountain Front Fault; KhF: Khanaqin fault.

6.2 InSAR Observations

6.2.1 Time Series Analysis 4.5 Years after Mainshcok

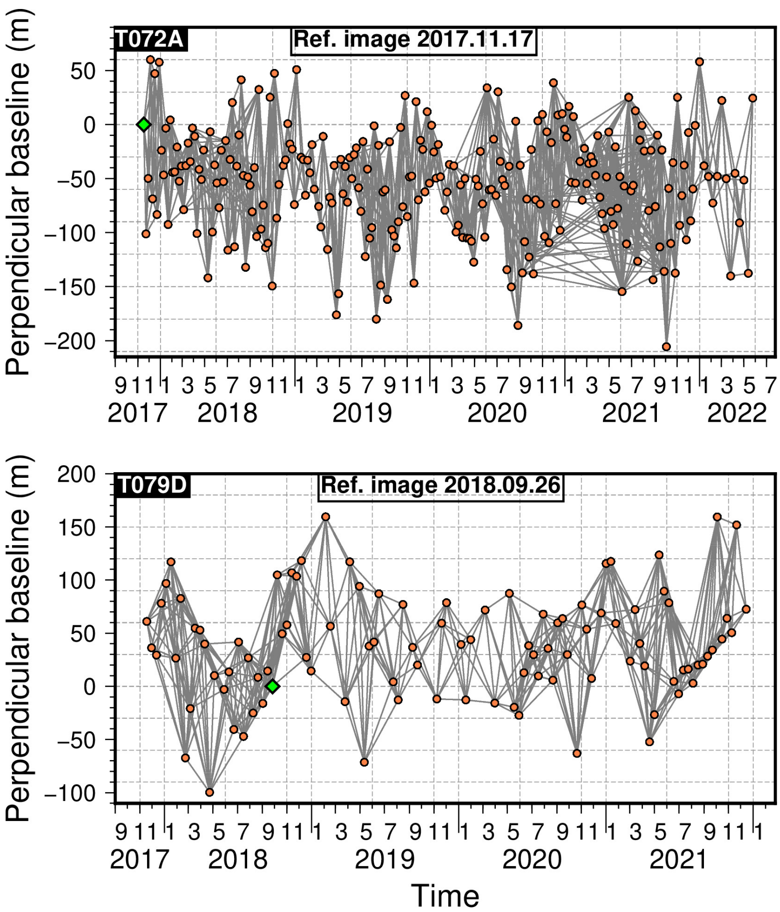

Figure 6.2: The baseline networks for the two sentinel-1 tracks (T072A and T079D). The green diamond represents the reference image.

We processed Sentinel-1 SAR images from two tracks, including an ascending track T072A and a descending track T079D, to get ∼4.5 years of postseismic ground surface displacements after the mainshock (Figure 6.1). We utilized LiCSAR products (Lazecký et al., 2020), which are based on GAMMA software (Wegnüller et al., 2016) to derive over 1700 interferograms for ascending track T072A covering the period from November 17, 2017 to May 25, 2022. Then we employed LiCSBAS (Morishita et al., 2020), an open-source time-series analysis package integrated with LiCSAR, to perform multitemporal interferometry analysis based on the SBAS technique (Berardino et al., 2002). The reader is referred to Morishita et al. (2020) for more details and in-depth descriptions of the LiCSBAS system. For descending track T079D, we manually processed Sentinel-1 data from November 18, 2017 to December 15, 2021 using GAMMA software, to generate over 560 interferograms. Each interferogram is processed at a spatial resolution of ∼30 m, and we used the 30-m DEM from SRTM mission to remove topographic effect (Farr et al., 2007). GACOS products (Yu et al., 2018) are additionally used to mitigate atmospheric delay for each interferometric pair. Then we imported the interferograms of T079D to

LiCSBAS to perform time series analysis. The network of small-baseline interferograms is shown in Figure 6.2. After reducing orbit ramps, topography-correlated components and performing spatio-temporal filters, we finally obtained ~4.5-year of cumulative postseismic LOS displacements from the two descending and ascending tracks of T072A and T079D, respectively (Figure 6.1c and 6.1d).

6.2.2 2.5D Postseismic Deformation Fields and Time Series Fitting

The postseismic 2.5D (quasi-eastward and quasi-upward) deformation fields are decomposed from the LOS displacements of the two ascending and descending tracks (Fujiwara et al., 2000; Motagh et al., 2017), which well define the westward crustal shortening along the northwestern foreland boundary of the Lurestan Arc and topography uplift west of the MFF (Figure 6.1e and 6.3).

In addition, we examine the InSAR displacement time series and utilize logarithmic $u(t) = a + b \cdot \ln(1 + t/\tau_{ln})$, exponential $u(t) = a + b \cdot \exp^{-t/\tau_{exp}}$ and combined function models $u(t) = a + b \cdot \ln(1 + t/\tau_{ln}) + d \cdot \exp^{-t/\tau_{exp}}$ to fit them (Figure 6.4 and 6.5). In these equations, t is time since the mainshock, $u(t)$ is the position of the point at the time t, a is a constant, b and d is the amplitude associated with the decay, and τ_{ln} and τ_{exp} are the logarithmic and exponential decay time, respectively. We employ least squares fitting to estimate these parameters for achieving the best fit to the time series data. The postseismic velocities for every point are given by the combined fitting function. We find that the postseismic velocities for most points remain below 5 mm/yr 4 years after the mainshock and are still decaying (Figure 6.4 and 6.5), indicating the majority of coseismic stress changes on the fault may have been released.

6.3 Finite Element Method Models

6.3.1 Full Afterslip Model

In last chapter, we modeled the 3-year afterslip evolution following 2017 Sarpol-e Zahab event to explore the fault friction properties using rate-strengthening friction law (Guo et al., 2022). However, due to the large number of adjustable parameters involved in the dynamic simulations and the trade-offs between them (e.g., Guo et al., 2022; Helmstetter and Shaw, 2009), here we employ full frictional afterlip simulations to infer the possible complexity of the fault structures and the frictional properties on them (see Section 3.3.3.3):

$$\Delta\tau = \mu_0 \cdot \Delta\sigma + \Delta\mu \cdot (\rho g h \cos\theta + \Delta\sigma) \tag{6.1}$$

where ρ is the density of the material, g is the gravitational acceleration (9.80665 m/s^2), h is the fault depth and θ is the fault dip angle. In this study, we specify $\mu_0 = 0.6$ (Byerlee, 1978). $\Delta\mu$ does not involve the rate-and-state friction law and is independent of slip rate, thus we refer to such models as “full” afterslip models.

In this chapter, an assumption in this scenario is that the mechanically full afterslip would relax the coseismic stress changes within 4.5 years. This assumption appears reasonable, particularly considering the short afterslip duration updip of the coseismic ruptures where the faults are usually locked during the interseismic period (Lienkaemper and McFarland, 2017; Tian et al., 2020). Subsequently, we compare the numerical simulations

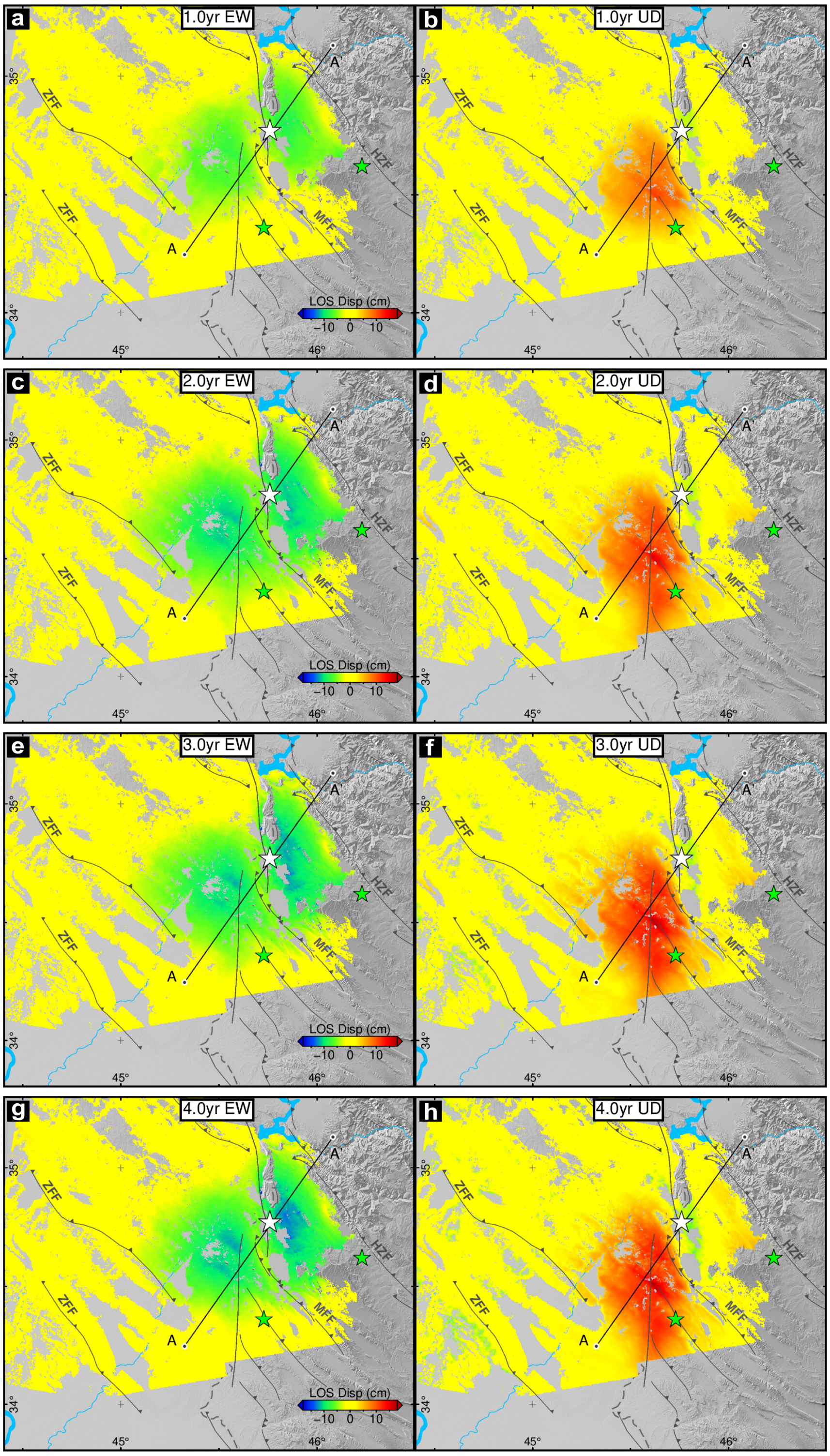

Figure 6.3: The 2.5D deformation (quasi-eastward (EW), eastward movement is positive; and quasi-upward (UD), upward movement is positive) fields 1 to 4 years after the mainshock decomposed from ascending Track T072A and descending Track T079D. The white and green stars are the mainshock and the two ~M 6 aftershocks respectively.

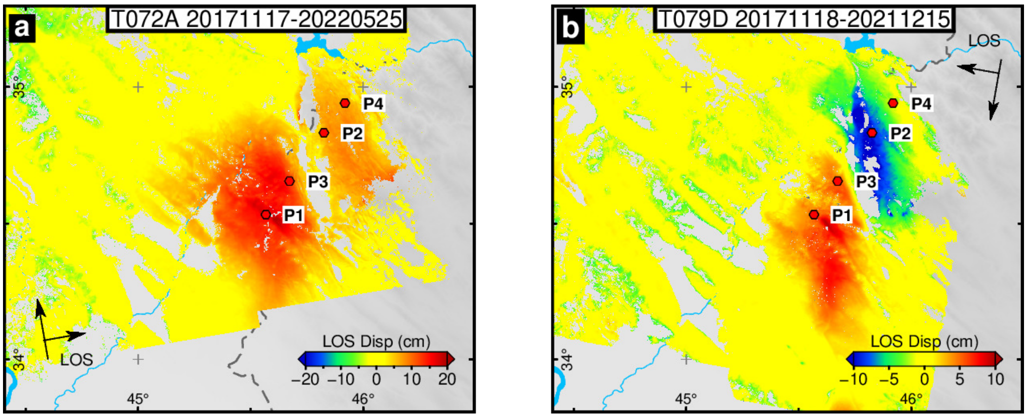

Figure 6.4: The selected points of (a) T072A and (b) T079D along Profile AA', which are used for plotting the InSAR time series in Figure 6.5.

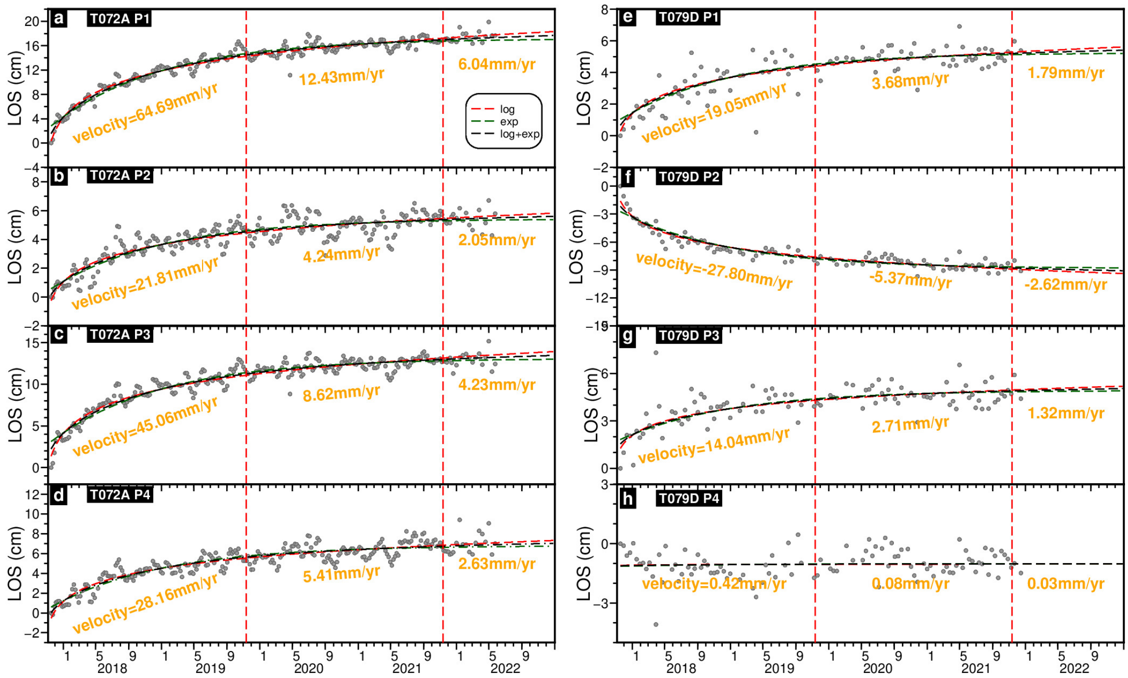

Figure 6.5: The time series of selected points for (a) T072A and (b) T079D shown in Figure 6.4. The red, green and black dashed lines are the fitting functions of logarithmic function, exponential function and the combination of the logarithmic exponential functions, respectively.

from various afterslip models incorporating three clusters of faults with the 4.5-year post-seismic InSAR observations within 8 km-wide swath AA' (Figure 6.1c and d) to explore the optimal fault structure and its frictional properties.

6.3.2 Model Setups

Hundreds of different 2D FEM models incorporating planar, ramp-flat faults and the combination models of ramp-flat and splay faults are established for the numerical simulations in this chapter. In order to minimize the boundary effect, our model meshes are expanded to 1520 km in horizontal direction and 500 km in depth direction (Figure 6.6), which is significantly larger than the source dimension of the Sarpol-e Zahab earthquake. For the east, west and bottom boundaries of the problem domain we fix the displacements normal to the boundaries (free slip boundary condition), while the top of the problem domain could move freely to all directions (free surface boundary condition). The minimum edge length of the meshes is about 1 km around the fault and top surface, and discretization size of the triangle elements gradually gets coarser far from the fault and ground surface, reaching to tens of kilometers near the boundaries. The material properties used in the FEM models are derived from previous references (Table 6.1, Afsari et al., 2011; Hatzfeld et al., 2003; Maheri-Peyrov et al., 2020; Mahmoodabadi et al., 2019; Motaghi et al., 2017; Teknik et al., 2019). In this study, we consider the 2D models as elastic bodies.

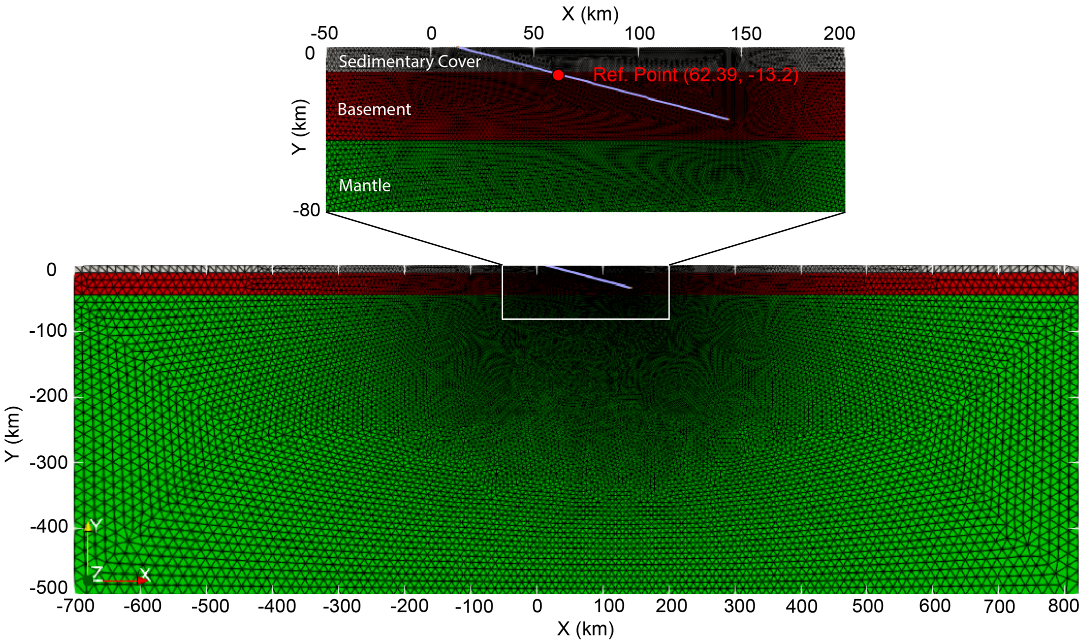

Figure 6.6: An example of a 2D mesh showing a planar fault dipping 15°, with the mesh coordinates of reference point (62.39 km, -13.2 km). The reference point in this mesh is horizontally moved 7.5 km to the left (west) from the original reference point (69.89 km, -13.2 km).

6.3.3 Model Approach and Results

Previous studies suggest the 2017 Sarpol-e Zahab earthquake ruptured a dextral-thrust fault with a rake angle (fault slip direction) of ~140° (e.g., Barnhart et al., 2018; Feng

Table 6.1: Material properties used in the simulations of this study and from Crust 1.0.

		Depth (km)	Density (kg/m^3)	V_p (km/s)	V_s (km/s)	Poisson ratio
Crust	Sedimentary Cover	12	2500 (2720^a)	5.4 (6.1^a)	3.1 (3.5^a)	0.25 (0.25^a)
	Crystalline Basement	45	2850 (2865^a)	6.2 (6.7^a)	3.5 (3.8^a)	0.27 (0.26^a)
Mantle		>45	3300 (3310^a)	8.2 (8.0^a)	4.4 (4.5^a)	0.30 (0.27^a)

[a]The material properties provided by Crust 1.0 (Laske et al., 2013) for comparison purposes.

et al., 2018; Guo et al., 2022; Wang and Bürgmann, 2020). To take the strike- and thrust-slip components into consideration, we thus select the Profile AA' along the rake angle of 140° to solve the FEM models (Figure 6.1a-b). To simulate the frictional afterslip along the Profile AA', we develop a suite of 2D FEM models incorporating planar faults (e.g., Feng et al., 2018; Liu and Xu, 2019), ramp-flat faults (e.g., Barnhart et al., 2018; Guo et al., 2022; Wang and Bürgmann, 2020) and combined models of the ramp-flat and splay faults (Tavani et al., 2018, 2020) with the open-source code PyLith (Aagaard et al., 2013). Based on these various fault structures, we firstly invert the coseismic InSAR data calculated from last chapter (Guo et al., 2022) for the kinematic coseismic models (see Section 6.3.3.1). We then solve the forward models using the coseismic slip distributions, and finally we import the coseismic stress changes from the forward models into the frictional afterslip simulations.

To do so, we employ a modeling strategy consisting of three main steps. We firstly test a number of 2D FEM models that integrate different planar fault geometries to explore the best coseismic kinematic model and its corresponding frictional afterslip model (Section 6.3.3.1). Then, we introduce a series of ramp-flat faults into the frictional afterslip models by modifying the geometry of the best planar fault derived by the last step. These adjustments include variations in the transition depth between the updip flat and downdip ramp, and the dip angles of the flat. Given previous studies suggest that the coseismic rupture mainly occured on the "ramp", while postseismic slip primarily on the "flat", we focus on using postseismic data to search for ramp-flat geometry in this study (Section 6.3.3.2). Finally, we add another splay fault to the best ramp-flat model from the second step and vary the dip angles and rooting depths of the splay faults to construct the composite models for the frictional afterslip simulations (Section 6.3.3.3). As such, by gradually increasing the complexity of the fault models, we progressively explore whether the model complexities and the frictional properties on them could further improve the data fitting.

To determine the frictional properties on different fault structures in the frictional afterslip simulations, a series of $\Delta\mu$ values from 1×10^{-5} to 1×10^{-2} are imposed on the different parts of the fault models. A section of the fault model (coseismic asperity) is clamped (no sliding) by imposing a higher friction based on the coseismic slip distribution, which usually would heal and get relocked in the real earthquake cycle. Lower effective friction coefficients are imposed to the areas updip and downdip of the coseismic rupture as well as to the splay faults to make sure aseismic slip occurring on these segments. For simplicity and also because the viscoelastic relaxation is negligible for postseismic transient of this event (e.g. Guo et al., 2022; Wang and Bürgmann, 2020), here we consider all of the 2D models as elastic bodies (we will discuss the viscoelastic effect in the Section 6.4).

6.3.3.1 Planar Models

We firstly constructed a suite of model meshes incorporating planar faults for the coseismic inversions. Because the fault geometry and fault position are significant for modeling surface deformation, we get an initial planar fault along Profile AA' based on the fault model proposed in last chapter (Guo et al., 2022), which is in a good agreement with the results from others (e.g., Feng et al., 2018; Wang and Bürgmann, 2020). A reference point on the initial fault with mesh coordinates (x, y) = (69.89 km, −13.2 km) (Figure 6.6) is defined so that a number of 2D models with different planar fault geometries could be constructed by horizontally moving the reference point (from -20 km to 10 km, eastward is positive) and changing the dip angles (from 7° to 19°). Then based on these model meshes, we invert the observed coseismic surface motions for the best coseismic kinematic model.

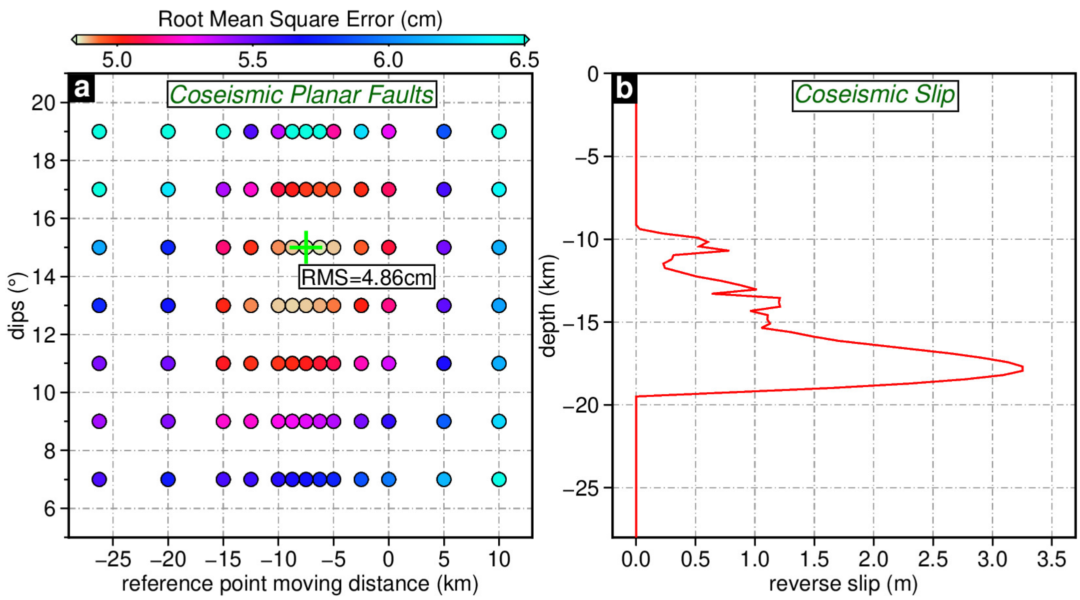

Figure 6.7: Searching results of planar fault geometry for coseismic kinematic models. The green plus sign indicates the best planar fault for coseismic deformation. The reference point on the initial fault derived from last chapter (Guo et al., 2022) with mesh coordinates (x, y) = (69.89 km, −13.2 km) is defined. (b) is the coseismic fault slip along depth.

We use a 2D elastic dislocation model in a layered FEM model to invert the observed surface motions to derive a coseismic kinematic model. The geodetic Green's functions are calculated using PyLith software for coseismic inversions. The fault slip is constrained as reverse slip and then we invert the coseismic InSAR data from Guo et al. (2022) for the kinematic coseismic models, based on the linear least-squares inversions with bounds on the variable. The optimal smooth factors for the models are selected based on the trade-off between misfit of observations and simulations and fault roughness. Then we evaluate a series of forward models to achieve a best fit to the coseismic data. The results show that the parameters of the best-fitting planar coseismic model with dip angle of 15° and the peak coseismic slip of 3.3 m and depth range of 10-20 km are consistent with those given by previous works (Figure 6.7 and 6.8; Barnhart et al., 2018; Guo et al., 2022; Wang and Bürgmann, 2020).

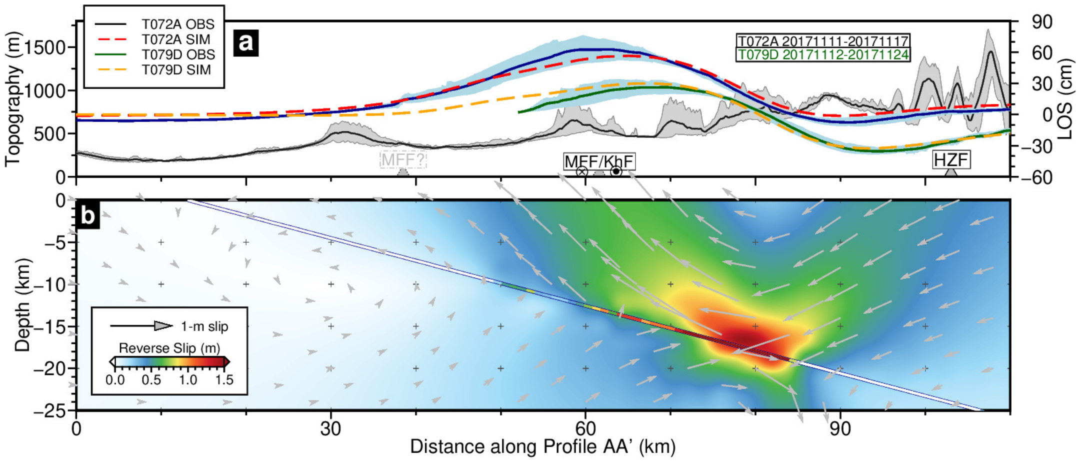

Figure 6.8: Kinematic models and simulations based on planar faults for coseismic deformation along profile the AA'. (a) coseismic InSAR observations and simulations based on the (b) coseismic slip model which is from the best searching result of Figure 6.7. The envelope curves of the InSAR observations and topography (gray) in (a) indicate the minimum, maximum and mean value of the swath with width of 8 km.

Based on this fault slip distribution model, we calculated the coseismic stress changes to drive frictionally full afterslip along the planar fault by varying the friction variations up- and down-dip of the coseismic rupture. As is shown in Figure 6.9a, the best value of friction strengthening updip of the coseismic rupture ($\Delta\mu_1 = \sim 0.002$) is significantly greater than that on the downdip part ($\Delta\mu_2 = \sim 0.0002$), which validates the friction contrast between the up- and down-dip portions of the fault as indicated by previous studies (Guo et al., 2022; Wang and Bürgmann, 2020). Such frictional contrast may be related to the lithology and the increasing temperatures and pressures due to the rising depth. Furthermore, the small values of the overall strengthening $\Delta\mu$ of the fault are expected. $\Delta\mu$ is equivalent to $a - b$ of purely rate-dependent friction law which is on the order of 10^{-4}-10^{-2} derived from both laboratory experiments and postseismic geodetic data (e.g., Barbot et al., 2009; Carpenter et al., 2012; Chang et al., 2013; Collettini et al., 2011; Ingleby et al., 2020; Johnson et al., 2006; Perfettini and Avouac, 2007). The inferred planar afterslip model with a RMS error of 2.28 cm indicates that there is ~0.7 m and ~0.1-0.2 m peak afterslip up- and down-dip of the coseismic rupture, respectively. However, such a planar afterslip model cannot explain long-wavelength deformation field in its entirety as the western postseismic signals extend further to the west (Figure 6.10a and 6.10b).

6.3.3.2 Ramp-flat Models

Then, we attempt to investigate the optimal afterslip models using ramp-flat faults. Based on the best planar fault model derived in Section 6.3.3.1, we vary the transition depths between the updip flat and downdip ramp, as well as the dip angles of the updip flat to

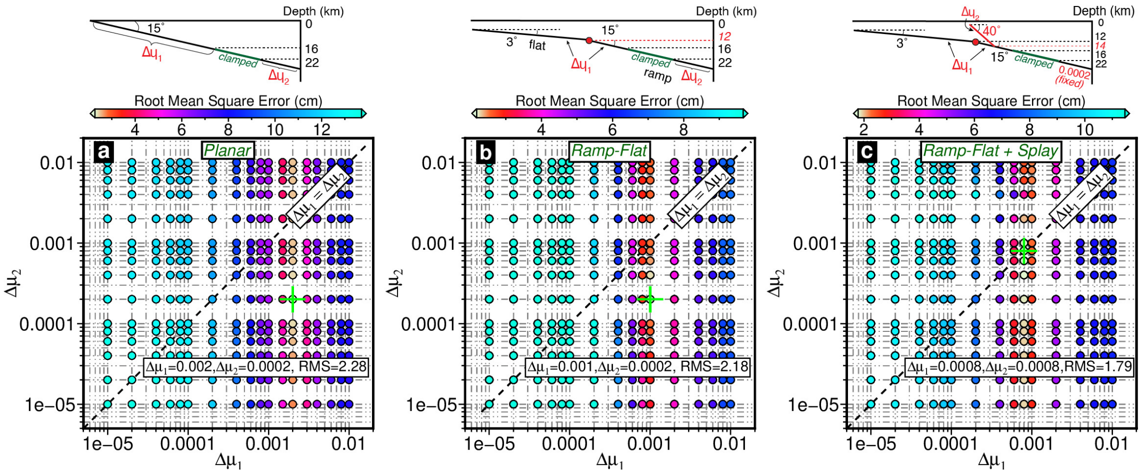

Figure 6.9: Optimal frictional strengthening search results for various best-constrained faults: (a) a planar fault, (b) a ramp-flat fault and (c) composite model with splay and ramp-flat faults. The green plus signs denote the best search results described in the white background text box.

establish a suite of ramp-flat fault models. There are two steps to do it. In the first step, we fixed the updip flat and downdip ramp part with a dip angle of 3° and 15° according to previous studies (Barnhart et al., 2018; Guo et al., 2022; Wang and Bürgmann, 2020) and the best coseismic model, respectively, but vary the transition depths between the updip flat and downdip ramp from 8 km to 16 km (Figure 6.11a). In the second step we fix the transition depth at the optimal depth (12 km) derived from the first step and keep fixing the dip angle of the downdip ramp at 15°, but we vary the dip angle of the updip flat from 0 to 12° to create a range of ramp-flat fault models (Figure 6.11b). Then the ramp-flat faults are used for investigating the best mechanically full afterslip model.

By searching the friction variations up- ($\Delta\mu_1$) and down-dip ($\Delta\mu_2$) of the coseismic rupture, the ramp-flat fault in which the transition depth and dip angle of the updip flat are 12 km and 3°, respectively, proved successful in explaining the postseismic surface motion (Figure 6.9b and Figure 6.11). The best ramp-flat afterslip model with the maximum slip of ~1.0 m and ~0.2 m up- and down-dip of the coseismic rupture indicates friction variation of $\Delta\mu_1 =\sim 0.001$, $\Delta\mu_2 =\sim 0.0002$ for the up- and downdip segments, respectively (Figure 6.9b and 6.10c). Compared to the planar fault model shown in Figure 6.9a and 6.10b, such a model offers an overall improvement in explaining surface displacements with a RMS error of 2.18 cm (Figure 6.9b and 6.10c).

6.3.3.3 Splay Models

Finally, based on the best ramp-flat fault derived above, we add another splay fault to it and thus we get the combined models of ramp-flat and splay faults. We fix the geometry of the best-fitting ramp-flat fault but change the dip angles and rooting depths of the splay faults to check whether such structures could further improve the residuals between the postseismic observations and simulations, compared to the best-fitting ramp-flat fault.

We fix the frictional variation of the downdip portion of the ramp-flat fault to 0.0002 to test various composite models of splay and ramp-flat faults. By varying the dip angles from 25° to 75° and rooting depths from 12 to 15 km for the splay faults, we search for

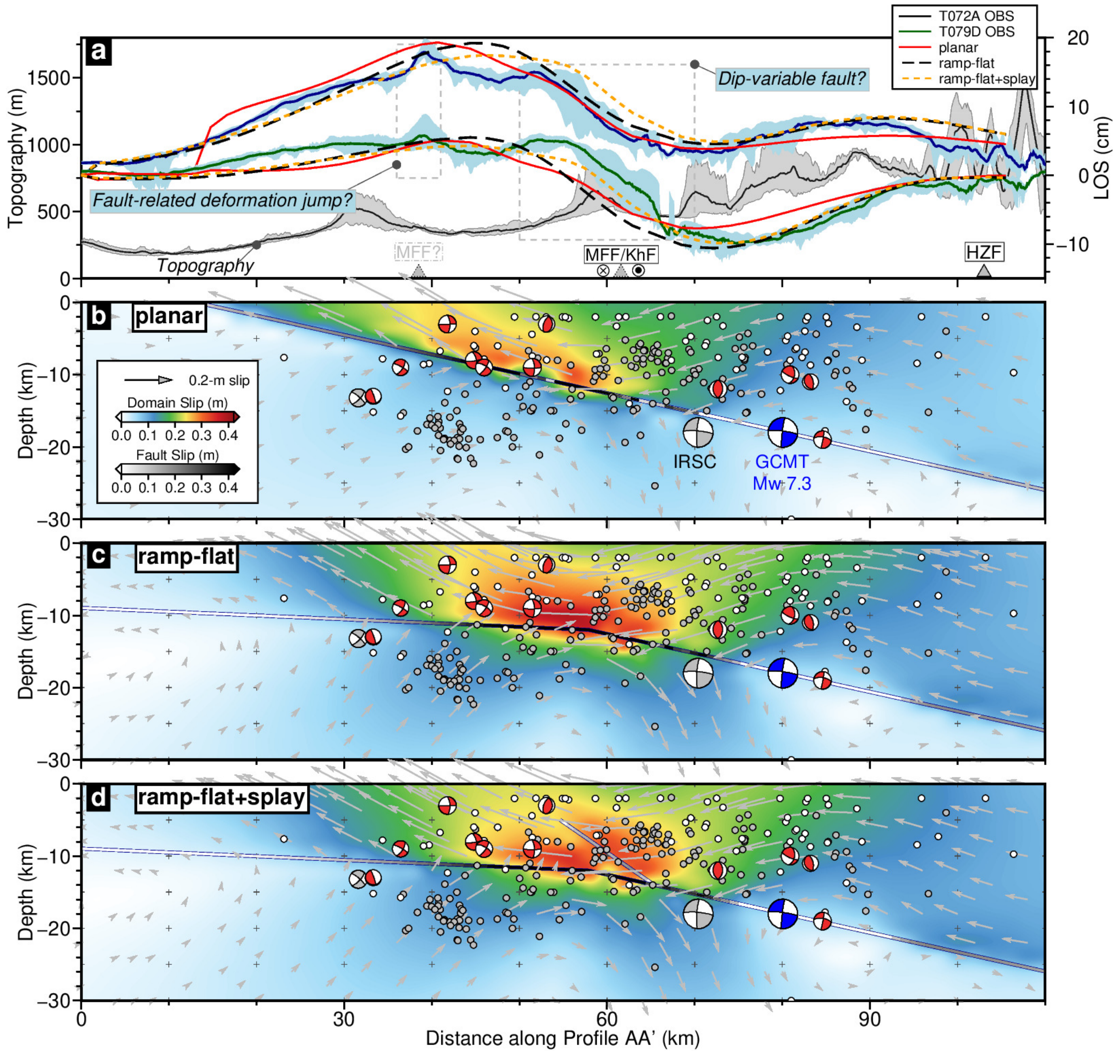

Figure 6.10: Postseismic InSAR observations (~4.5 years after the mainshock) and different mechanical afterslip models. (a) Comparison between InSAR observations and the model simulations based on (b) the best planar fault model, (c) the best ramp-flat fault model and (d) the best composite model of a ramp-flat and a splay fault. The mechanical models are based on the search results presented in Figure 6.9. The envelope curves of the InSAR observations in (a) indicate the minimum, maximum and mean value of the swath with width of 8 km. The gray and white dots are the relocated aftershocks from Fathian et al. (2021) within approximately 2 months and Jamalreyhani et al. (2022) with $M \geq 3$. The gray, blue and red beach balls are the focal mechanisms from the IRSC, GCMT catalog and Jamalreyhani et al. (2022), respectively. HZF: High Zagros Fault; MFF: Mountain Front Fault; KhF: Khanaqin fault.

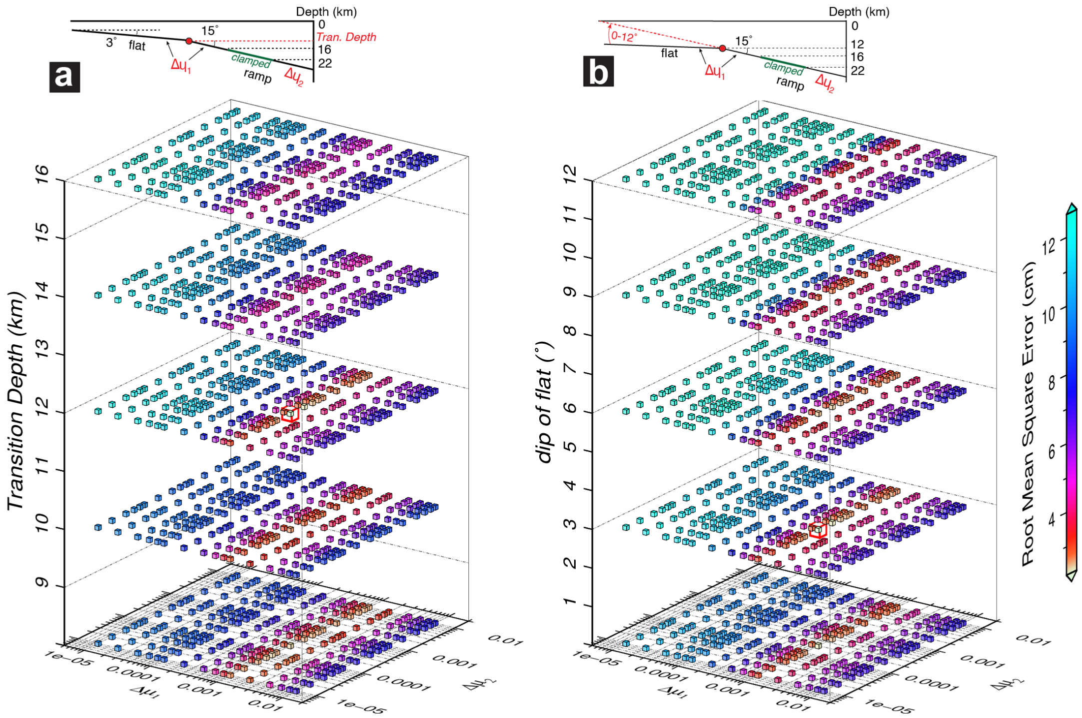

Figure 6.11: (a) Searching results between transition depths and the friction coefficients up- and down-dip of coseismic rupture, based on ramp-flat faults. The red cube indicates the best result (with RMS error of 2.18 cm) in which $\Delta\mu_1 = 0.001$, $\Delta\mu_2 = 0.0002$ for the up- and downdip segments of the fault, respectively, the transition depth between the up- and down-dip portions is 12 km. (b) Searching results between dip angles of flat portion and the friction coefficients up- and down-dip of coseismic rupture, based on ramp-flat faults. The red cube indicates the best result (with RMS error of 2.18 cm) in which $\Delta\mu_1 = 0.001$, $\Delta\mu_2 = 0.0002$ for the up- and downdip segments of the fault, respectively, the dip angle of the updip flat is 3°.

the optimal frictional variations on the updip part of the ramp-flat faults and the splay faults (Figure 6.12 and 6.13). Our findings indicate that a splay fault with a dip angle of 40° and a rooting depth of 14 km provides the best fit to the InSAR observations, with a RMS error of 1.79 cm, and the frictional variation for both the ramp-flat and splay fault of ∼0.0008 (Figure 6.9c and 6.13a). However, it is noteworthy that the maximum frictional slip on the splay fault (∼0.2 m) is considerably smaller than that (∼0.9 m) on the updip portion of the ramp-flat fault, which may be due to the higher dip angle of the splay structure making it difficult to produce thrust slip. Such a minor slip might also be the reason why most geodetically-constrained models are not sensitive to it, leading to the preference for ramp-flat faults in previous studies (Barnhart et al., 2018; Guo et al., 2022; Wang and Bürgmann, 2020). With changes in rooting depths and dip angles of the splay fault, the friction variations on it vary accordingly, suggesting a trade-off between the splay fault geometries and the friction variations on them (Figure 6.12, 6.13 and Table 6.2). Overall, comparing all the mechanical afterslip model solutions based on the integration fault structures of ramp-flat and splay faults, it becomes apparent that they consistently yield better residuals than the planar and ramp-flat fault models (Table 6.2).

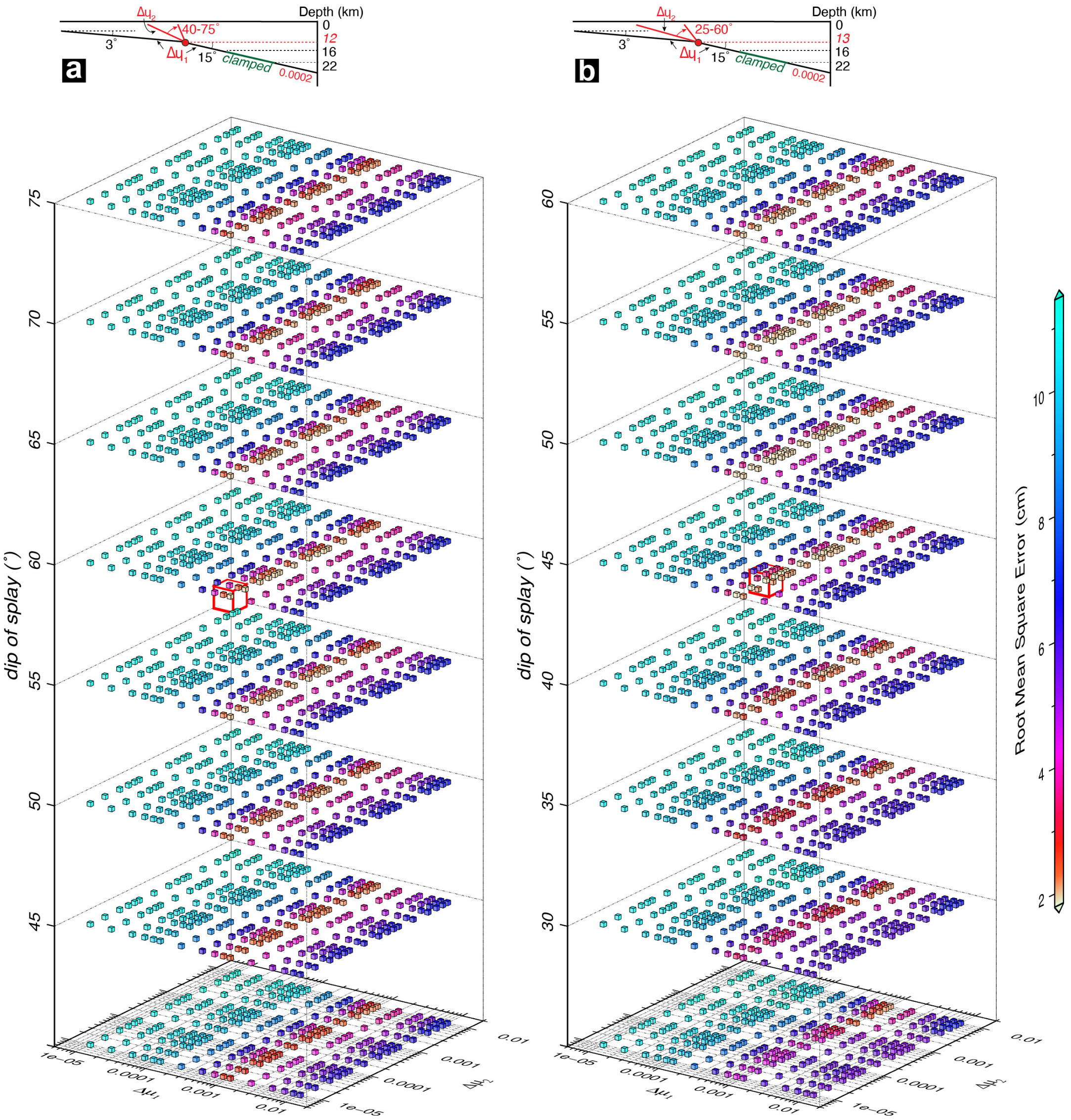

Figure 6.12: Searching results between dip angles of splay fault and the friction coefficients of the updip flat and the splay fault. The rooting depths of the splay faults are (a) 12 km and (b) 13 km, respectively. The red cubes indicate the best searching results. The best results for (a) are $\Delta\mu_1 = 0.001$, $\Delta\mu_2 = 0.00001$ and the RMS error of 1.93 cm with a splay fault dipping 60°; for (b) are $\Delta\mu_1 = 0.0008$, $\Delta\mu_2 = 0.00004$ and the RMS error of 1.88 cm with a splay fault dipping 45°.

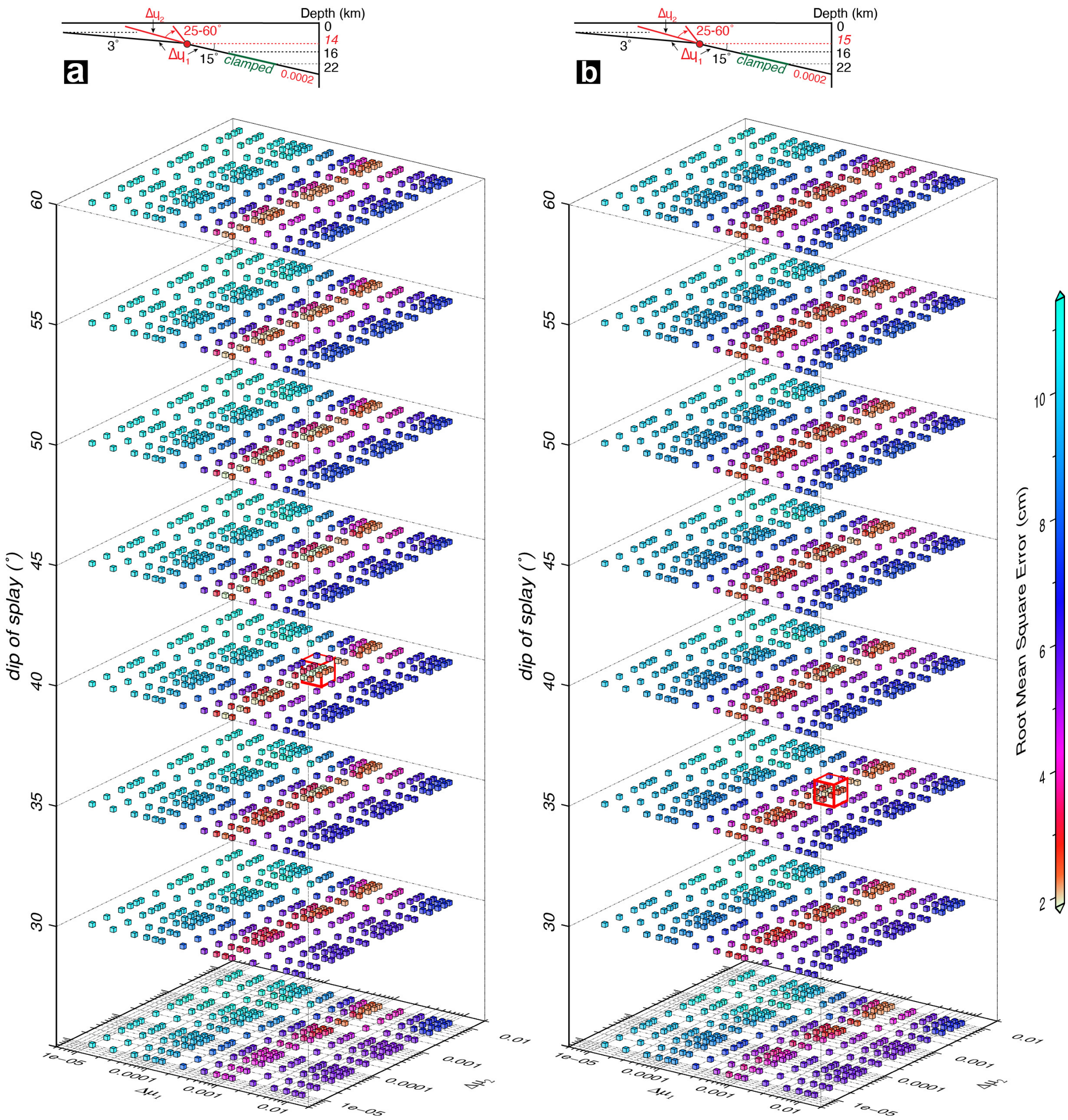

Figure 6.13: Same to Figure 6.12 but the rooting depths of the splay faults are (a) 14 km and (b) 15 km, respectively. The red cubes indicate the best searching results. The best results for (a) are $\Delta\mu_1 = 0.0008$, $\Delta\mu_2 = 0.0008$ and the RMS error of 1.79 cm with a splay fault dipping 40°; for (b) are $\Delta\mu_1 = 0.0008$, $\Delta\mu_2 = 0.001$ and the RMS error of 1.81 cm with a splay fault dipping 35°.

Table 6.2: Best searching results of frictional variations based on different fault geometries.

	Frictional Afterslip Models			
	Scenarios	$\Delta\mu_1$	$\Delta\mu_2$	RMS (cm)
Planar Models	Figure 6.9a	0.002	0.0002	2.28
	Figure 6.17a	0.002	0.006	2.18
Ramp-flat Models	Figure 6.9b, 6.11	0.001	0.0002	2.18
	Figure 6.17b	0.001	0.002	2.12
Ramp-flat and Splay Models	Figure 6.12a	0.001	0.00001	1.93
	Figure 6.12b	0.0008	0.00004	1.88
	Figure 6.9c, 6.13a	0.0008	0.0008	1.79
	Figure 6.13b	0.0008	0.001	1.81

6.4 Discussion

6.4.1 The Impact of Viscoelastic Effect, Data Noise, and Medium Parameters on the Models

We conduct further assessments to validate the influence of viscoelastic responses, data noise, as well as medium parameters on the frictional afterslip models. In this study, we have assumed the viscoelastic relaxation is negligible, as suggested by previous studies (e.g., Barnhart et al., 2018; Guo et al., 2022; Wang and Bürgmann, 2020), where the viscosity in this seismogenic zone is expected to be no less than 1×10^{19} Pa S, and the resulting displacements magnitudes are negligible compared to the cumulative postseismic deformation. Here, we take the ramp-flat fault as an example to quantitatively evaluate the contribution of viscoelastic deformation to surface deformation and our afterslip model. We tested Maxwell viscosity of 1×10^{19} and 1×10^{20} Pa S in the lower crust between 25 km and 45 km underlain by a Maxwell-fluid upper mantle with an effective viscosity of 3×10^{19} Pa S to explore the viscoelastic contribution (Guo et al., 2022; Lv et al., 2020; Wang and Bürgmann, 2020). The results show that the maximum viscoelastic contribution (with Maxwell viscosity of 1×10^{19} Pa S) $\sim$4.5 years after Sarpol-e Zahab event is less than 2 cm, one tenth of cumulative LOS deformation in this period (Figure 6.14a-b). The viscoelastic responses with a viscosity of 1×10^{20} Pa S is even smaller (Figure 6.14c-d). Thus, it is probably reasonable to neglect the viscoelastic response in this study.

In addition to the viscoelastic relaxation, InSAR observation noise, crustal properties and base frictions μ_0 used in the simulations may also have an impact on our frictional afterslip models. We masked the main deformation area from the $\sim$1-year observations of ascending (T072A) and descending (T079D) tracks and compared the noise levels between this study and Wang and Bürgmann (2020). The results indicate that the noise levels of both studies are comparable (Figure 6.15). Then we apply noise perturbations to the original InSAR observations and use them to re-search the frictional afterslip models with different fault geometries (i.e., planar, ramp-flat and combined model of ramp-flat and splay faults shown in Figure 6.9). We find that, although the observation noise could lead to slight variations in friction $\Delta\mu_1$ and $\Delta\mu_2$, the combined model of ramp-flat and splay faults could better explain the data (Table 6.3). Similarly, we apply different crustal properties and base frictions in the modeling and the similar conclusion can be drawn (Table 6.3).

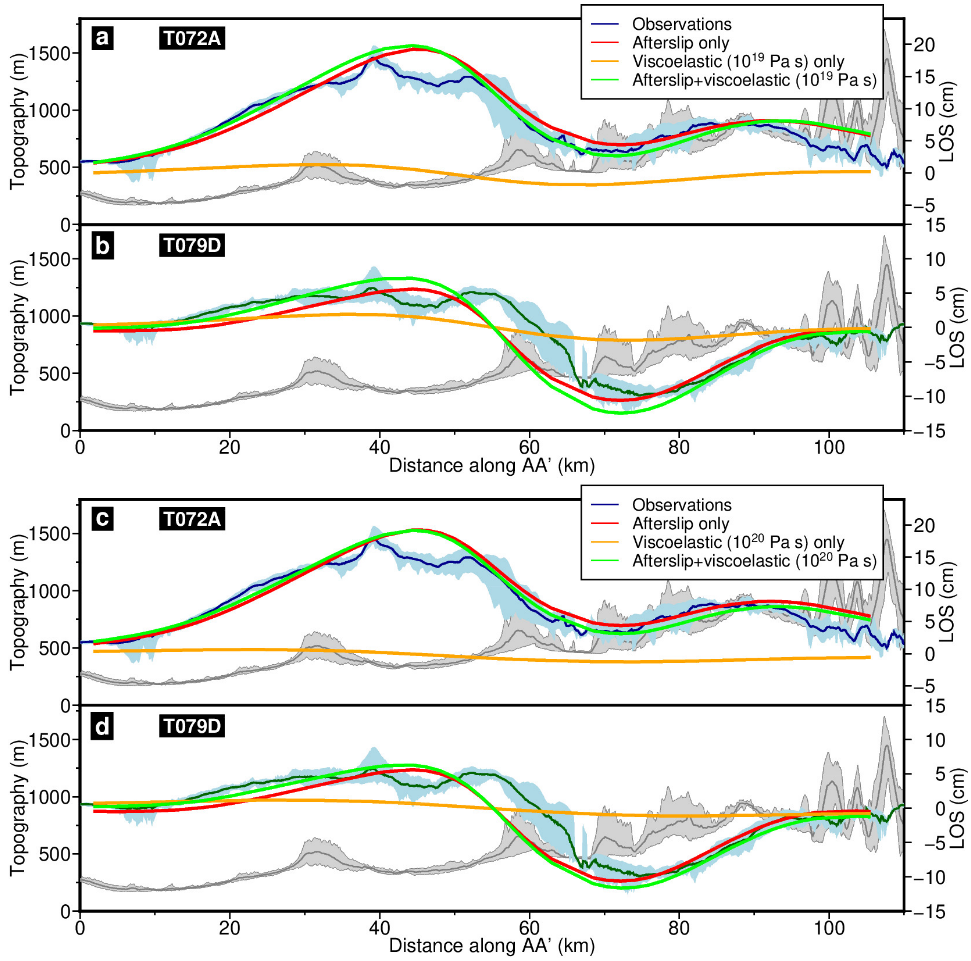

Figure 6.14: The comparisons between InSAR observations, afterslip and viscoelastic simulations. Different viscosities 1×10^{19} (a and b) and 1×10^{20} Pa S (c and d) between 25-45 km in the lower crust are tested based on the ramp-flat fault.

6.4.2 Insights from Relocated Aftershocks and Geologic Cross-Sections

Our findings suggest that a composite model, comprising both ramp-flat and splay faults, offers a more plausible explanation for the postseismic InSAR observations after the 2017 Sarpol-e Zahab mainshock. This structural geometry is consistent with the distribution of relocated aftershocks and geologic cross-sections. The 2017 Sarpol-e Zahab event is a basement-rooted faulting while most of the aftershocks are relocated at the sedimentary cover with shallow centroid depth of 8-12 km (Jamalreyhani et al., 2022). This indicates special fault interactions between basement and sedimentary cover (Figure 6.16a-c). In addition, the geologic cross-sections in previous studies also reveal the structural complexity where the basement-rooted fault emerges from the basement into the sedimentary cover (Figure 6.16d; e.g., Alavi, 2007; Emami et al., 2010; Guo et al., 2022; Koshnaw et al., 2020; Le Garzic et al., 2019; McQuarrie, 2004; Sadeghi and Yassaghi, 2016; Tavani et al., 2018; Yang et al., 2019). Because the forelands of mountain belts usually develop listric faults with varying dip angles along depth, the splay fault in the combined model may be dip-variable rather than a simple planar fault (Figure 6.16d-e).

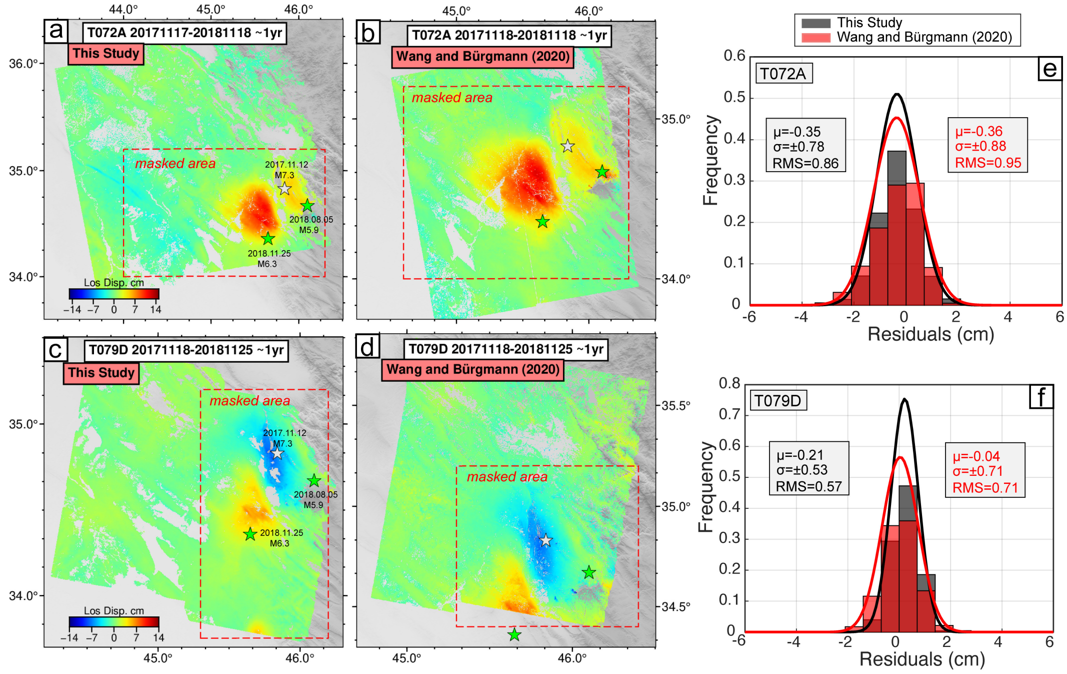

Figure 6.15: ~1-year cumulative postseismic LOS displacements of ascending track T072A (a and b) and descending track T079D (c and d) from our study and Wang and Bürgmann (2020). The red dashed boxes in (a-d) represent the masked areas with deformation fields. The residuals (e and f) are calculated from the non-deforming areas with T072A and T079D.

Table 6.3: The impact of data noises, material properties and base friction on model results.

	Frictional Afterslip Models[a]			
	Scenarios	$\Delta\mu_1$	$\Delta\mu_2$	RMS (cm)
Planar Models	Figure 6.9a	0.002	0.0002	2.28
	(a)	0.002	0.0002	2.29
	(b)	0.002	0.00008	2.46
	(c)	0.002	0.0001	2.29
	(d)	0.002	0.00008	2.31
Ramp-flat Models	Figure 6.9b	0.001	0.0002	2.18
	(a)	0.001	0.0004	2.33
	(b)	0.0008	0.0002	2.13
	(c)	0.0008	0.0002	2.17
	(d)	0.001	0.0002	2.02
Ramp-flat and Splay Models	Figure 6.9c	0.0008	0.0008	1.79
	(a)	0.0006	0.001	2.09
	(b)	0.0006	0.001	1.91
	(c)	0.0006	0.00006	1.98
	(d)	0.0008	0.0008	1.86

[a]Note: (a) Introducing noise disturbance to InSAR data. (b) crust material properties are from Crust 1.0 (Laske et al., 2013). (c) base friction $\mu_0 = 0.5$. (d) base friction $\mu_0 = 0.7$.

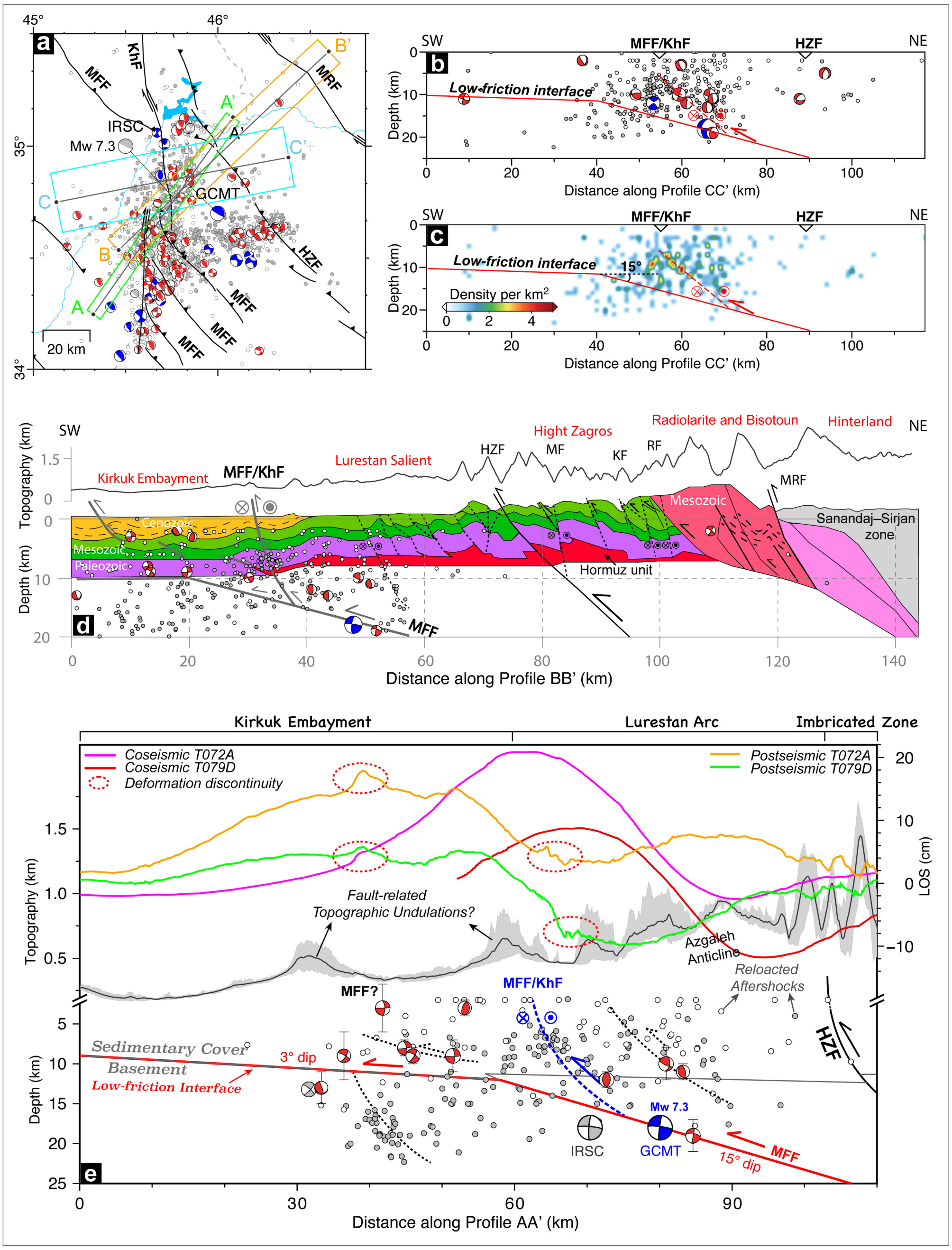

Figure 6.16: Relocated aftershocks, structural cross-section as well as the conceptual fault structures along various profiles in the seismogenic zone. (a) Tectonic map showing the relocated aftershock distributions, faults, as well as the three profiles. The swath widths along Profile AA', BB' and CC' are 8 km,16 km and 30 km, respectively. The gray dots represent the relocated aftershocks from Fathian et al. (2021) and Jamalreyhani et al. (2022), respectively. The gray, blue and red beach balls are the focal mechanisms from the IRSC, GCMT catalog and Jamalreyhani et al. (2022), respectively. (b) and (c) are the distribution and the density map of relocated aftershocks of Profile CC' along depth, respectively. (d) shows the relocated aftershocks and geologic cross section which is modified from Yang et al. (2018) along Profile BB'. (e) represents the relationship between the topography, seismicity, surface deformation and the regional conceptual interpreted fault structures. The magenta and dark red solid lines indicate the coseismic LOS displacements derived from our previous work (Guo et al., 2022), scaled by a factor of 3. The dashed lines are the conceptual faults. HZF: High Zagros Fault; KF: Kermanshah Fault; MRF: Main Recent Fault; MF: Marekhil Fault; RF: Ravansar Fault; KhF: Khanaqin Fault.

The relationship between the seismogenic fault of this 2017 Mw 7.3 event and the blind MFF fault remains controversial in previous studies (Barnhart et al., 2018; Basilici et al., 2020; Chen et al., 2018; Fathian et al., 2021; Feng et al., 2018; Guo et al., 2022; Nissen et al., 2019; Tavani et al., 2018; Wang and Bürgmann, 2020). The balanced cross-section constrained by geologic observations, seismic reflection data and well data suggests that this 2017 event ruptured the MFF (Tavani et al., 2018), which is in good agreement with the composite model of ramp-flat and splay faults in this study (Figure 6.16).

Furthermore, the strike angle (355°) of the seismogenic fault of this Sarpol-e Zahab event closely aligns with the nearly north-south trending Khanaqin fault (Figure 6.1 and Figure 6.16). Because of the variability in the naming conventions of basement faults, the strike-slip Khanaqin fault could be regarded as a segment of the blind MFF (Berberian, 1995) and it displaces the MFF laterally to the right for a distance of at least 130 km (Hessami et al., 2001).

Additionally, because the strain partitioning in this region (Talebian and Jackson, 2004), the collision of the Arabian and Eurasian plates promotes oblique motion (dextral-thrust) along the fault, which explains the slip direction (rake angle of ∼140°) of the Mw 7.3 main-shock (Gombert et al., 2019). Therefore the MFF and/or the Khanaqin fault features a combination of reverse and right-lateral strike-slip mechanisms, rather than predominantly exhibiting either thrust- or strike-slip, respectively (Figure 6.16; Berberian, 1995; Hessami et al., 2001).

Overall, the 2017 Mw 7.3 basement-involved event activated a complex structure in this region, contributing regional thick- and thin-skinned shortening in seismic and aseismic behaviors, respectively. Such a fault interaction pattern is more complex than a simple two-layer decoupling model. In the two-layer decoupling model, a mechanically weak layer (Hormuz unit) impedes the propagation of seismic events from the basement to the sedimentary cover and limits most earthquake to $M < 6$ (e.g., Alavi, 2007; Barnhart et al., 2018; Nissen et al., 2011; Wang and Bürgmann, 2020). The destructive 2017 Mw 7.3 Sarpol-e Zahab event thus serves as a significant warning that the MFF has the capacity to host significant ($M > 7$) earthquakes and underscores the need for a reevaluation of the seismic potential of these regional faults.

6.4.3 Fault Frictional Heterogeneity VS Structural Complexity

In addition to the structural complexity of the 2017 Sarpol-e Zahab event, we find a friction contrast between the up- and down-dip portions ($\Delta\mu_1$ and $\Delta\mu_2$) of the planar and ramp-flat faults (Figure 6.9a-b). However, the values of the frictional parameters may be even more complex because they may vary with the lithology (Floyd et al., 2016; Yassaghi and Marone, 2019). The mechanical stratigraphy in the region of the 2017 Sarpol-e Zahab event consists of different lithologies at various depths ranging from the Cambrian to Triassic (e.g., Casciello et al., 2009; Le Garzic et al., 2019; Sadeghi and Yassaghi, 2016), which may significantly influence the friction properties of the fault plane. To explore the impact of the frictional complexity of the fault on the afterslip modeling, we divide the planar fault and ramp-flat fault shown in Figure 6.9a-b and Figure 6.10b-c into 3 segments. Then the friction of the downdip portion of the faults was set to 0.0002, the best search result in Figure 6.9, and finally we searched for the frictions on the other 2 segments updip of the coseismic rupture (Figure 6.17). The results show that the friction variations on the two updip segments are $\Delta\mu_1 =\sim 0.002$, $\Delta\mu_2 =\sim 0.006$ for the planar fault and $\Delta\mu_1 =\sim 0.001$, $\Delta\mu_2 =\sim 0.002$ for the ramp-flat fault, respectively (Figure

6.17). It is noteworthy that these models with more complex fault friction heterogeneity do not significantly improve the model's fit, nor do they provide a better explanation for the observations in comparison to the geometrically complex combined models (see Table 6.2).

In last chapter (Guo et al., 2022), we also explore the time-dependent afterslip evolution on a purely rate-strengthening ramp-flat fault. Similarly, we found that a more physically plausible stress-driven afterslip model which features depth-varying frictions is preferred, but the misfit still cannot be improved significantly. More interestingly, many previous studies employing rate- and state-dependent or steady-state rate-dependent friction laws have assumed either uniform (e.g., Barbot et al., 2009; Feng et al., 2016; Fukuda et al., 2009; Hearn et al., 2009; Wang and Fialko, 2018) or spatially varying frictions (e.g., Chang et al., 2013; Guo et al., 2022; Ingleby et al., 2020; Wang, 2018) along the fault to dynamically model afterslip, with general satisfactory results. To sum up, it appears that the contribution of the fault structures to the surface deformation is first-order compared to the fault friction heterogeneity (Table 6.2). Only through the precise fault morphology can we gain meaningful insights into fault friction properties, which, in turn, are crucial for our understanding of fault stress accumulation and seismic hazard assessment.

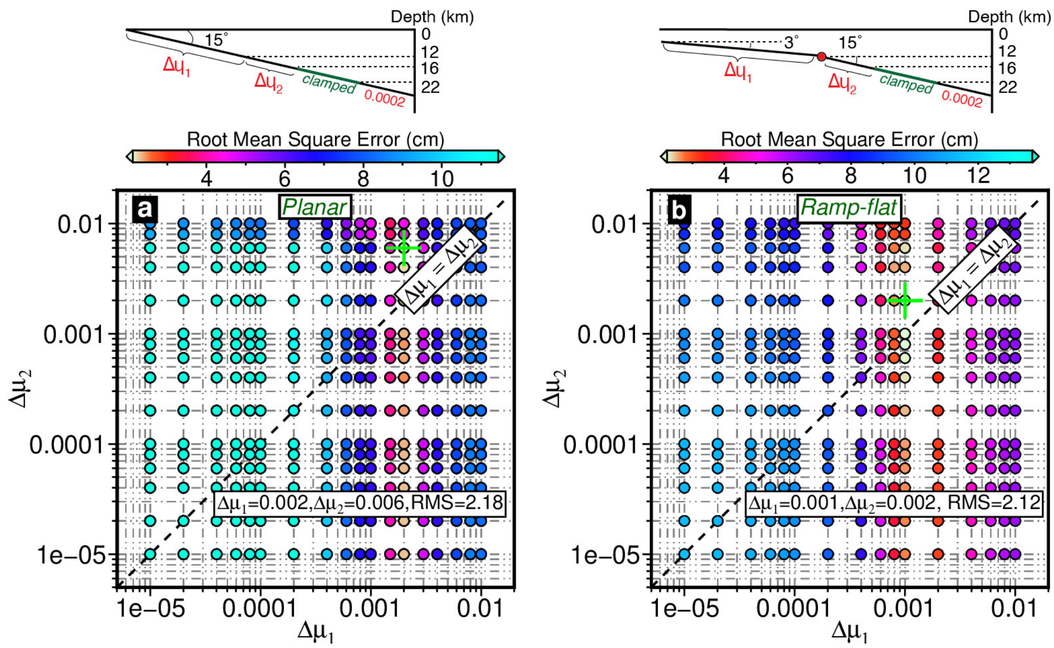

Figure 6.17: Searching results of friction heterogeneity based on the three-segment planar and ramp-flat faults in which the friction variation of the downdip portion is fixed as 0.0002. (a) planar fault and (b) ramp-flat fault. The green plus signs denote the best search results described in the white background text box.

6.4.4 Further Discussion: Structural Complexity Revealed by Large Events in Active Fold-and-Thrust Belts

Active continental fold-and-thrust belts have the potential to host large earthquakes (M > 7). However, due to the ongoing continental collision and orogeny in the mountain belts, the seismogenic structures of the thrust events in active fold-and-thrust belts are often the subject of considerable debate (e.g., Bendick et al., 2007; Dal Zilio et al., 2019; Ingleby et al., 2020; Lee et al., 2006; Li et al., 2018; Sathiakumar and Barbot, 2021; Yue et al., 2005). Other notable examples in fold-and-thrust belts since the late 20th century, which like the 2017 Mw 7.3 Sarpol-e Zahab event in the ZFTB of the Zagros Mountain, exhibit similar complexity in fault structures include the 1999 Mw 7.6 Chi-chi earthquake in the western foothills of central Taiwan, the 2005 Mw 7.6 Kashmir earthquake in the westernmost Himalaya, the 2015 Mw 7.8 Gorkha, Nepal earthquake in the Lesser Himalaya and the 2018 Mw 7.5 Papua New Guinea earthquake in the New Guinea Highlands. While some previous studies have suggested relatively simple single- or multi-segment planar or ramp-flat faults (e.g. Avouac et al., 2006; Feng et al., 2017; Hsu et al., 2002; Ji et al., 2001, 2003; Johnson et al., 2001; Johnson and Segall, 2004; Jouanne et al., 2011; Ma et al., 2000; Wang and Fialko, 2018, 2014; Wang et al., 2020; Xu et al., 2022; Zhao et al., 2017), all of these events occurring in the mountain ranges seem to exhibit more complex fault structures. For example, the activation of several interlinked faults for 1999 Chi-chi event (Yue et al., 2005), the wedge thrust faults for 2005 Kashmir earthquake (Bendick et al., 2007), numerous ramps and decollements (e.g., Elliott et al., 2016b; Hubbard et al., 2016; Mencin et al., 2016; Nábělek et al., 2009; Sathiakumar and Barbot, 2021; Sreejith et al., 2016) or the duplex faults for 2015 Nepal earthquake (Mendoza et al., 2019), as well as multiple planar faults overlaying a detachment fault for 2018 Papua New Guinea earthquake (Chong and Huang, 2020). In this study, our preferred composite model of ramp-flat and splay faults also reveals the structural complexity of this largest instrumentally recorded Mw 7.3 event in the Zagros so far. We therefore suggest that the structural complexity appears to be common for large events in active continental fold-and-thrust belts. Such common fault complexity also serves as a reminder that when we are modeling large earthquakes within orogenic belts, it is essential to consider the complexity of fault geometries.

6.5 Conclusion

In this chapter, we explore the coseismic and postseismic fault slip associated with the 2017 Mw 7.3 Sarpol-e Zahab earthquake using InSAR observations and FEM models. The best coseismic slip model constrained by kinematic inversions is a planar fault dipping 15°, which confirms the coseismic fault structure proposed by previous studies. Then we simulate mechanically frictional afterslip models using a number of different fault structures to check whether the fault complexity could further improve the model fit. Our finding suggests that a planar frictional afterslip model cannot fully explain the long-wavelength postseismic deformation field. In contrast, the ramp-flat fault model fits better to the data with a maximum afterslip of approximately 1.0 m updip of the coseismic rupture. The fault friction variations were found to be $\sim$0.001 and $\sim$0.0002 for the up-dip and down-dip portions of the ramp-flat fault, respectively. Based on the optimal ramp-flat fault model, we found that the combined model of the ramp-flat and splay faults further improves the model fit, although the frictional afterslip on the splay portion is minor (about 0.2 m) compared to the ramp-flat fault (about 0.9 m). The frictional variation for both the ramp-flat and splay fault in this optimal model is $\sim$0.0008. The combined model, implying a complex fault interaction between the sedimentary cover and crystalline basement, is best explained by the fault slip on the Mountain Front Fault in the Zagros.

7 Summary and Future Perspectives

This chapter provides a summary of the research findings and offers perspectives on future work. The detailed content is as follows.

7.1 Summary

This dissertation is based on InSAR observations and takes the 2017 Mw 7.3 Sarpol-e Zahab earthquake in the Zagros region as a case study. It focuses on modeling both coseismic and postseismic deformation and thoroughly investigates fault geometry and frictional characteristics during the postseismic phase. The key contributions of this research are as follows:

In Chapter 5, we use InSAR observations to investigate the fault geometry and postseismic deformation evolution within 3 years after a mainshock. Coseismic linear inversions reveal a planar fault which is capable of explaining the coseismic deformation better than the listric faults. The coseismic rupture highlights a unilaterally southward rupture involving sequential rupture of two asperities along a dextral-thrust fault.

The postseismic observations favor a ramp-flat structure in which the flat angle should be lower than 10°. The postseismic deformation is dominated by afterslip, while the viscoelastic response is negligible. A multisegment, stress-driven afterslip model (SA-2 model) with depth-varying frictional properties better explains the spatiotemporal evolution of the postseismic deformation than a two-segment, stress-driven afterslip model (SA-1 model). Although the SA-2 model does not improve the misfit significantly, this multisegment fault with depth-varying friction is more physically plausible given the depth-varying mechanical stratigraphy in the region. Compared to the kinematic afterslip model, the mechanical afterslip models with friction variation tend to underestimate early postseismic deformation to the west, which may indicate more complex fault structure or fault friction. In Chapter 6, we make a more in-depth analysis to the fault geometry complexity and fault friction complexity during the postseismic period.

Both the kinematic and stress-driven models can resolve downdip afterslip, although it could be affected by data noise and model resolution. The transition depth of the sedimentary cover basement interface inferred by afterslip models is $\sim$12 km in the seismogenic zone, which coincides with the regional stratigraphic profile.

In Chapter 6, we extend the time span of the InSAR data to around 4.5 years after the mainshock, and utilize the integration of InSAR observations and 2D FEM models incorporating various fault geometries such as planar faults, ramp-flat faults, and the combined models of ramp-flat and splay faults to explore frictional afterslip process due to coseismic stress changes following the mainshock. Our findings suggest that a ramp-flat frictional afterslip model, characterized by the maximum afterslip of $\sim$1.0 m better explains the long-wavelength postseismic deformation than planar fault models. However, an integration model of a ramp-flat and a splay fault further improves the model fit, although the splay fault's frictional slip is limited to < 0.2 m, which is much smaller than that on the ramp-flat part (∼0.9 m). Considering the relocated aftershocks and structural cross-sections, the combined model could be best attributed to fault slip on the blind Mountain Front Fault.

As the largest instrumentally recorded earthquake in the fold-and-thrust belt of the northwestern Zagros mountain so far, the fault structure of the 2017 Mw 7.3 Sarpol-e Zahab earthquake and its contribution to regional crustal shortening remain controversial. Because the coseismic rupture propagated along a basement-involved fault while the postseismic slip may activate the blind Mountain Front Fault in the sedimentary cover, the 2017 Sarpol-e Zahab earthquake may have acted as a typical event that contributed to both thick- and thin-skinned shortening of the Zagros in both seismic and aseismic ways, suggesting the complexity of the fault interactions between the basement and sedimentary cover in the Zagros.

7.2 Future Perspectives

Research on fault friction properties and lithospheric rheology based on postseismic deformation data has long been a challenging and significant topic in the geosciences. In this dissertation, we take the 2017 Mw 7.3 Sarpol-e Zahab earthquake as a case study to thoroughly analyze the postseismic deformation process. Building on existing research results, we can further expand our work in the following areas:

1. Fault Friction Properties Based on Precise Fault Geometry: Many previous studies using rate- and state-dependent or steady-state rate-dependent friction laws—whether assuming uniform or spatially varying friction along the fault—have been successful in dynamically modeling afterslip and explaining postseismic data. However, determining fault properties associated with the afterslip process remains challenging, especially when the fault structures are not precisely defined. Accurate fault geometry, combined with reliable geodetic observations and geological data, is essential for gaining meaningful insights into fault friction properties. In the future, we could focus on seismic events where ruptures reach the surface, allowing the surface fault trace to be precisely mapped through deformation data. This would reduce uncertainties in fault geometry and enable more accurate investigations of fault friction characteristics.

2. Comparison and Study of Other Afterslip Mechanisms: Currently, most research on afterslip modeling utilizes either kinematic or stress-driven (frictional) afterslip models. Kinematic afterslip models, with their greater number of free parameters, often provide better fits to observational data, but they may result in non-physical solutions. On the other hand, stress-driven afterslip models, based on rate-state friction equations, impose more physical constraints but may struggle to fit postseismic data in some cases. In addition to these classical models, new approaches have emerged. For example, Meade (2024) developed a novel kinematic afterslip model based on the concept of geometric moment, while Aben and Brantut (2023) found that fluid-induced afterslip is promoted by local fluid pressure recharge in laboratory experiments. These recent findings offer new perspectives on afterslip behavior and could be applied and compared across different case studies.

3. Modeling the Complete Earthquake Cycle: Research on the full earthquake cycle encompasses pre-seismic, coseismic, and postseismic phases. As geodetic technology advances, we now have access to increasingly rich geodetic data, which allows us to study the full seismic cycle of individual faults. Such research is crucial for understanding the coseismic, postseismic, and interseismic processes. Physically linking postseismic and interseismic phases will enable us to more accurately recognize the systematic and variable nature of seismic cycle deformation patterns and mechanisms.

List of Figures

List of Tables

Bibliography

Aagaard BT, Knepley MG, Williams CA (2013) A domain decomposition approach to implementing fault slip in finite-element models of quasi-static and dynamic crustal deformation. Journal of Geophysical Research: Solid Earth 118(6):3059–3079

Aben FM, Brantut N (2023) Rupture and afterslip controlled by spontaneous local fluid flow in crustal rock. Journal of Geophysical Research: Solid Earth 128(11):e2023JB027534

Afsari N, Sodoudi F, Farahmand FT, Ghassemi MR (2011) Crustal structure of northwest zagros (kermanshah) and central iran (yazd and isfahan) using teleseismic ps converted phases. Journal of Seismology 15(2):341–353

Alavi M (2007) Structures of the zagros fold-thrust belt in iran. American Journal of Science 307:1064–1095

Allen MB, Saville C, Blanc EJ, Talebian M, Nissen E (2013) Orogenic plateau growth: Expansion of the turkish-iranian plateau across the zagros fold-and-thrust belt. Tectonics 32:171–190

Avouac JP (2015) From geodetic imaging of seismic and aseismic fault slip to dynamic modeling of the seismic cycle. Annual Review of Earth and Planetary Sciences 43(1):233–271

Avouac JP, Tapponnier P (1993) Kinematic model of active deformation in central asia. Geophysical Research Letters 20(10):895–898

Avouac JP, Ayoub F, Leprince S, Konca O, Helmberger DV (2006) The 2005, mw 7.6 kashmir earthquake: Sub-pixel correlation of aster images and seismic waveforms analysis. Earth and Planetary Science Letters 249(3-4):514–528

Barbot S, Fialko Y, Bock Y (2009) Postseismic deformation due to the mw 6.0 2004 parkfield earthquake: Stress-driven creep on a fault with spatially variable rate-and-state friction parameters. Journal of Geophysical Research 114(B7):B07405

Barbot S, Moore JDP, Lambert V (2017) Displacement and stress associated with distributed anelastic deformation in a half-space. Bulletin of the Seismological Society of America 107(2):821–855

Barnhart WD, Lohman RB (2013) Phantom earthquakes and triggered aseismic creep: Vertical partitioning of strain during earthquake sequences in iran. Geophysical Research Letters 40:819–823

Barnhart WD, Brengman CM, Li S, Peterson KE (2018) Ramp-flat basement structures of the zagros mountains inferred from co-seismic slip and afterslip of the 2017 mw7.3 darbandikhan, iran/iraq earthquake. Earth and Planetary Science Letters 496:96–107

Basilici M, Ascione A, Megna A, Santini S, Tavani S, Valente E, Mazzoli S (2020) Active deformation and relief evolution in the western lurestan region of the zagros mountain belt: New insights from tectonic geomorphology analysis and finite element modeling. Tectonics 39(12):1–27

Bekaert D, Walters R, Wright T, Hooper A, Parker D (2015) Statistical comparison of insar tropospheric correction techniques. Remote Sensing of Environment 170:40–47

Ben-Zion Y (2001) Dynamic ruptures in recent models of earthquake faults. Journal of the Mechanics and Physics of Solids 49(9):2209–2244

Bendick R, Bilham R, Khan MA, Khan SF (2007) Slip on an active wedge thrust from geodetic observations of the 8 october 2005 kashmir earthquake. Geology 35(3):267–270

Berardino P, Fornaro G, Lanari R, Sansosti E (2002) A new algorithm for surface deformation monitoring based on small baseline differential sar interferograms. IEEE Transactions on Geoscience and Remote Sensing 40(11):2375–2383

Berberian M (1995) Master "blind" thrust faults hidden under the zagros folds: Active basement tectonics and surface morphotectonics. Tectonophysics 241:193–224

Biggs J, Wright T, Lu Z, Parsons B (2007) Multi-interferogram method for measuring interseismic deformation: Denali fault, alaska. Geophysical Journal International 170(3):1165–1179

Bird P (2003) An updated digital model of plate boundaries. Geochemistry, Geophysics, Geosystems 4(3)

Bletery Q, Nocquet JM (2023) The precursory phase of large earthquakes. Science 381(6655):297–301

Bletery Q, Cavalié O, Nocquet JM, Ragon T (2020) Distribution of interseismic coupling along the north and east anatolian faults inferred from insar and gps data. Geophysical Research Letters 47(16):e2020GL087775

Bürgmann R (2023) Reliable earthquake precursors? Science 381(6655):266–267

Bürgmann R, Dresen G (2008) Rheology of the lower crust and upper mantle: Evidence from rock mechanics, geodesy, and field observations. Annual Review of Earth and Planetary Sciences 36(1):531–567

Bürgmann R, Rosen PA, Fielding EJ (2000) Synthetic aperture radar interferometry to measure earth's surface topography and its deformation. Annual Review of Earth and Planetary Sciences 28(1):169–209

Bürgmann R, Hilley G, Ferretti A, Novali F (2006) Resolving vertical tectonics in the san francisco bay area from permanent scatterer insar and gps analysis. Geology 34(3):221–224

Byerlee J (1978) Friction of rocks. pure and applied geophysics 116(4):615–626

Cao Y, Li Z, Wei J, Hu J, Duan M, Feng G (2018) Stochastic modeling for time series insar: with emphasis on atmospheric effects. Journal of Geodesy 92:185–204

Carpenter B, Saffer D, Marone C (2012) Frictional properties and sliding stability of the san andreas fault from deep drill core. Geology 40(8):759–762

Casciello E, Vergés J, Saura E, Casini G, Fernández N, Blanc E, Homke S, Hunt DW (2009) Fold patterns and multilayer rheology of the lurestan province, zagros simply folded belt (iran). Journal of the Geological Society, London 166:947–959

Cavalié O, Lasserre C, Doin MP, Peltzer G, Sun J, Xu X, Shen ZK (2008) Measurement of interseismic strain across the haiyuan fault (gansu, china), by insar. Earth and Planetary Science Letters 275(3-4):246–257

Chang SH, Avouac JP, Barbot S, Lee JC (2013) Spatially variable fault friction derived from dynamic modeling of aseismic afterslip due to the 2004 parkfield earthquake. Journal of Geophysical Research: Solid Earth 118(7):3431–3447

Chen K, Xu W, Mai PM, Gao H, Zhang L, Ding X (2018) The 2017 mw 7.3 sarpol zahāb earthquake, iran: A compact blind shallow-dipping thrust event in the mountain front fault basement. Tectonophysics 747–748:108–114

Chinnery MA, Jovanovich DB (1972) Effect of earth layering on earthquake displacement fields. Bulletin of the Seismological Society of America 62(6):1629–1639

Chong JH, Huang MH (2020) Refining the 2018 mw 7.5 papua new guinea earthquake fault-slip model using subpixel offset. Bulletin of the Seismological Society of America 111(2):1032–1042

Colesanti C, Ferretti A, Novali F, Prati C, Rocca F (2003) Sar monitoring of progressive and seasonal ground deformation using the permanent scatterers technique. IEEE Transactions on Geoscience and Remote Sensing 41(7):1685–1701

Collettini C, Niemeijer A, Viti C, Smith SAF, Marone C (2011) Fault structure, frictional properties and mixed-mode fault slip behavior. Earth and Planetary Science Letters 311(3):316–327

Copley A, Karasozen E, Oveisi B, Elliott JR, Samsonov S, Nissen E (2015) Seismogenic faulting of the sedimentary sequence and laterally variable material properties in the zagros mountains (iran) revealed by the august 2014 murmuri (e. dehloran) earthquake sequence. Geophysical Journal International 203:1436–1459

Dal Zilio L, van Dinther Y, Gerya T, Avouac JP (2019) Bimodal seismicity in the himalaya controlled by fault friction and geometry. Nature Communications 10(1):48

Daout S, Parsons B, Walker R (2021) Post-earthquake fold growth imaged in the qaidam basin, china, with interferometric synthetic aperture radar. Journal of Geophysical Research: Solid Earth 126(3):e2020JB021241

Diao F, Wang R, Xiong X, Liu C (2021) Overlapped postseismic deformation caused by afterslip and viscoelastic relaxation following the 2015 mw 7.8 gorkha (nepal) earthquake. Journal of Geophysical Research: Solid Earth 126

Dieterich JH (1979) Modeling of rock friction: 1. experimental results and constitutive equations. Journal of Geophysical Research: Solid Earth 84(B5):2161–2168

Dutta R, Jónsson S, Vasyura-Bathke H (2021) Simultaneous bayesian estimation of non-planar fault geometry and spatially-variable slip. Journal of Geophysical Research: Solid Earth 126(7):e2020JB020441

Eineder M, Adam N, Bamler R, Yague-Martinez N, Breit H (2009) Spaceborne spotlight sar interferometry with terrasar-x. IEEE Transactions on Geoscience and Remote Sensing 47(5):1524–1535

Elliott J, Walters R, Wright T (2016a) The role of space-based observation in understanding and responding to active tectonics and earthquakes. Nature Communications 7(1):13844

Elliott JR, Biggs J, Parsons B, Wright T (2008) Insar slip rate determination on the altyn tagh fault, northern tibet, in the presence of topographically correlated atmospheric delays. Geophysical Research Letters 35(12)

Elliott JR, Jolivet R, Gonzalez PJ, Avouac JP, Hollingsworth J, Searle MP, Stevens VL (2016b) Himalayan megathrust geometry and relation to topography revealed by the gorkha earthquake. Nature Geoscience 9(2):174–180

Emami H, Vergés J, Nalpas T, Gillespie P, Sharp I, Karpuz R, Blanc EP, Goodarzi MG (2010) Structure of the mountain front flexure along the anaran anticline in the pusht-e kuh arc (nw zagros, iran): Insights from sand box models. Geological Society, London, Special Publications 330:155–178

Emardson T, Simons M, Webb F (2003) Neutral atmospheric delay in interferometric synthetic aperture radar applications: Statistical description and mitigation. Journal of Geophysical Research: Solid Earth 108(B5)

Falcon NL (1969) Problems of the relationship between surface structure and deep displacements illustrated by the zagros range. Geological Society of London, Special Publication 3:9–21

Fang J, Houseman GA, Wright TJ, Evans LA, Craig TJ, Elliott JR, Hooper A (2024) The dynamics of the india-eurasia collision: Faulted viscous continuum models constrained by high-resolution sentinel-1 insar and gnss velocities. Journal of Geophysical Research: Solid Earth 129(6):e2023JB028571

Farr TG, Rosen PA, Caro E, Crippen R, Duren R, Hensley S, Kobrick M, Paller M, Rodriguez E, Roth L, Seal D, Shaffer S, Shimada J, Umland J, Werner M, Oskin M, Burbank D, Alsdorf D (2007) The shuttle radar topography mission. Reviews of Geophysics 45(2)

Fathian A, Atzori S, Nazari H, Reicherter K, Salvi S, Svigkas N, Tatar M, Tolomei C, Yaminifard F (2021) Complex co- and postseismic faulting of the 2017–2018 seismic sequence in western iran revealed by insar and seismic data. Remote Sensing of Environment 253

Feng L, Barbot S, Hill EM, Hermawan I, Banerjee P, Natawidjaja DH (2016) Footprints of past earthquakes revealed in the afterslip of the 2010 mw 7.8 mentawai tsunami earthquake. Geophysical Research Letters 43(18):9518–9526

Feng W, Li Z, Elliott JR, Fukushima Y, Hoey T, Singleton A, Cook R, Xu Z (2013) The 2011 mw 6.8 burma earthquake: Fault constraints provided by multiple sar techniques. Geophysical Journal International 195(1):650–660

Feng W, Lindsey E, Barbot S, Samsonov S, Dai K, Li P, Li Z, Almeida R, Chen J, Xu X (2017) Source characteristics of the 2015 mw 7.8 gorkha (nepal) earthquake and its mw 7.2 aftershock from space geodesy. Tectonophysics 712–713:747–758

Feng W, Samsonov S, Almeida R, Yassaghi A, Li J, Qiu Q, Li P, Zheng W (2018) Geodetic constraints of the 2017 mw7.3 sarpol zahab, iran earthquake, and its implications on the structure and mechanics of the northwest zagros thrust-fold belt. Geophysical Research Letters 45(14):6853–6861

Ferretti A, Prati C, Rocca F (2000) Nonlinear subsidence rate estimation using permanent scatterers in differential sar interferometry. IEEE Transactions on geoscience and remote sensing 38(5):2202–2212

Ferretti A, Monti-Guarnieri A, Prati C, Rocca F, Massonet D (2007) InSAR principles-guidelines for SAR interferometry processing and interpretation, vol 19

Fialko Y (2006) Interseismic strain accumulation and the earthquake potential on the southern san andreas fault system. Nature 441(7096):968–971

Fialko Y, Simons M, Agnew D (2001) The complete (3-d) surface displacement field in the epicentral area of the 1999 mw7.1 hector mine earthquake, california, from space geodetic observations. Geophysical Research Letters 28(16):3063–3066

Flesch L, Haines A, Holt W (2001) Dynamics of the india-eurasia collision zone (paper 2001jb000208). JOURNAL OF GEOPHYSICAL RESEARCH-ALL SERIES- 106(8; SECT 2):16–435

Floyd MA, Walters RJ, Elliott JR, Funning GJ, Svarc JL, Murray JR, Hooper AJ, Larsen Y, Marinkovic P, Bürgmann R, Johanson IA, Wright TJ (2016) Spatial variations in fault friction related to lithology from rupture and afterslip of the 2014 south napa, california, earthquake. Geophysical Research Letters 43(13):6808–6816

Foster J, Brooks B, Cherubini T, Shacat C, Businger S, Werner C (2006) Mitigating atmospheric noise for insar using a high resolution weather model. Geophysical Research Letters 33(16)

Freed AM, Bürgmann R (2004) Evidence of power-law flow in the mojave desert mantle. Nature 430(6999):548–551

Freed AM, Bürgmann R, Calais E, Freymueller J, Hreinsdóttir S (2006) Implications of deformation following the 2002 denali, alaska, earthquake for postseismic relaxation processes and lithospheric rheology. Journal of Geophysical Research: Solid Earth 111(B01401)

Fujiwara S, Nishimura T, Murakami M, Nakagawa H, Tobita M, Rosen PA (2000) 2.5-d surface deformation of m6.1 earthquake near mt iwate detected by sar interferometry. Geophysical Research Letters 27(14):2049–2052

Fukuda J, Johnson KM, Larson KM, Miyazaki S (2009) Fault friction parameters inferred from the early stages of afterslip following the 2003 tokachi-oki earthquake. Journal of Geophysical Research: Solid Earth 114(B4)

Gombert B, Duputel Z, Shabani E, Rivera L, Jolivet R, Hollingsworth J (2019) Impulsive source of the 2017 mw=7.3 ezgeleh, iran, earthquake. Geophysical Research Letters 46:5207–5216

Grandin R, Vallée M, Satriano C, Lacassin R, Klinger Y, Simoes M, Bollinger L (2015) Rupture process of the mw= 7.9 2015 gorkha earthquake (nepal): Insights into himalayan megathrust segmentation. Geophysical Research Letters 42(20):8373–8382

Guo Z, Wen Y, Xu G, Wang S, Wang X, Liu Y, Xu C (2019) Fault slip model of the 2018 mw 6.6 hokkaido eastern iburi, japan, earthquake estimated from satellite radar and gps measurements. Remote Sensing 11(14):1667

Guo Z, Motagh M, Hu JC, Xu G, Haghighi MH, Bahroudi A, Fathian A, Li S (2022) Depth-varying friction on a ramp-flat fault illuminated by ∼3-year insar observations following the 2017 mw 7.3 sarpol-e zahab earthquake. Journal of Geophysical Research: Solid Earth 127(12):e2022JB025148

Guo Z, Baes M, Motagh M (2024) Ramp-flat and splay faulting illuminated by frictional afterslip following the 2017 mw 7.3 sarpol-e zahab earthquake. Seismological Research Letters

Hanssen RF (2001) Radar interferometry: data interpretation and error analysis, vol 2. Springer Science & Business Media

Hatzfeld D, Tatar M, Priestley K, Ghafory-Ashtiany M (2003) Seismological constraints on the crustal structure beneath the zagros mountain belt (iran). Geophysical Journal International 155(2):403–410

Hearn EH, Bürgmann R, Reilinger RE (2002) Dynamics of izmit earthquake postseismic deformation and loading of the düzce earthquake hypocenter. Bulletin of the Seismological Society of America 92(1):172–193

Hearn EH, McClusky S, Ergintav S, Reilinger RE (2009) Izmit earthquake postseismic deformation and dynamics of the north anatolian fault zone. Journal of Geophysical Research: Solid Earth 114(B8)

Helmstetter A, Shaw BE (2009) Afterslip and aftershocks in the rate-and-state friction law. Journal of Geophysical Research: Solid Earth 114(B1)

Hessami K, Koyi HA, Talbot CJ (2001) The significance of strike-slip faulting in the basement of the zagros fold and thrust belt. Journal of Petroleum Geology 24(1):5–28

Hirose H, Kato A, Kimura T (2024) Did short-term preseismic crustal deformation precede the 2011 great tohoku-oki earthquake? an examination of stacked tilt records. Geophysical Research Letters 51(12):e2024GL109384

Hooper A, Zebker H, Segall P, Kampes B (2004) A new method for measuring deformation on volcanoes and other natural terrains using insar persistent scatterers. Geophysical Research Letters 31(23)

Hsu YJ, Bechor N, Segall P, Yu SB, Kuo LC, Ma KF (2002) Rapid afterslip following the 1999 chi-chi, taiwan earthquake. Geophysical Research Letters 29(16):1–4–1–4

Hu J, Li Z, Ding X, Zhu J, Zhang L, Sun Q (2012) 3d coseismic displacement of 2010 darfield, new zealand earthquake estimated from multi-aperture insar and d-insar measurements. Journal of Geodesy 86:1029–1041

Huang MH, Bürgmann R, Freed AM (2014) Probing the lithospheric rheology across the eastern margin of the tibetan plateau. Earth and Planetary Science Letters 396:88–96

Hubbard J, Almeida R, Foster A, Sapkota SN, Bürgi P, Tapponnier P (2016) Structural segmentation controlled the 2015 mw 7.8 gorkha earthquake rupture in nepal. Geology 44(8):639–642

Hussain E, Hooper A, Wright TJ, Walters RJ, Bekaert DP (2016) Interseismic strain accumulation across the central north anatolian fault from iteratively unwrapped insar measurements. Journal of Geophysical Research: Solid Earth 121(12):9000–9019

Ingleby T, Wright TJ, Hooper A, Craig TJ, Elliott JR (2020) Constraints on the geometry and frictional properties of the main himalayan thrust using coseismic, postseismic, and interseismic deformation in nepal. Journal of Geophysical Research: Solid Earth 125(2):1–26

Jamalreyhani M, Rezapour M, Cesca S, Dahm T, Heimann S, Sudhaus H, Isken MP (2022) Insight into the 2017-2019 lurestan arc seismic sequence (zagros, iran); complex earthquake interaction in the basement and sediments. Geophysical Journal International 230(1):114–130

Ji C, Helmberger DV, Alex Song TR, Ma KF, Wald DJ (2001) Slip distribution and tectonic implication of the 1999 chi-chi, taiwan, earthquake. Geophysical Research Letters 28(23):4379–4382

Ji C, Helmberger DV, Wald DJ, Ma KF (2003) Slip history and dynamic implications of the 1999 chi-chi, taiwan, earthquake. Journal of Geophysical Research: Solid Earth 108(B9)

Johnson KM, Segall P (2004) Imaging the ramp–décollement geometry of the chelungpu fault using coseismic gps displacements from the 1999 chi-chi, taiwan earthquake. Tectonophysics 378(1):123–139

Johnson KM, Hsu YJ, Segall P, Yu SB (2001) Fault geometry and slip distribution of the 1999 chi-chi, taiwan earthquake imaged from inversion of gps data. Geophysical Research Letters 28(11):2285–2288

Johnson KM, Bürgmann R, Larson K (2006) Frictional properties on the san andreas fault near parkfield, california, inferred from models of afterslip following the 2004 earthquake. Bulletin of the Seismological Society of America 96(4B):S321–S338

Jolivet R, Cattin R, Chamot-Rooke N, Lasserre C, Peltzer G (2008) Thin-plate modeling of interseismic deformation and asymmetry across the altyn tagh fault zone. Geophysical Research Letters 35(2)

Jolivet R, Bürgmann R, Houlié N (2009) Geodetic exploration of the elastic properties across and within the northern san andreas fault zone. Earth and Planetary Science Letters 288(1):126–131

Jolivet R, Lasserre C, Doin MP, Peltzer G, Avouac JP, Sun J, Dailu R (2013) Spatio-temporal evolution of aseismic slip along the haiyuan fault, china: Implications for fault frictional properties. Earth and Planetary Science Letters 377–378:23–33

Jolivet R, Simons M, Agram PS, Duputel Z, Shen ZK (2015) Aseismic slip and seismogenic coupling along the central san andreas fault. Geophysical Research Letters 42(2):297–306

Jónsson S, Zebker H, Segall P, Amelung F (2002) Fault slip distribution of the 1999 mw 7.1 hector mine, california, earthquake, estimated from satellite radar and gps measurements. Bulletin of the Seismological Society of America 92(4):1377–1389

Jónsson S, Segall P, Pedersen R, Björnsson G (2003) Post-earthquake ground movements correlated to pore-pressure transients. Nature 424(6945):179–183

Jouanne F, Awan A, Madji A, Pêcher A, Latif M, Kausar A, Mugnier JL, Khan I, Khan NA (2011) Postseismic deformation in pakistan after the 8 october 2005 earthquake: Evidence of afterslip along a flat north of the balakot-bagh thrust. Journal of Geophysical Research: Solid Earth 116(B7)

Jung J, Kim Dj, Park SE (2013) Correction of atmospheric phase screen in time series insar using wrf model for monitoring volcanic activities. IEEE Transactions on Geoscience and Remote Sensing 52(5):2678–2689

Kaneko Y, Fialko Y, Sandwell DT, Tong X, Furuya M (2013) Interseismic deformation and creep along the central section of the north anatolian fault (turkey): Insar observations and implications for rate-and-state friction properties. Journal of Geophysical Research: Solid Earth 118(1):316–331

Karato Si (2008) Deformation of earth materials. An introduction to the rheology of Solid Earth 463

Khorrami F, Vernant P, Masson F, Nilfouroushan F, Mousavi Z, Nankali H, Saadat SA, Walpersdorf A, Hosseini S, Tavakoli P, Aghamohammadi A, Alijanzade M (2019) An up-to-date crustal deformation map of iran using integrated campaign-mode and permanent gps velocities. Geophysical Journal International 217:832–843

Kirkpatrick S, Gelatt CD, Vecchi MP (1983) Optimization by simulated annealing. Science 220(4598):671–680

Koshnaw RI, Stockli DF, Horton BK, Teixell A, Barber DE, Kendall JJ (2020) Late miocene deformation kinematics along the nw zagros fold-thrust belt, kurdistan region of iraq: Constraints from apatite (u-th)/he thermochronometry and balanced cross sections. Tectonics 39(12):1–37

Lanari R, Zoffoli S, Sansosti E, Fornaro G, Serafino F (2001) New approach for hybrid strip-map/spotlight sar data focusing. IEE Proceedings-Radar, Sonar and Navigation 148(6):363–372

Lay T (2018) A review of the rupture characteristics of the 2011 tohoku-oki mw 9.1 earthquake. Tectonophysics 733:4–36

Lazecký M, Spaans K, González PJ, Maghsoudi Y, Morishita Y, Albino F, Elliott J, Greenall N, Hatton E, Hooper A, Juncu D, McDougall A, Walters RJ, Watson CS, Weiss JR, Wright TJ (2020) Licsar: An automatic insar tool for measuring and monitoring tectonic and volcanic activity. Remote Sensing 12(15):2430

Le Garzic E, Vergés J, Sapin F, Saura E, Meresse F, Ringenbach JC (2019) Evolution of the nw zagros fold-and-thrust belt in kurdistan region of iraq from balanced and restored crustal-scale sections and forward modeling. Journal of Structural Geology 124:51–69

Lee SJ, Ma KF, Chen HW (2006) Effects of fault geometry and slip style on near-fault static displacements caused by the 1999 chi-chi, taiwan earthquake. Earth and Planetary Science Letters 241(1):336–350

Li S, Wang K, Wang Y, Jiang Y, Dosso SE (2018) Geodetically inferred locking state of the cascadia megathrust based on a viscoelastic earth model. Journal of Geophysical Research: Solid Earth 123(9):8056–8072

Li Z, Muller JP, Cross P (2003) Comparison of precipitable water vapor derived from radiosonde, gps, and moderate-resolution imaging spectroradiometer measurements. Journal of Geophysical Research: Atmospheres 108(D20)

Li Z, Pasquali P, Cantone A, Singleton A, Funning G, Forrest D (2011) Meris atmospheric water vapor correction model for wide swath interferometric synthetic aperture radar. IEEE Geoscience and Remote Sensing Letters 9(2):257–261

Lienkaemper JJ, McFarland FS (2017) Long-term afterslip of the 2004 m 6.0 parkfield, california, earthquake—implications for forecasting amount and duration of afterslip on other major creeping faults. Bulletin of the Seismological Society of America 107(3):1082–1093

Lisowski M, Prescott W, Savage JC, Johnston M (1990) Geodetic estimate of coseismic slip during the 1989 loma prieta, california, earthquake. Geophysical Research Letters 17(9):1437–1440

Liu X, Xu W (2019) Logarithmic model joint inversion method for coseismic and postseismic slip: Application to the 2017 mw 7.3 sarpol zahāb earthquake, iran. Journal of Geophysical Research: Solid Earth 124:12034–12052

Loveless JP, Meade BJ (2011) Partitioning of localized and diffuse deformation in the tibetan plateau from joint inversions of geologic and geodetic observations. Earth and Planetary Science Letters 303(1-2):11–24

Lu Z, Dzurisin D (2014) InSAR Imaging of Aleutian Volcanoes: Monitoring a Volcanic Arc from Space. Springer Berlin Heidelberg, Berlin, Heidelberg

Lv X, Amelung F, Shao Y, Ye S, Liu M, Xie C (2020) Rheology of the zagros lithosphere from post-seismic deformation of the 2017 mw7.3 kermanshah, iraq, earthquake. Remote Sensing 12(2032)

Ma KF, Song TRA, Lee SJ, Wu HI (2000) Spatial slip distribution of the september 20, 1999, chi-chi, taiwan, earthquake (mw7.6) —inverted from teleseismic data. Geophysical Research Letters 27(20):3417–3420

Maheri-Peyrov M, Ghods A, Donner S, Akbarzadeh-Aghdam M, Sobouti F, Motaghi K, Hassanzadeh M, Mortezanejad G, Talebian M, Chen L (2020) Upper crustal structure of nw iran revealed by regional 3-d pg velocity tomography. Geophysical Journal International 222(2):1093–1108

Mahmoodabadi M, Yaminifard F, Tatar M, Kaviani A, Motaghi K (2019) Upper-mantle velocity structure beneath the zagros collision zone, central iran and alborz from nonlinear teleseismic tomography. Geophysical Journal International 218(1):414–428

Mansinha L, Smylie D (1971) The displacement fields of inclined faults. Bulletin of the Seismological Society of America 61(5):1433–1440

Marone C (1998a) The effect of loading rate on static friction and the rate of fault healing during the earthquake cycle. Nature 391(6662):69–72

Marone C (1998b) Laboratory-derived friction laws and their application to seismic faulting. Annual Review of Earth and Planetary Sciences 26(1):643–696

Marone CJ, Scholtz CH, Bilham R (1991) On the mechanics of earthquake afterslip. Journal of Geophysical Research: Solid Earth 96(B5):8441–8452

Massonnet D, Feigl KL (1998) Radar interferometry and its application to changes in the earth's surface. Reviews of geophysics 36(4):441–500

Massonnet D, Rossi M, Carmona C, Adragna F, Peltzer G, Feigl K, Rabaute T (1993) The displacement field of the landers earthquake mapped by radar interferometry. Nature 364(6433):138–142

McGinley JR (1969) A comparision of observed permanent titles and strains due to earthquakes with those calculated from displaced dislocations in elastic earth models. PhD thesis, California institute of Technology

McQuarrie N (2004) Crustal scale geometry of the zagros fold-thrust belt, iran. Journal of Structural Geology 26:519–535

Meade BJ (2024) Kinematic afterslip patterns. Geophysical Research Letters 51(1):e2023GL105797

Mencin D, Bendick R, Upreti BN, Adhikari DP, Gajurel AP, Bhattarai RR, Shrestha HR, Bhattarai TN, Manandhar N, Galetzka J, Knappe E, Pratt-Sitaula B, Aoudia A, Bilham R (2016) Himalayan strain reservoir inferred from limited afterslip following the gorkha earthquake. Nature Geoscience 9(7):533–537

Mendoza MM, Ghosh A, Karplus MS, Klemperer SL, Sapkota SN, Adhikari LB, Velasco A (2019) Duplex in the main himalayan thrust illuminated by aftershocks of the 2015 m w 7.8 gorkha earthquake. Nature Geoscience 12(12):1018–1022

Meyer F (2019) Synthetic Aperture Radar (SAR) Handbook: Comprehensive Methodologies for Forest Monitoring and Biomass Estimation

Molinaro M, Leturmy P, Guezou JC, Frizon de Lamotte D, Eshraghi SA (2005) The structure and kinematics of the southeastern zagros fold-thrust belt, iran: From thin-skinned to thick-skinned tectonics. Tectonics 24(TC3007)

Moreno M, Li S, Melnick D, Bedford JR, Baez JC, Motagh M, Metzger S, Vajedian S, Sippl C, Gutknecht BD, Contreras-Reyes E, Deng Z, Tassara A, Oncken O (2018) Chilean megathrust earthquake recurrence linked to frictional contrast at depth. Nature Geoscience 11(4):285–290

Morishita Y, Lazecky M, Wright TJ, Weiss JR, Elliott JR, Hooper A (2020) Licsbas: An open-source insar time series analysis package integrated with the licsar automated sentinel-1 insar processor. Remote Sensing 12(3):424

Motagh M, Bahroudi A, Haghighi MH, Samsonov S, Fielding E, Wetzel HU (2015) The 18 august 2014 mw 6.2 mormori, iran, earthquake: A thin-skinned faulting in the zagros mountain inferred from insar measurements. Seismological Research Letters 86(3):775–782

Motagh M, Shamshiri R, Haghshenas Haghighi M, Wetzel HU, Akbari B, Nahavandchi H, Roessner S, Arabi S (2017) Quantifying groundwater exploitation induced subsidence in the rafsanjan plain, southeastern iran, using insar time-series and in situ measurements. Engineering Geology 218:134–151

Motaghi K, Shabanian E, Kalvandi F (2017) Underplating along the northern portion of the zagros suture zone, iran. Geophysical Journal International 210(1):375–389

Mouthereau F, Lacombe O, Vergés J (2012) Building the zagros collisional orogen: Timing, strain distribution and the dynamics of arabia/eurasia plate convergence. Tectonophysics 532–535:27–60

Nábělek J, Hetényi G, Vergne J, Sapkota S, Kafle B, Jiang M, Su H, Chen J, Huang BS, Team tHC (2009) Underplating in the himalaya-tibet collision zone revealed by the hi-climb experiment. Science 325(5946):1371–1374

Nissen E, Tatar M, Jackson JA, Allen MB (2011) New views on earthquake faulting in the zagros fold-and-thrust belt of iran. Geophysical Journal International 186:928–944

Nissen E, Ghods A, Karasözen E, Elliott JR, Barnhart WD, Bergman EA, Hayes GP, Jamal-Reyhani M, Nemati M, Tan F, Abdulnaby W, Benz HM, Shahvar MP, Talebian M, Chen L (2019) The 12 november 2017 mw 7.3 ezgeleh-sarpolzahab (iran) earthquake and active tectonics of the lurestan arc. Journal of Geophysical Research: Solid Earth 124(2):2124–2152

Nur A, Mavko G (1974) Postseismic viscoelastic rebound. Science 183(4121):204–206

Okada Y (1985) Surface deformation due to shear and tensile faults in a half-space. Bulletin of the Seismological Society of America 75(4):1135–1154

Okada Y (1992) Internal deformation due to shear and tensile faults in a half-space. Bulletin of the Seismological Society of America 82(2):1018–1040

Ozawa S, Nishimura T, Suito H, Kobayashi T, Tobita M, Imakiire T (2011) Coseismic and post-seismic slip of the 2011 magnitude-9 tohoku-oki earthquake. Nature 475(7356):373–376

O'Brien C (1950) Tectonic problems of the oil field belt of southwest iran. In: 18th International Geological Congress. Great Britain, Proceedings, vol 6, pp 45–58

Peltzer G, Rosen P, Rogez F, Hudnut K (1996) Postseismic rebound in fault step-overs caused by pore fluid flow. Science 273(5279):1202–1204

Peltzer G, Rosen P, Rogez F, Hudnut K (1998) Poroelastic rebound along the landers 1992 earthquake surface rupture. Journal of Geophysical Research: Solid Earth 103(B12):30131–30145

Perfettini H, Avouac JP (2004) Postseismic relaxation driven by brittle creep: A possible mechanism to reconcile geodetic measurements and the decay rate of aftershocks, application to the chi-chi earthquake, taiwan: Dynamics of brittle creep. Journal of Geophysical Research: Solid Earth 109(B2)

Perfettini H, Avouac JP (2007) Modeling afterslip and aftershocks following the 1992 landers earthquake. Journal of Geophysical Research 112(B7):B07409

Pollitz FF (1996) Coseismic deformation from earthquake faulting on a layered spherical earth. Geophysical Journal International 125(1):1–14

Pollitz FF (2003) Transient rheology of the uppermost mantle beneath the mojave desert, california. Earth and Planetary Science Letters 215(1):89–104

Qiao X, Zhou Y (2021) Geodetic imaging of shallow creep along the xianshuihe fault and its frictional properties. Earth and Planetary Science Letters 567:117001

Roeloffs EA (2006) Evidence for aseismic deformation rate changes prior to earthquakes. Annu Rev Earth Planet Sci 34(1):591–627

Ruina A (1983) Slip instability and state variable friction laws. Journal of Geophysical Research: Solid Earth 88(B12):10359–10370

Sadeghi S, Yassaghi A (2016) Spatial evolution of zagros collision zone in kurdistan, nw iran: Constraints on arabia–eurasia oblique convergence. Solid Earth 7:659–672

Sandwell DT, Price EJ (1998) Phase gradient approach to stacking interferograms. Journal of Geophysical Research: Solid Earth 103(B12):30183–30204

Sathiakumar S, Barbot S (2021) The stop-start control of seismicity by fault bends along the main himalayan thrust. Communications Earth & Environment 2(87)

Sato R (1971) Crustal deformation due to dislocation in a multi-layered medium. Journal of Physics of the Earth 19(1):31–46

Savage J, Prescott W (1978) Asthenosphere readjustment and the earthquake cycle. Journal of Geophysical Research: Solid Earth 83(B7):3369–3376

Savage JC, Langbein J (2008) Postearthquake relaxation after the 2004 m6 parkfield, california, earthquake and rate-and-state friction. Journal of Geophysical Research: Solid Earth 113(B10)

Scholz CH (1998) Earthquakes and friction laws. Nature 391(6662):37–42

Scholz CH (2019) The mechanics of earthquakes and faulting. Cambridge university press

Shamshiri R, Motagh M, Nahavandchi H, Haghighi MH, Hoseini M (2020) Improving tropospheric corrections on large-scale sentinel-1 interferograms using a machine learning approach for integration with gnss-derived zenith total delay (ztd). Remote Sensing of Environment 239:111608

Shen ZK, Jackson DD, Feng Y, Cline M, Kim M, Fang P, Bock Y (1994) Postseismic deformation following the landers earthquake, california, 28 june 1992. Bulletin of the Seismological Society of America 84(3):780–791

Simons M, Rosen P (2007) Interferometric synthetic aperture radar geodesy. Geodesy 3:391–446

Smylie D, Mansinha L (1971) The elasticity theory of dislocations in real earth models and changes in the rotation of the earth. Geophysical Journal International 23(3):329–354

Sreejith KM, Sunil PS, Agrawal R, Saji AP, Ramesh DS, Rajawat AS (2016) Coseismic and early postseismic deformation due to the 25 april 2015, mw 7.8 gorkha, nepal, earthquake from insar and gps measurements. Geophysical Research Letters 43(7):3160–3168

Steketee J (1958) On volterra's dislocations in a semi-infinite elastic medium. Canadian Journal of Physics 36(2):192–205

Talebian M, Jackson J (2004) A reappraisal of earthquake focal mechanisms and active shortening in the zagros mountains of iran. Geophysical Journal International 156:506–526

Tavani S, Parente M, Puzone F, Corradetti A, Gharabeigli G, Valinejad M, Morsalnejad D, Mazzoli S (2018) The seismogenic fault system of the 2017 mw 7.3 iran-iraq earthquake: Constraints from surface and subsurface data, cross-section balancing, and restoration. Solid Earth 9:821–831

Tavani S, Camanni G, Nappo M, Snidero M, Ascione A, Valente E, Gharabeigli G, Morsalnejad D, Mazzoli S (2020) The mountain front flexure in the lurestan region of the zagros belt: Crustal architecture and role of structural inheritances. Journal of Structural Geology 135(December 2019):104022

Teknik V, Thybo H, Artemieva I (2019) Crustal density structure of nw iranian plateau. Canadian Journal of Earth Sciences

Thatcher W (2007) Microplate model for the present-day deformation of tibet. Journal of Geophysical Research: Solid Earth 112(B1)

Tian Z, Freymueller JT, Yang Z (2020) Spatio-temporal variations of afterslip and viscoelastic relaxation following the mw 7.8 gorkha (nepal) earthquake. Earth and Planetary Science Letters 532:116031

Tian Z, Freymueller JT, Yang Z (2021) Postseismic deformation due to the 2012 m w 7.8 haida gwaii and 2013 m w 7.5 craig earthquakes and its implications for regional rheological structure. Journal of Geophysical Research: Solid Earth 126(2):e2020JB020197

Tong X, Sandwell DT, Smith-Konter B (2013) High-resolution interseismic velocity data along the san andreas fault from gps and insar. Journal of Geophysical Research: Solid Earth 118(1):369–389

Torres R, Snoeij P, Geudtner D, Bibby D, Davidson M, Attema E, Potin P, Rommen B, Floury N, Brown M, et al. (2012) Gmes sentinel-1 mission. Remote Sensing of Environment 120:9–24

Vajedian S, Motagh M, Mousavi Z, Motaghi K, Fielding EJ, Akbari B, Wetzel HU, Darabi A (2018) Coseismic deformation field of the mw 7.3 12 november 2017 sarpol-e zahab (iran) earthquake: A decoupling horizon in the northern zagros mountains inferred from insar observations. Remote Sensing 10(1589)

Vergés J, Saura E, Casciello E, Fernàndez M, Villaseñor A, Jiménez-Munt I, García-Castellanos D (2011) Crustal-scale cross-sections across the nw zagros belt: Implications for the arabian margin reconstruction. Geological Magazine 148(5-6):739–761

Vergnolle M, Calais E, Dong L (2007) Dynamics of continental deformation in asia. Journal of Geophysical Research: Solid Earth 112(B11)

Vernant P, Nilforoushan F, Hatzfeld D, Abbassi MR, Vigny C, Masson F, Nankali H, Martinod J, Ashtiani A, Bayer R, Tavakoli F, Chéry J (2004) Present-day crustal deformation and plate kinematics in the middle east constrained by gps measurements in iran and northern oman. Geophysical Journal International 157:381–398

Walpersdorf A, Hatzfeld D, Nankali H, Tavakoli F, Nilforoushan F, Tatar M, Vernant P, Chéry J, Masson F (2006) Difference in the gps deformation pattern of north and central zagros (iran). Geophysical Journal International 167:1077–1088

Walters R, Holley R, Parsons B, Wright T (2011) Interseismic strain accumulation across the north anatolian fault from envisat insar measurements. Geophysical research letters 38(5)

Wang H, Wright T, Biggs J (2009) Interseismic slip rate of the northwestern xianshuihe fault from insar data. Geophysical Research Letters 36(3)

Wang K, Bürgmann R (2020) Probing fault frictional properties during afterslip updip and downdip of the 2017 mw 7.3 sarpol-e zahab earthquake with space geodesy. Journal of Geophysical Research: Solid Earth 125(e2020JB020319)

Wang K, Fialko Y (2014) Space geodetic observations and models of postseismic deformation due to the 2005 m7.6 kashmir (pakistan) earthquake. Journal of Geophysical Research: Solid Earth 119(9):7306–7318

Wang K, Fialko Y (2015) Slip model of the 2015 mw 7.8 gorkha (nepal) earthquake from inversions of alos-2 and gps data. Geophysical Research Letters 42(18):7452–7458

Wang K, Fialko Y (2018) Observations and modeling of coseismic and postseismic deformation due to the 2015 mw 7.8 gorkha (nepal) earthquake. Journal of Geophysical Research: Solid Earth 123(1):761–779

Wang K, Hu Y, He J (2012) Deformation cycles of subduction earthquakes in a viscoelastic earth. Nature 484(7394):327–332

Wang L (2018) The next m 6 event in parkfield implied by a physical model linking interseismic, coseismic, and postseismic phase. Journal of Geophysical Research: Solid Earth 123(10):8858–8873

Wang R, Lorenzo-Martín F, Roth F (2006) Psgrn/pscmp—a new code for calculating co-and post-seismic deformation, geoid and gravity changes based on the viscoelastic-gravitational dislocation theory. Computers & Geosciences 32(4):527–541

Wang S, Xu C, Li Z, Wen Y, Song C (2020) The 2018 mw 7.5 papua new guinea earthquake: A possible complex multiple faults failure event with deep-seated reverse faulting. Earth and Space Science 7(3):e2019EA000966

Wegnüller U, Werner C, Strozzi T, Wiesmann A, Frey O, Santoro M (2016) Sentinel-1 support in the gamma software. Procedia Computer Science 100:1305–1312

Wright T, Parsons B, Fielding E (2001) Measurement of interseismic strain accumulation across the north anatolian fault by satellite radar interferometry. Geophysical Research Letters 28(10):2117–2120

Wright TJ, Parsons BE, Lu Z (2004) Toward mapping surface deformation in three dimensions using insar. Geophysical Research Letters 31(1)

Wu DL, Ge WP, Liu SZ, Yuan DY, Zhang B, Wei CM (2024) Present-day 3d crustal deformation of the northeastern tibetan plateau from space geodesy. Geophysical Research Letters 51(4):e2023GL106143

Xu G, Xu C, Wen Y, Yin Z (2019) Coseismic and postseismic deformation of the 2016 mw 6.2 lampa earthquake, southern peru, constrained by interferometric synthetic aperture radar. Journal of Geophysical Research: Solid Earth 124(4):4250–4272

Xu W, Liu X, Bürgmann R, Xie L, Feng G, Li Z, Wu L (2022) Space geodetic evidence of basement-involved thick-skinned orogeny and fault frictional heterogeneity of the papuan fold belt, papua new guinea. Journal of Geophysical Research: Solid Earth 127(8):e2022JB024227

Xu X, Sandwell DT, Klein E, Bock Y (2021) Integrated sentinel-1 insar and gnss time-series along the san andreas fault system. Journal of Geophysical Research: Solid Earth 126(11):e2021JB022579

Yang C, Han B, Zhao C, Du J, Zhang D, Zhu S (2019) Co- and post-seismic deformation mechanisms of the mw 7.3 iran earthquake (2017) revealed by sentinel-1 insar observations. Remote Sensing 11(4):1–17

Yang YH, Hu JC, Yassaghi A, Tsai MC, Zare M, Chen Q, Wang ZG, Rajabi AM, Kamranzad F (2018) Midcrustal thrusting and vertical deformation partitioning constraint by 2017 mw 7.3 sarpol zahab earthquake in zagros mountain belt, iran. Seismological Research Letters 89(6):2204–2213

Yassaghi A, Marone C (2019) The relationship between fault zone structure and frictional heterogeneity, insight from faults in the high zagros. Tectonophysics 762:109–120

Yu C, Li Z, Penna NT, Crippa P (2018) Generic atmospheric correction model for interferometric synthetic aperture radar observations. Journal of Geophysical Research: Solid Earth 123(10):9202–9222

Yue LF, Suppe J, Hung JH (2005) Structural geology of a classic thrust belt earthquake: The 1999 chi-chi earthquake taiwan (mw=7.6). Journal of Structural Geology 27(11):2058–2083

Zebker HA, Rosen PA, Hensley S (1997) Atmospheric effects in interferometric synthetic aperture radar surface deformation and topographic maps. Journal of geophysical research: solid earth 102(B4):7547–7563

Zhao B, Bürgmann R, Wang D, Tan K, Du R, Zhang R (2017) Dominant controls of downdip afterslip and viscous relaxation on the postseismic displacements following the mw7.9 gorkha, nepal, earthquake. Journal of Geophysical Research: Solid Earth 122(10):8376–8401

Zhao D, Qu C, Bürgmann R, Gong W, Shan X, Qiao X, Zhao L, Chen H, Liu L (2022) Large-scale crustal deformation, slip-rate variation, and strain distribution along the kunlun fault (tibet) from sentinel-1 insar observations (2015–2020). Journal of Geophysical Research: Solid Earth 127(1):e2021JB022892

Zhou Y, Walker RT, Hollingsworth J, Talebian M, Song X, Parsons B (2016) Coseismic and postseismic displacements from the 1978 mw 7.3 tabas-e-golshan earthquake in eastern iran. Earth and Planetary Science Letters 452:185–196

Eidesstattliche Erklärung

Hiermit versichere ich an Eides statt, dass ich

1. die Regeln der geltenden Promotionsordnung kenne und eingehalten habe und mit einer Prüfung nach den Bestimmungen der Promotionsordnung einverstanden bin;
2. die Dissertation selbst verfasst habe (Selbstständigkeitserklärung), keine Textabschnitte von Dritten oder eigener Prüfungsarbeit ohne Kennzeichnung übernommen habe und alle von mir benutzten Hilfsmittel und Quellen in meiner Arbeit angegeben habe;
3. Dritten weder unmittelbar noch mittelbar geldwerte Leistungen für Vermittlungstätigkeiten oder für die inhaltliche Ausarbeitung der Dissertation erbracht habe (d.h. die wissenschaftliche Arbeit wurde weder in Teilen noch in Gänze von Dritten gegen Entgelt oder sonstige Gegenleistung erworben oder vermittelt);
4. die Dissertation noch nicht als Prüfungsarbeit für eine staatliche oder andere wissenschaftliche Prüfung eingereicht habe;
5. die gleiche oder in wesentlichen Teilen ähnliche Arbeit nicht bei einer anderen Hochschule als Dissertation eingereicht habe; desgleichen habe ich keine andere Abhandlung als Dissertation eingereicht;
6. damit einverstanden bin, dass die Dissertation auch zum Zwecke der Überprüfung der Einhaltung allgemein geltender wissenschaftlicher Standards genutzt wird, insbesondere auch unter Verwendung elektronischer Datenverarbeitungsprogramme.

Hannover, 2025

Zelong Guo

Basic Information

Date of Birth: 28.09.1993

Place of Birth: Jinan City, Shandong Province, China

Education

Wuhan University

Master in Geophysics — *Wuhan, CN*, *Sep. 2017 – Jul.2020*

- **Institute:** School of Geodesy and Geomatics
- **Advisor:** Prof. Yangmao Wen

Shandong University of Science and Technology — *Qingdao, CN*, *Sep. 2012 – Jul.2016*

Bachelor in Geodesy

- **Institute:** School of Geomatics

Publications

- ***Guo, Z.***, M. Base, and M. Motagh (2024). Ramp-Flat and Splay Faulting Illuminated by Frictional Afterslip Following the 2017 Mw 7.3 Sarpol-e Zahab Earthquake, *Seismological Research Letter*, 1-14, doi:10.1785/0220230425

- ***Guo, Z.***, Motagh, M., Hu, J.-C., Xu, G., Haghighi, M. H., Bahroudi, A., et al. (2022). Depth-varying Fric- tion on a Ramp-flat Fault Illuminated by ~3-year InSAR Observations Following the 2017 Mw 7.3 Sarpol-e Zahab earthquake. *Journal of Geophysical Research: Solid Earth,* 127, doi: 10.1029/2022JB025148

- ***Guo, Z.,*** Wen, Y., Xu, G., Wang, S., Wang, X., Liu, Y., and Xu, C. (2019). Fault Slip Model of the 2018 Mw 6.6 Hokkaido Eastern Iburi, Japan, Earthquake Estimated from Satellite Radar and GPS Measurements. *Remote Sensing*, 11(14), doi:10.3390/rs11141667

- Wen, Y., ***Guo, Z.***, Xu, C., Xu, G., and Song, C. (2019). Coseismic and Postseismic Deformation Associated with the 2018 Mw 7.9 Kodiak, Alaska, Earthquake from Low-Rate and High-Rate GPS Observations. *Bulletin of the Seismological Society of America*, 109(3), 908–918, doi:10.1785/0120180246

- Peng, M., Motagh, M., Lu, Z., Xia, Z., ***Guo, Z.***, Zhao, C. and Liu, Q. (2023). Characterization and pre- diction of InSAR-derived ground motion with ICA-assisted LSTM model. *Remote Sensing of Environment*, 301,113923, doi:10.1016/j.rse.2023.113923

- Xu, G., Wen, Y., Yi, Y., ***Guo, Z.***, Wang. L., and Xu, C. (2023). Geodetic constraints of the 2015 Mw 6.5 Alor, East Indonesia earthquake: a strike-slip faulting in the convergent boundary. *Geophysical Journal International*, 235(1), doi:10.1093/gji/ggad211

- Zhang, Y., Xu, C., Fang, J. and Guo, Z. (2021). Focal mechanism inversion of the 2018 Mw 7.1 An- chorage earthquake based on high-rate GPS observation. Geodesy and Geodynamics, 12(6), 381-391, doi:10.1016/j.geog.2021.09.004

Wissenschaftliche Arbeiten der Fachrichtung Geodäsie und Geoinformatik der Leibniz Universität Hannover

(Eine vollständige Liste der Wiss. Arb. ist beim Geodätischen Institut, Nienburger Str. 1, 30167 Hannover erhältlich.)

Nr. 381	WASSINK, Martin:	Kommunal- und Regionalentwicklung durch Kooperation und Teilung von Verantwortung in ländlichen Räumen - eine multiperspektivische Untersuchung an Beispielen aus dem Raum Steinwald/Fichtelgebirge (Diss. 2022)
Nr. 382	GOLDSCHMIDT, Jürgen:	Die Berücksichtigung künftiger Entwicklungen bei der Verkehrswertermittlung (Diss 2022)
Nr. 383	KRUSE, Christian:	Impact maps from bomb craters detected in aerial wartime images using marked point processes (Diss. 2023)
Nr. 384	ZOURLIDOU, Stefania:	Traffic Regulation Recognition from GPS Data (Diss. 2023)
Nr. 385	SLEDZ, Artuom:	Thermal anomaly detection based on information fusion from optical and infrared images (Diss. 2023)
Nr. 386	WITTICH, Dennis:	Deep Domain Adaptation for the Pixel-wise Classification of Aerial and Satellite Images (Diss. 2023)
Nr. 387	SINGH, Vishwa Vijay:	Lunar Laser Ranging - Improved Modelling and Parameter Estimation (Diss. 2023)
Nr. 388	HARTMANN, Jens:	Hochgenaue 3D-Erfassung von Großstrukturen durch kinematisches terrestrisches Laserscanning (Diss. 2023)
Nr. 389	ZHUGE, Xia:	Characterizing slope instability kinematics by integrating multi-sensor satellite remote sensing observations (Diss. 2023)
Nr. 390	DOROZYNSKI, Mareike Marianne:	Image Classification and Retrieval in the Context of Silk Heritage using Deep Learning (Diss. 2023)
Nr. 391	KNABE, Annike:	New Concepts for Gravity Field Recovery using Satellites (Diss. 2023)
Nr. 392	KALIA, Andre:	Landslide activity detection based on nationwide Sentinel-1 PSI datasets (Diss. 2023)
Nr. 393	BROCKMEYER, Marco:	Modellierung von Bodenbewegungen anhand heterogener Messverfahren am Beispiel der niedersächsischen Landesfläche (Diss. 2023)
Nr. 394	ZHANG, Mingyue:	Characteristics and Benefits of Differential Lunar Laser Ranging (Diss. 2023)
Nr. 395	DENNIG, Dirk:	Entwicklung eines kinematischen Profilvermessungssystems am Beispiel Kranbahnvermessung (Diss. 2024)
Nr. 396	FUEST, Stefan:	Nudging travelers to societally favorable routes by means of cartographic symbolization (Diss. 2024)
Nr. 397	MOFTIZADEH, Rozhin:	Advanced Particle Filtering for Vehicle Navigation based on Collaborative Information (Diss. 2024)
Nr. 398	VASSILEVA, Magdalena Stefanova:	Satellite Radar Interferometry for Geohazards: from ground deformation to processes understanding (Diss. 2024)
Nr. 399	MALINOVSKAYA, Anna:	Statistical Process Monitoring of Networks (Diss. 2024)
Nr. 400	BANNERT, Jörn:	Der Einfluss von Straßenverkehrslärm und Umgehungsstraßen auf Grundstückswerte in Ortslagen - Bestimmung mittels Expertenbefragung nach der Delphi-Methode (Diss. 2024)
Nr. 401	AXMANN: Jeldrik:	Maximum consensus localization using LiDAR (Diss. 2024)
Nr. 402	TENNSTEDT, Benjamin:	Concept and Evaluation of a Hybridization Scheme for Atom Interferometers and Inertial Measurement Units (Diss. 2024)
Nr. 403	HAKE, Frederic:	Schadenserkennung an Bauwerken mittels maschinellem Lernens (Diss. 2025)
Nr. 404	KARIMIDOONA, Ali:	On Integrity Prediction for Network-RTK Positioning in Urban Environments (Diss. 2025)
Nr. 405	ORTEGA, Mabel:	Domain Adaptation for Deforestation Detection in Remote Sensing: Addressing Class Imbalance and Performance Estimation (Diss. 2025)
Nr. 406	KUPRIYANOV, Alexey:	Investigation of Optical Accelerometry and Novel Satellite Formations for Future Gravimetry Missions (Diss. 2025)
Nr. 407	BREVA, Yannick:	On the Observation Quality of Robot-based GNSS Antenna Calibration for Determining Codephase Corrections (Diss. 2025)
Nr. 408	GUO, Zelong:	Co- and Post-seismic Slip Models Inferred from InSAR Geodesy (Diss. 2025)